DETERMINATION OF THE NON-RECRYSTALLIZATION TEMPERATURE (T_{NR}) IN MULTIPLE MICROALLOYED STEELS

by
Caryn Nicole Homsher

A thesis submitted to the Faculty and the Board of Trustees of the Colorado School of Mines in partial fulfillment of the requirements for the degree of Master of Science (Metallurgical and Materials Engineering).

Golden, Colorado

Date _____

Signed: _____

Caryn Nicole Homsher

Signed: _____

Dr. Chester J. Van Tyne
Thesis Advisor

Golden, Colorado

Date _____

Signed: _____

Dr. Michael J. Kaufman
Professor and Head
Department of Metallurgical and
Materials Engineering

ABSTRACT

Rolling mill metallurgists must be able to easily and accurately determine critical temperatures such as the non-recrystallization temperature (T_{NR}) to properly plan rolling schedules for desired properties. Microalloyed steels have small additions of alloying elements such as V, Ti, and Nb, to improve mechanical properties through grain size control and precipitation strengthening. The value of T_{NR} is based on both alloying elements and deformation parameters. To easily predict T_{NR}, equations have been developed and utilized in the literature and industry. However, each equation has certain limitations which constrain its applicability. This study was completed using ten laboratory grade low-carbon microalloyed steels designed to meet the API X-70 specification with varying amounts of V, Nb, and Ti. Double-hit deformation tests were conducted on a Gleeble® 3500 system in the standard pocket-jaw configuration at the Colorado School of Mines to determine experimental values of T_{NR}. Double-hit deformation tests involve cylindrical specimens in an axisymmetric compression test. The test method requires six steps: 1) reheat to ensure most precipitates dissolve back into solution, 2) cool to deformation temperature, 3) compress with given strain and strain rate, 4) hold for interpass time, 5) deform specimen again holding everything else constant, and 6) measure the percent recrystallized or percent fractional softening. The T_{NR} is the temperature where fractional softening is equal to 20 %. Niobium plays the largest role in influencing T_{NR}. Complex niobium-vanadium-carbonitride precipitates are believed to play a significant role increasing T_{NR} in the Hi-V alloy The experimental values of T_{NR} were compared with predicted values of T_{NR} from four equations in the literature. The Bai 2011 equation was the most reliable of the existing empirical formulas considered, while the commonly used Boratto equation was not accurate in predicting the T_{NR} for the alloys in this study. The Bai 2011 equation is a reasonable estimator for T_{NR} for the steels in this study. The Boratto equation ignores the effects of N and has consistently high predictions of T_{NR} for the steels investigated.

TABLE OF CONTENTS

LIST OF FIGURES

LIST OF TABLES

ACKNOWLEDGEMENTS

I would like to first thank my family, specifically my parents Carl and Laurene Homsher for the support and encouragement they have given me throughout the years. I would not be the woman I am today without your love and guidance. To my sister, Andrea Lyn, I owe a debt of gratitude. You were always my biggest cheerleader! To my fiancé, Marcus Ritosa, for supporting me on whatever crazy far off adventure I choose to face. And to my grandparents Ken and Rowena Lautzenheiser for always believing in me from a young age and giving me the vision and drive to explore the world both near and far away.

I would like to also thank the Advanced Steel Processing and Products Research Center at the Colorado School of Mines for taking a chance on a mechanical engineer. I sincerely thank my advisor, Prof. Chester Van Tyne for all of his insights, both academic and life related. You have helped me see this is where I want to be. Thank you to my committee members Dr. John Speer and Dr. Emmanuel De Moor for their suggestions, inputs and guidance along my way. I am sincerely grateful to my industrial mentors Dr. Dengqi Bai from SSAB Americas, Dr. Matt Green from Tata Steel Europe, and Dr. Matt Merwin from US Steel. You have challenged me and helped me when I needed it most.

I thank my colleagues, especially Paul Gibbs, Stephanie Miller, Julian Stock, Timothy Barlow, Tyson Brown, and Lee Rothleutner for extensive conversations, assistance, and support. Thank you to the undergraduate research assistance Ana Luiza and Matt Glaizer for their continued support and never failing lack of enthusiasm!

I finally would like to thank the Golden First United Methodist Church for welcoming me over two years ago, specifically to my surrogate families Lea Conklin, Lynda Smith and Laura Wolfe. I always appreciate being part of a family when my own is not around.

CHAPTER 1 : INTRODUCTION

Microalloying with multiple alloy elements is widely used in low-carbon high strength low alloy (HSLA) steels. Typical applications of HSLA microalloyed plate steels include marine applications, pipeline steels, construction steels, and machinery steels [1], [2].

Microalloyed steels have small additions of alloying elements such as V, Ti, and Nb, to improve mechanical properties through grain size control and precipitation strengthening [1]. For example, microalloying is used in API X-70 and X-80 line pipe steels to modify ferrite-perlite or bainite steel to improve strength and toughness [3].

The present study focuses on the influence of V and Ti on the T_{NR} of Nb-bearing microalloyed steels. If processed correctly, the steels should meet the requirements of API X-70 grade [4]. The primary purpose of this study is to characterize and understand high temperature properties during rolling. The focus is not mechanical properties at room temperature, but rather mechanical behavior and properties during hot rolling.

For a rolling mill metallurgist, it is important to know how to determine or estimate the non-recrystallization temperature (T_{NR}) as a function of the microalloying elements in the steel in order to determine rolling schedules to produce desired properties and microstructures. The present investigation was designed to provide insight into the synergistic effects of titanium (Ti) and vanadium (V) on the T_{NR} in niobium (Nb)-microalloyed plate steels.

This study was completed using double-hit deformation testing on a Gleeble® 3500 system in the standard pocket-jaw to determine experimental values of T_{NR}. Double-hit deformation tests typically use cylindrical specimens in an axisymmetric compression test. The test involves reheating to ensure most precipitates dissolve back into solution, cooling to deformation temperature, compressing with given strain and strain rate, holding for interpass time, deforming specimen again holding everything else constant, and measuring the percent recrystallized or percent fractional softening.

CHAPTER 2 : BACKGROUND

Microalloyed (MA) high strength low alloy (HSLA) steels have become increasingly popular, particularly in plate and pipeline steel applications where larger diameter pipes are being developed with the need for increased strength, formability, and joinablilty [5]. In combination with processing parameters, small additions of V, Nb, and Ti to HSLA steels are designed to achieve higher strength while minimizing required plate thicknesses for the desired application. Microalloying additions are generally used for grain refinement, to influence recrystallization behavior, and for precipitation strengthening through the formation of carbides or nitrides [5]. Each element contributes to the various strengthening mechanisms differently and will be discussed further in this chapter.

This chapter also provides background regarding concepts and current research into the non-recrystallization temperature (T_{NR}) of multiple microalloyed plate steels that are relevant to the research of this thesis. Specifically, hot rolling, recrystallization, and the behavior of V, Nb, and Ti in microalloyed plate steels are discussed.

2.1 Hot Rolling

Rolling is a process of plastically deforming a material passed through two or more rotating rolls. Hot rolling, as with all hot-working processes, requires elevated temperature control, generally in the range 850 °C-1320 °C (1562 °F-2408 °F) for steel [5]. The lower flow stress of the material at high temperature requires lower tool forces and power to deform the plate [6]. The workpiece is heated to a uniform elevated temperature in the austenite region, typically above the T_{NR}. The T_{NR} for the steel is alloy dependent [5], [7], [8] and also dependent on the deformation parameters [5], [9–12] . For MA steels, the reaustenitizing temperature, or soak temperature, is often between 1200 °C and 1320 °C (2192 °F and 2408 °F) [5]. The steel is then cooled and rolled at a given deformation temperature.

Hot rolling of steel previously began with a primary roughing mill (also called blooming, slabbing, or cogging mill) [13]. A roughing mill is usually a two-high reversing mill with 0.610-1.37 m (24-54 in) diameter rolls. An ingot is broken down into blooms or slabs for further processing of plates, bars, or sheets. The initial breakdown passes usually only involve small reductions. Significant spreading of the ingot width occurs during hot rolling [14]. Ingots are rotated 90° during intermediate passes and often pass through edging rolls or grooves to maintain desired dimensions. An ingot may go through one reversing mill 10-20 times before moving to subsequent processes [14]. With industrial improvements, continuous casting of slabs is now used in high-production plants, where slabs are produced directly from the molten metal. Plates are produced from reheated slabs or ingots. Figure 2.1 shows the flow of rolled material in various rolling mills.

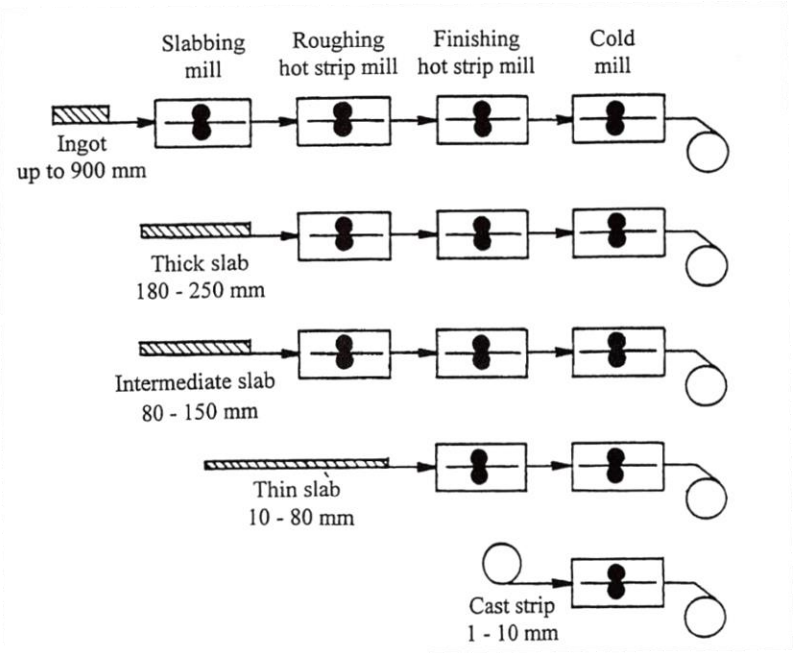

Figure 2.1 Flow of rolled material through various rolling mills [15].

Utilizing slabs to roll plate steel, instead of ingots, allows achievement of better surface quality, and yield improved mechanical properties, improved temperature control, and greater output due to fewer passes. Dedicated plate mills are capable of rolling product 2.54 -5.08 m (100-200 in) wide. In the late 1960's, high pressure water sprays started being used to remove primary and secondary scale from the workpiece, replacing the previously used scale-breaking stands [16].

A slab is sent to a reheat furnace to be heated to a desired temperature. The slab then goes through the roughing mill, which consists of a series of vertical and horizontal mill stands. A shear is used, typically to remove the head and tail before entering the finishing mill. The finishing mill utilizes one or a series of horizontal mill stands and loopers to maintain desired strip tension by pushing a free rotating roller against the strip [15]. On the runout table, a series of water cooling headers reduce the plate temperature. In some cases, the plate is coiled, but coiling is usually reserved for strip steel. The plate undergoes a descaling operation to remove any scale from the surface using a high-pressure water system. Further cooling may take place before the plate is ready for further processing.

Depending on desired properties, hot rolling can be terminated approximately 50 °C to 100 °C (90 °F to 180 °F) above the T_{NR} to ensure uniform fine grains and prevent the possibility of strain-hardening [14]. Deformation below T_{NR} leads to work hardening, and therefore the formation of "pancaked" grains and deformation bands[7], [10], [12], [17–19]. The increased grain boundary area increases the number of

nucleation sites for the austenite-to-ferrite transition and may promote a fine grained microstructure producing a plate with a good balance of strength and toughness properties.

2.2 Recrystallization

Recrystallization is the formation of new strain-free, equiaxed grains. Recrystallization occurs when a material has undergone a certain amount of deformation and is heated to a point where sufficient energy is available to drive recrystallization. For plate steels the deformation is typically imparted by rolling. The deformed grains that have been "pancaked," i.e. elongated in one direction, have a high dislocation density, which creates nucleation sites for new grains [20]. The new grains have the same composition and phase as the parent grains with lower stored energy. The lower-energy material is accompanied by a decrease in strength and a simultaneous increase in ductility from the parent structure. These changes in material properties may be undesired if high strength is required or desirable if the need is to regain ductility after cold working [20]. For ferrite-pearlite steels, an increase in crystalline defect content in the austenite will provide nucleation sites for ferrite [21]. As industry places greater requirements on the mechanical and physical requirements of metals, even greater interest in understanding, predicting, and utilizing recrystallization is necessary.

Figure 2.2 schematically presents the normal sequence and mechanisms for the recrystallization process in a simplified fashion. Figure 2.2a shows a deformed structure. Figure 2.2b shows the effects of recovery where subgrains have formed in the deformed regions. Figure 2.2c shows nucleation of strain-free grains to form a partially recrystallized structure. Figure 2.2d shows a fully recrystallized structure with fine equiaxed grains. It should be noted that these mechanisms can occur simultaneously. The recrystallization process can occur statically, dynamically or meta-dynamically. Time and temperature also play a significant role in these individual steps and hence in the overall recrystallization process.

During hot rolling, hot steel with large grains enters the roll bite where the material is deformed, "pancaking" the grains. After leaving the rolls, the grains recrystallize in a process known as static recrystallization [5], [22], [23] and begin to grow. This step is typically followed by further deformation and the process repeats until the temperature of the material cools to a point about where recrystallization is not completed, often 50-100 °C (122-212 °F) above the normally defined recrystallization temperature (T_r) [14]. Figure 2.3 shows a schematic of the hot rolling process and static recrystallization with large austenite grains before the plate enters the roll bite, deformed grains in the roll bite and recrystallized grains after the material has left the roll bite. Recrystallization during deformation (while the material is in the roll bite) can occur if enough strain has accumulated prior to deformation, and is called dynamic recrystallization [5], [22].

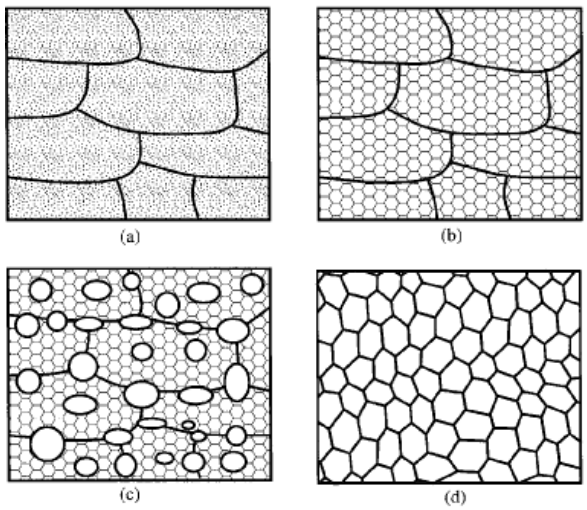

Figure 2.2 Schematic diagram of recrystallization sequence (a) deformed grains, (b) recovered grains, (c) partially recrystallized, (d) fully recrystallized [23].

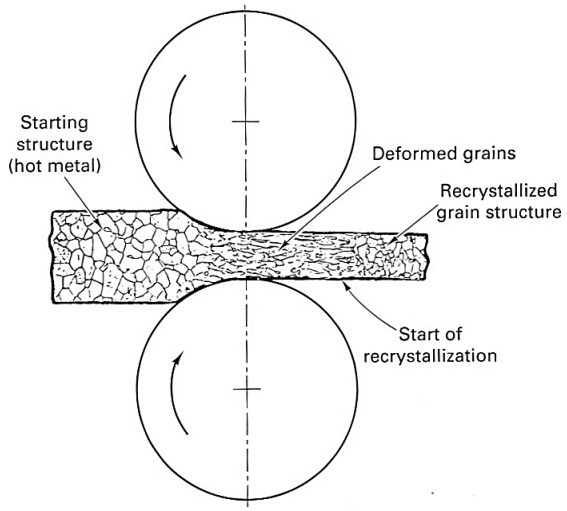

Figure 2.3 Schematic representation of the hot-rolling process, showing deformation and recrystallization of the rolled metal [14].

2.2.1 Recrystallization Kinetics

The rate of recrystallization depends on time, temperature, and the amount of strain (deformation) within the material. Recrystallization normally has an Avrami or sigmoidal behavior with time, starting slow, accelerating and plateauing near the end [10], [24–26]. Figure 2.4 shows recrystallization kinetics for pure copper with percent recrystallized as a function of time for various temperatures. The same model holds true for steel. Each curve is an isothermal line. At higher temperatures recrystallization occurs faster

than at cooler temperatures. In Figure 2.4 the higher temperatures are on the left side of the graph, signifying a shorter time for complete recrystallization.

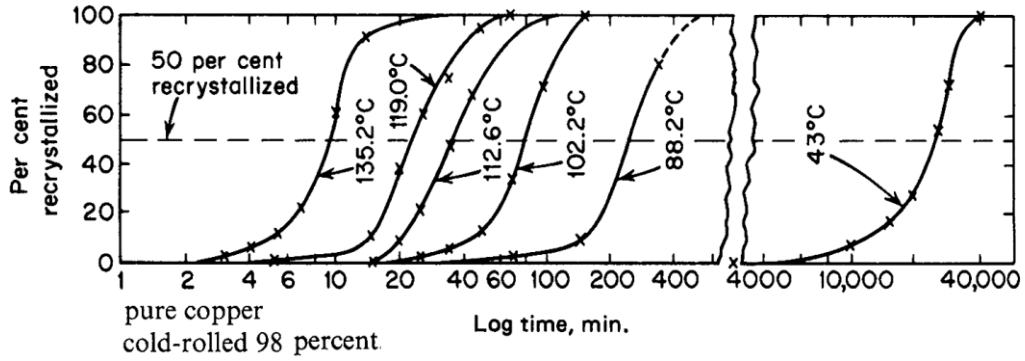

Figure 2.4 Isothermal transformation (recrystallization) kinetics for pure copper [25].

Another major factor in recrystallization kinetics is the original grain size. Generally, fine-grained materials recrystallize faster than coarse-grained materials. This shorter recrystallization time in fine-grained materials is mainly due to increased grain boundary area providing more "nucleation" sites for the recrystallized grains [23]. The effects of grain size on recrystallization kinetics can be summarized as:

- Smaller grain size leads to an increase in stored energy of a metal deformed to low strains.
- Deformation and shear bands form more readily in coarse grains, which increase the number of sites for nucleation.
- Finer grains have a larger grain boundary area than coarse grains, which are the preferred nucleation sites.

Two main methods have been used to quantify recrystallization kinetics[20], [21], [23], [27]. The simple Johnson-Mehl-Avrami-Kolmogorov (JMAK) model based on fraction of recrystallized material, and a more complex model, microstructure path methodology (MPM), which uses additional microstructural parameters. Both models have limitations in handling the recrystallization kinetics for inhomogeneous recrystallization and for recrystallization concurrent with recovery [23], [27].

2.2.2 Definition of the Non-Recrystallization Temperature (T_{NR})

Multiple critical temperatures exist during hot rolling. During cooling, the first is known as the non-recrystallization temperature (T_{NR}) where complete static recrystallization no longer occurs for a given hold time. The second critical temperature is known as the recrystallization temperature or recrystallization stop temperature (T_r) where no recrystallization occurs for a given hold time. As a rule of thumb, T_r is roughly 75 °C below T_{NR} [2], [28]. A third critical temperature is the Ar_3 where the austenite starts to transform to ferrite.

Deformation above the T_{NR} results in equiaxed recrystallized grains. Without further recrystallization, the grains could become large through grain coarsening. Deformation below T_r results in elongated grains and the formation of deformation bands, which act as nucleation sites for ferrite transformation. If the starting grains were the same size, rolling below the T_{NR} would result in finer ferrite grains than rolling above the T_{NR} because the ratio of grain boundary surface area to grain volume is increased. The higher nucleation density leads to significantly smaller ferrite grains [2]. Deformation between T_{NR} and T_r results in a mixture including some recrystallized grains and some deformed grains. Since some deformation is accumulated, complete recrystallization is not possible. Figure 2.5 shows an illustration of recrystallization rolling above T_{NR}, rolling between T_{NR} and T_r, and rolling below T_r. between two passes.

2.3 Microalloyed Plate Steels

Microalloyed (MA) steels use small additions, often on the order of 0.1 wt pct or less, of alloying elements such as V, Nb, and Ti to improve mechanical properties through precipitation strengthening and grain size control. Grain refinement is typically achieved through MA carbide or nitride precipitation at high temperature to control austenite grain size and morphology during processing [5], [21].

2.3.1 Product Applications

High strength low alloyed steels have many applications, most notable in creating large diameter pipe for the oil and gas industry. Other applications include construction materials for high-rise buildings, bridges, offshore structures, farm machinery, automotive applications, and transmission towers. Niobium and other MA elements continue to provide strength with lower carbon levels to help with weldability in pipeline steels and increase strength and toughness, allowing ships and buildings to use less steel for the same strength, and better corrosion resistance [29].

2.3.2 Solubility of Microalloying Elements

Understanding how microalloying elements influence the microstructure and properties of a particular steel is important. The MA elements are well known for affecting properties of steel through solution strengthening and precipitation as carbides or nitrides. The form the compound takes can be predicted with equilibrium constants for the compound being investigated. For metallurgists, the inverse of the equilibrium constant is often referred to as the solubility product, K_s, and is commonly expressed as a function of temperature given by,

$$\log_{10} K_s = \log_{10}[M][X] = A - \frac{B}{T} \tag{2.1}$$

where K_s is a product of the metallic microalloying elements, *M*, and the interstitial, *X*, in wt pct, *A* and *B* are constants and *T* is absolute temperature [5], [30]. Table 2.1 shows the equations for K_γ, where γ indicates austenite solubilities for the precipitates of interest in this study [5], [30]. Since the coefficients *A* and *B* were found experimentally, there are some discrepancies among the values in the literature [21], [30–32], but the work by Turkdogan [30] has been used in many reports from the literature [5], [33], [34] and will be used in the present investigation. Discrepancies may exist due to the method used to obtain the solubility product such as thermodynamic calculations, chemical separation and isolation of precipitates, hardness measurements, and statistical treatment of previous solubility products [32], [35] resulting in differences of the activities. The NbC and VC compounds have exponents on the C-term of 0.87 and 0.75, respectively. This indicates the compounds are not 1:1 ratios. Instead, the commonly occurring precipitates in HSLA steels are actually Nb_8C_7 and V_4C_3. For simplicity, the precipitates will be referred to at NbC and VC in this study.

Precipitates play a significant role in austenite recrystallization through grain boundary pinning. Grain boundary pinning is a function of the precipitate's solubility, alloy composition, and particle coarsening rate [1], [5]. Fine particles retard austenite grain growth better than coarse precipitates. Solubility in austenite is important, because as the temperature decreases, the solubility product also decreases, until eventually the austenite is supersaturated with the alloying elements, and thus precipitation will occur.

In regards to thermomechanical processing of austenite, whether for research or in a rolling mill, the lowest temperature that dissolves the microalloying elements should be used. This temperature is generally determined by the amount of Nb and C in the steel. Titanium forms a very stable nitirde, which usually remains undissolved [5], [12], [21]. The TiN compound does limit austenite grain growth at high soaking temperatures and may use most of the free N, thereby limiting the formation of other nitrides, most notable NbN.

Figure 2.6 shows the generic influence of V, Al, Nb, and Ti additions on the grain coarsening characteristics of austenite on heating. The line labeled *C-Mn* indicates a plain carbon steel where the austenite grain growth is not inhibited by second-phase particles. The plain carbon steel exhibits larger grain sizes with increasing temperature. Additions of V, Al, and Nb show a temperature range with abnormal grain growth. Abnormal grain growth is a commonly described phenomenon in MA steels [1], [12], [20], [36], [37], where only a few grains grow in a relatively stable matrix of fine grains. The hatched regions show the temperature range where precipitates dissolve, and grain growth is no longer inhibited. Ti forms a very stable nitride that can inhibit grain growth to very high temperatures.

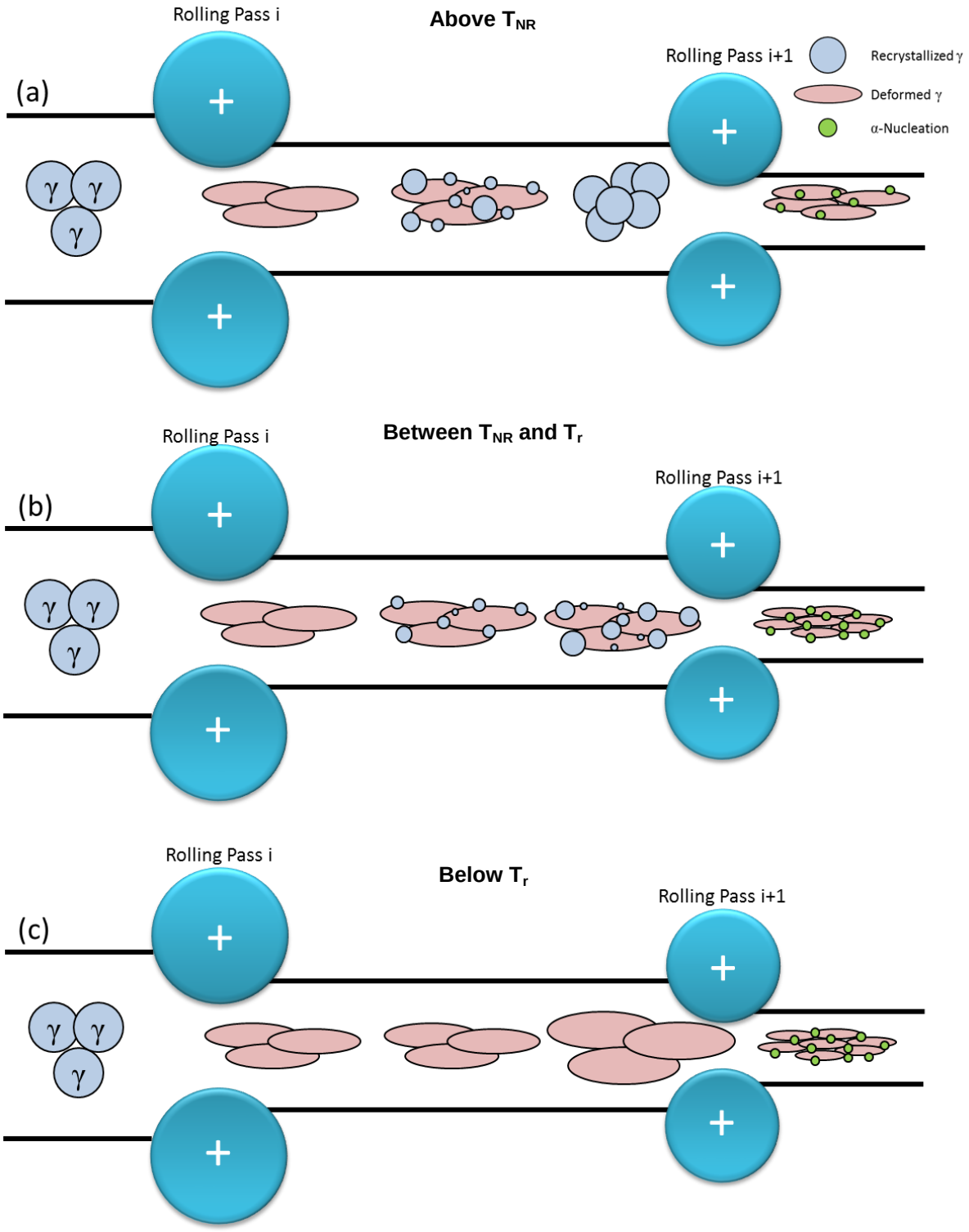

Figure 2.5 Schematic representation of deformation (a) above T_{NR} where complete static recrystallization takes place between rolling passes i and i+1, (b) between T_{NR} and T_r where partial static recrystallization takes place between rolling passes i and i+1, and (c) below T_r where no static recrystallization can occur between rolling passes i and i+1. Ferrite nucleation is depicted after rolling pass i+1 for each representation. Adapted from [12], [18].

Table 2.1 – Solubility Equations [30]

Solubility Product	$\text{Log}_{10}\ K\gamma$
[Ti][N]	$5.40 - \frac{15790}{T}$
[Nb][N]	$3.79 - \frac{10150}{T}$
[V][N]	$2.86 - \frac{7700}{T}$
[Al][N]	$1.30 - \frac{6770}{T}$
[Ti][C]	$2.75 - \frac{7000}{T}$
$[Nb][C]^{0.87}$	$2.81 - \frac{7020}{T}$
$[V][C]^{0.75}$	$4.45 - \frac{6560}{T}$

Figure 2.7 shows the relative solubility products for the precipitating compounds of interest in this study as a function of temperature [30]. It is clearly seen that the solubility product of $VC_{0.75}$ is many orders of magnitude higher than the solubility product of the stable TiN. It is therefore expected that most of vanadium will be in solution, even at low finishing temperatures. Titanium nitrides can form at high temperatures, even in the liquid. Niobium is expected to be in solution during typical reaheating operations, but will precipitate upon cooling during rolling. Precipitation can occur in two ways: First forming purely on cooling, and second forming during or after rolling. This second mode of precipitation is known as strain-induced precipitation or dynamic precipitation [21], [38–41]. The first precipitation mode is not believed to be very significant in commercial rolling as precipitation in recrystallized austenite is typically sluggish [21].

2.3.3 Effect of Alloying Elements on T_{NR}

Microalloying elements are known for their characteristic effects in steel. Some effects are common for all MA elements, while other effects are more unique for a particular element. This subsection will describe some of the characteristics of the MA elements of interest in this study. The present study focuses on the synergistic effects of V, Nb, and Ti on the T_{NR}. Each of the MA elements are transition metals and form solid solutions with iron [21]. Vanadium, Nb, and Ti are all known for grain refinement

strengthening through grain boundary pinning and precipitation strengthening through the formation of carbides, nitrides, or a combination called carbo-nitrides (C,N).

Austenite grain growth is also inhibited through solute drag effects if the alloying elements segregate to the austenite grain boundaries [12], [42], [43]. The alloying elements at the grain boundaries reduce the grain boundary interfacial energy and mobility. The solute atoms force a non-linear boundary velocity, shown by a resistance to grain boundary motion. Thus, the recrystallization rate decreases for a given temperature. The greater the difference in atomic radius of the solute atom versus the iron atom, the greater the effects of solute drag on grain boundary and dislocation motion [12], [43]. The solute drag effect is limited by the solubility limit of the specific element. Above the solubility limit, precipitation can occur and these precipitates may dominate grain boundary mobility. Table 2.2 shows the atomic radii in Å for Fe, V, Nb, Ti, C, and N.

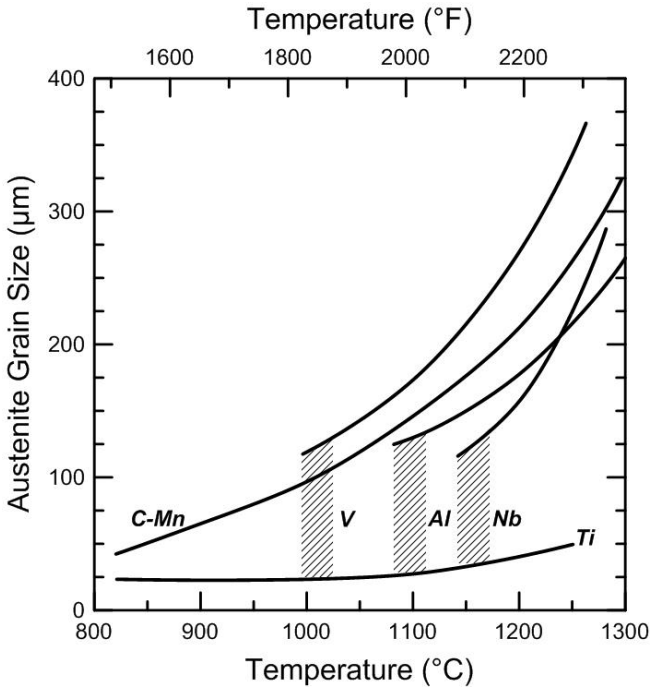

Figure 2.6 Schematic of relative grain-coarsening characteristics of various microalloyed steels adapted from [1].

Figure 2.8 shows the effect of the common MA elements on T_{NR} as a function of initial solute content in a steel with 0.07 C, 1.4 Mn, and 0.25 Si in wt pct [45]. Niobium shows a much greater effect in increasing the T_{NR} than Ti, Al, and V. From the graph, it takes approximately 0.25 atomic pct of V to increase the T_{NR} to roughly 875 °C, where it only requires approximately 0.05 atomic pct Ti for the same increase in temperature. This same increase in T_{NR} can be achieved with only 0.005 atomic pct Nb, an order

of magnitude less than Ti. The atomic radius of Fe is very close to the atomic radius of V, which may explain part of the reason V is not as effective at increasing T_{NR} as Nb and Ti.

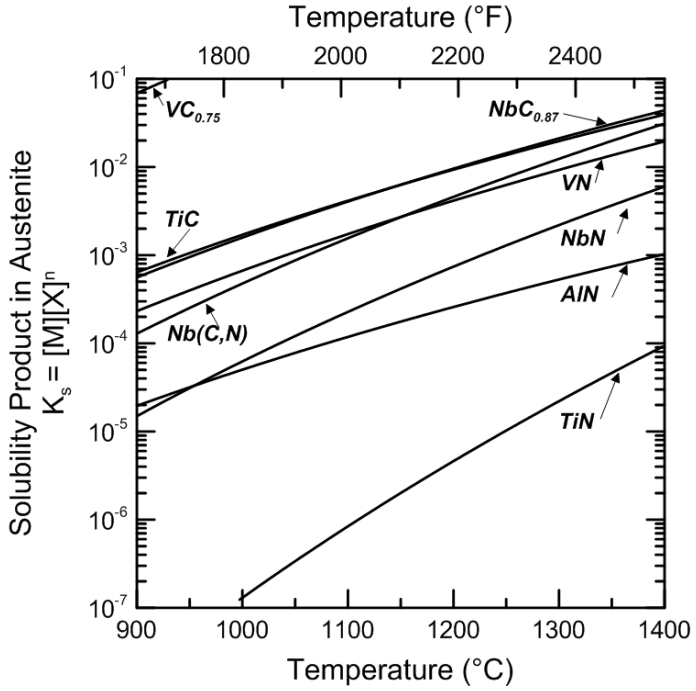

Figure 2.7 Equilibrium solubility products of carbides and nitrides in austenite, adapted from [30].

Table 2.2 – Atomic Radii of Elements of Interest in this Study: Fe, V, Nb, Ti, C, and N [44]

Element	Atomic Radii (Å)
Fe	1.34
V	1.33
Nb	1.48
Ti	1.47
C	0.70
N	0.68

(a) *Vanadium*

Vanadium has a very high solubility in austenite. Even VN, whose solubility is comparable to that of Nb(C,N) is over three orders of magnitude higher than the stable TiN [30]. Vanadium is expected to be in solution until rolling temperatures below 1000 °C for typical plate steel compositions. While solute V is not a strong grain boundary inhibitor through solute drag effects, the lower dissolution temperatures can still play a significant role in austenite conditioning through strain-induced precipitation [46]. The lower

precipitation temperatures ensure the particles are finely dispersed throughout the austenite matrix and thereby are effective in pinning grain boundaries. The likelihood of forming VN is limited to the amount of free-nitrogen remaining in the austenite after TiN and NbN formation, making N a key element in V-MA steels [46]. Aluminum content can also effect free N available to form VN since Al has a greater affinity for N than V. Aluminum can also effect the amount of NbN. Since TiN precipitates are so stable, VN precipitation is only possible through controlling both N and Ti levels where Ti is low and N is high. The VC compound is also not as stable as the VN. While solute V may not play a significant role in retarding recrystallization [45–47], the austenite is able to recrystallize between each pass, thereby refining the austenite grains before transforming to ferrite. The grain refinement can continue to much lower temperatures than is able in a Nb-bearing steel. A study by DeArdo *et al.* [32], shows that extended austenite recrystallization can produce ferrite grains roughly the size of the grains produced through Nb(C,N) pinning grain boundaries providing more nucleation site for fine ferrite to form, as small as 4 μm. In contrast, Nb(C,N) precipitates are effective in retarding austenite recrystallization, thereby forming long, flat grains with increased nucleation sites for ferrite formation [46].

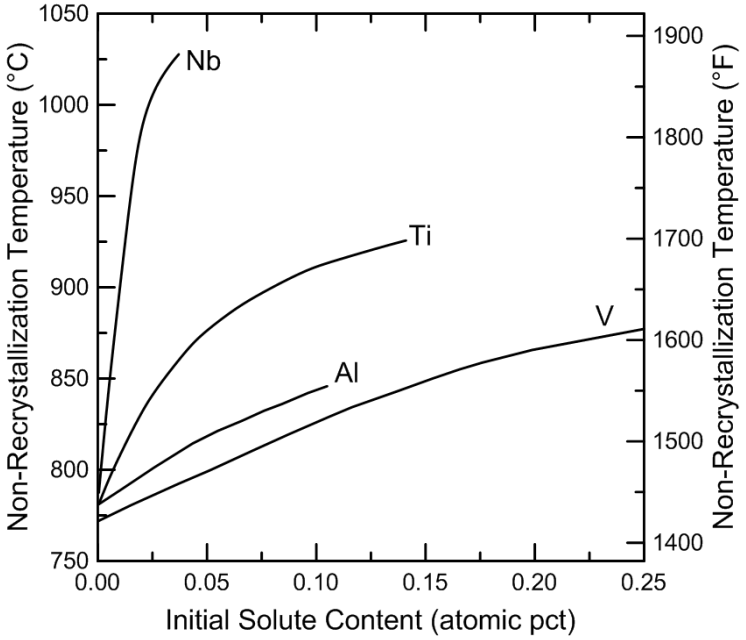

Figure 2.8 The effects of microalloying content on the recrystallization stop temperature of austenite in a 0.07 C, 1.4 Mn, 0.25 Si steel (in wt pct). Adapted from [45].

(b) *Niobium*

Niobium has been used as a microalloying element for many years. It has many attractive properties including significantly increasing the strength of ferrite-pearlite steels and a more recent use of

Nb as a stabilizing element, along with Ti to reduce the amount of free-carbon in solution [21], [47]. Niobium carbo-nitrides are very effective in pinning austenite grain boundaries. Solubility product calculations show Nb will precipitate as NbC and NbN at moderate rolling temperatures, usually between 1000 °C and 800 °C [5], [46], which is within the full deformation temperature regime for hot rolling. At low temperatures, undissolved carbo-nitrides act as effective grain refiners and can retard recrystallization if they are finely dispersed [5], [12], [40]. Both solute Nb and precipitation of Nb(C,N) increase strength. Vervynckt *et al*. [12] indicated that strain-induced Nb(C,N) precipitates may be on the order of 20 nm, and are too large to significantly contribute to strength increases through precipitation hardening. The low temperature precipitates are much finer and contribute to more strength increases. Niobium in solution, however, is also effective in retarding static recrystallization through solute drag effects [12], [40]. Niobium can retard the austenite-ferrite transformation, even though Nb is a ferrite stabilizer by exerting solute drag on the moving phase boundary [12].

(c) *Titanium*

Ti has a strong affinity to form nitrides, oxides and even sulphides before forming carbides [21]. With fast enough cooling, TiN will be finely dispersed. However, long reheat soak times may coarsen the precipitates and then pinning effects are small. Coarse TiN particles can have edge lengths around 5-10 μm [5]. If Ti levels are above the stoichiometric levels for TiN, Ti will also form the more soluble carbides. Titanium may form low temperature carbides and even carbosulfides which are important strengtheners [12]. There are differing views in the literature as to the amount of Ti for the most beneficial results [5], [12], [48]. Ti additions less than ca. 0.04 wt pct have shown to have very little effect on recrystallization and grain growth and may act like plain carbon steel, especially when nitrogen levels are less than 0.01 wt pct [5]. When Ti levels are around 0.10 wt pct, the effects on recrystallization are similar to Nb-bearing steels with a retardation of recrystallization due to solute Ti [5]. Titanium also plays a role controlling the austenite grain size during reheating, particularly in the heat affected zone during welding [12].

2.3.4 Carbon Equivalency

While this particular study is not specifically focused on final product applications, it is of interest to point out certain aspects that do affect product application, such as carbon equivalency. Carbon equivalency (C_{eq}) is a guideline established by the International Institute of Welding (IIW) to help determine weldability of a steel product [4], [49]. Weldability is affected by multiple alloying elements, most notably C, but is also influenced by Si, Mn, Cu, Ni, Cr, Mo, V and B. Depending on the carbon content, the other elements affect weldability and C_{eq} differently. If the C content is less than 0.12 wt pct, C_{eq} is known as $C_{eq\ Pcm}$ and is given by

$$C_{eq\ Pcm} = C + \frac{Si}{30} + \frac{Mn}{20} + \frac{Cu}{20} + \frac{Ni}{60} + \frac{Cr}{20} + \frac{Mo}{15} + \frac{V}{10} + 5B \quad (2.2)$$

where all elements are in wt pct. If the C content is greater than 0.12 wt pct, the C_{eq} is denoted by $C_{eq\ IIW}$ and is given by

$$C_{eq\ IIW} = C + \frac{Cr + Mn + V}{5} + \frac{Ni + Cu}{15} \quad (2.3)$$

where all elements are in wt pct. The maximum C_{eq} for $C_{eq\ Pcm}$ is 0.25 % and the maximum C_{eq} for $C_{eq\ IIW}$ is 0.43 %.

2.4 T_{NR} Determination Methodologies

The T_{NR} can be determined or estimated through many methods. From the literature, T_{NR} can be estimated through empirical formulas and laboratory methods. The Boratto equation [10], [50–52] is arguably the most known empirical formula to estimate T_{NR}. The laboratory methods to determine T_{NR} include [9], [11], [12], [17], [32], [53–57]: Double-hit deformation testing, multistep hot torsion testing, stress relaxation testing, tension-compression testing, laboratory rolling, and mathematical modeling. The most commonly used methods are double-hit deformation testing and multistep hot torsion testing. Examples of both testing procedures have been found in the literature, but no ASTM or ISO standards have been found for the determination of T_{NR}. The current study focuses on double-hit deformation testing to determine T_{NR}.

2.4.1 Empirical T_{NR} Determination

An empirical formula to determine or estimate T_{NR} is a useful tool, especially for rolling mill metallurgists needing to design a rolling schedule to produce steel with certain properties without extensive laboratory testing. This subsection introduces T_{NR} equations from the literature and discusses the benefits and shortcomings of each equation. Composition limits are available in the literature.

The Boratto equation [10], [50–52] is well known for estimating T_{NR} as a function of alloy content is given by,

$$T_{NR} = 887 + 464C + \left(6445Nb - 644\sqrt{Nb}\right) + \left(732V - 230\sqrt{V}\right) + 890Ti + 363Al - 357Si \quad (2.4)$$

where *C*, *Nb*, *V*, *Ti*, *Al*, and *Si* are the elements in wt pct of the steel. It should be noted that the Boratto equation does not include N, well known for precipitation and thus altering T_{NR}, even though N is almost always present in low carbon commercial steels [31]. Zaky [58] has found discrepancies with the Boratto equation at low levels of Nb and V (0.01 and 0.10 wt pct, respectively) and high levels of C (above 0.17 wt pct) [58]. A simplified equation by Bai *et al.* [9], [28] has been shown to produce reasonable T_{NR} estimates when the Boratto equation differs from experimental results. The Bai 2011 equation is given by,

$$T_{NR} = 174 \log\left[Nb\left(C + \frac{12}{14}N\right)\right] + 1444 \quad (2.5)$$

where *Nb* and *C* are the elements in wt pct of the steel and *N* is the free N remaining after TiN precipitation. Another T_{NR} equation developed by Fletcher [59], used a database of 59 different T_{NR} values for 17 alloy steels. A stepwise regression was based on the Boratto equation, ignoring pass strain:

$$T_{NR} = 849 - 349C + 676\sqrt{Nb} + 337V \ \ (R^2 = 0.72) \quad (2.6)$$

where C, Nb, and¸ V are the elements in wt pct.

Deformation parameters are known to influence T_{NR}. A strain-based model was developed by Bai [9] given by

$$T_{NR} = \beta e^{-0.36\varepsilon} \quad (2.7)$$

where β is an alloy-dependent coefficient, calculated to be 1103 °C, 1088 °C, and 1078 °C for the steels studied by Bai *et al.* and ε is strain. This model shows that small changes in pass strain can significantly affect the T_{NR}. Fletcher also developed a T_{NR} model based on pass strain and alloy content using a similar regression model as Equation (2.6), following the example of Equation (2.7) [59]:

$$T_{NR} = 203 - 310C - 149\sqrt{V} + 657\sqrt{Nb} + 683e^{-0.36\varepsilon} \quad (2.8)$$

where C, V, and Nb, are the elements in wt pct and ε is the pass strain. The coefficient β was assumed to be 1100 °C for the initial analysis. A point of caution to Fletcher's analysis: the sign on the carbon term for both Equation (2.6) and Equation (2.8) is negative, which is counterintuitive as increased carbon is known to increase precipitation thus inhibiting recrystallization and increasing the T_{NR}. While the empirical regression models may be useful to quickly predict the T_{NR} for the range of alloys used in the particular studies, they may not accurately predict T_{NR} for alloy ranges outside the studies because the empirical constants and coefficients have no true physical meaning.

2.4.2 Double-Hit Deformation Methodology

Double-hit deformation tests use cylindrical specimens in an axisymmetric compression test. The test involves reheating to ensure most precipitates dissolve back into solution, cooling to deformation temperature (T_{def}), compressing with given strain and strain rate, holding for an interpass time (t_{ip}), deforming specimen again holding everything else constant, and measuring the percent recrystallized or fraction of softening (FS) [11], [21], [57], [60–63]. Typical ranges for the testing procedure are as follows [11], [17], [47], [56], [57], [64]:

- Soak at the austenitizing temperature, 1175 °C to 1250 °C (2147 °F to 2282 °F), for a given amount of time, of 10 to 30 minutes.
- Cool to the T_{def} at a constant rate, e.g. 10 °C/s (18 °F/s).
- Hold at T_{def}, typically between 900-1200 °C (1652-2192 °F), for a given amount of time for homogenization of temperature throughout the specimen, e.g. 2 to 30 s.
- Compress specimen with strain rates ($\dot{\varepsilon}$) typically between 0.1 and 10 s^{-1} to a strain (ε) of 0.3 to 0.5.
- After the first deformation, remove the load, simulating t_{ip}, for 1 to 400 s.
- Deform the specimen again at the same temperature and strain rate to the same strain.
- Measure percent recrystallized, or fraction of softening.
- Repeat process with a new sample changing desired parameters, e.g. holding time, ε, $\dot{\varepsilon}$ or temperature.

The time between deformation hits simulates interpass time, allowing static recrystallization to occur [47]. The first deformation strain approximates a rolling pass strain, and double-hit deformation tests typically measure the fraction of softening. The softening fraction is determined by comparing the flow stress of the first and second deformation steps [57], [64]. The shape of the second curve is influenced by the amount of recrystallization and the interpass time between deformation steps. If the interpass time is long enough, complete recrystallization can occur and the flow curves should be identical. If no recrystallization or softening occurs, the second curve will be an extrapolation from the first with continually higher flow stress.

Figure 2.9 shows an example of flow stress curves with various amounts of recrystallization and softening. Four samples of a Nb microalloyed steel were tested with various t_{ip}'s ranging from 2 s to 1000 s with a T_{def} of 1000 °C [61]. All samples had roughly the same flow stress for the first deformation, as to be expected. After the respective interpass times, the samples were deformed again and their flow stress measured. The sample with t_{ip} equal to 2 s had a high flow stress for the second deformation, as if a continuation from the first deformation pass. The 20 s interpass time sample shows some softening, calculated to be 10 % using the 2% offset method described in Section 2.4.3. The sample with an interpass time of 200 s showed 40 % softening with the flow curve having slightly lower yield strength than the first deformation pass. The 1000 s interpass time sample had 100 % softening since the flow curve for the second deformation is almost identical to the curve for the first deformation.

2.4.3 Determining T_{NR} from Double-Hit Deformation Tests

The literature describes four main methods for analyzing double-hit deformation test data. The methods include[12], [17], [47], [56], [57], [63], [64]:

1. 0.2 % and 2 % offset-method
2. 5 % true strain method
3. Back extrapolation method
4. Mean flow stress method [6.3- 6.5].

Figure 2.10 gives an overview of these four methods. In Figure 2.10 fractional softening (FS) is the difference in stress for the first deformation and the stress for the second deformation normalized in some fashion given by [21], [27], [53], [63], [64], [66–69],

$$FS = \frac{\sigma_m - \sigma_r}{\sigma_m - \sigma_0} \tag{2.9}$$

where σ_0 is the stress of the first deformation step at a given strain, σ_r is the stress of the second deformation step at a given strain, and σ_m is the maximum stress as defined by the chosen method.

The variation in calculating FS depends on how each stress term is defined. In the 0.2 % and 2 % offset method, the maximum stress, σ_m, is the maximum stress from the first curve. The yield strength from the second curve at a chosen 0.2 % or 2 % offset is defined as $\sigma_{r,\,offset}$. The yield strength from the first curve at the respective 0.2 % or 2 % offset is defined as $\sigma_{0,\,offset}$.

In the back extrapolation method, the first curve is translated onto the second curve and σ_m is the maximum stress from the first curve, σ_{be} is the stress of the translated curve back to the unloading point of the first curve, and $\sigma_{0,\,0.2\%\,offset}$ is the stress of the first curve at 0.2% offset strain.

In the 5 % true strain method, $\sigma_{m,\,5\%\,TS}$ is the stress of a hypothetical second curve with no softening (i.e. an extrapolation of the first curve) at 5 % true strain, $\sigma_{0,\,5\%\,TS}$ and $\sigma_{r,\,5\%\,TS}$ are the stress values at 5 % offset of the first and second curve, respectively.

In the mean flow stress method, σ_0 and σ_r are found by calculating the area under the first and second stress-strain curves, respectively, and the "maximum stress," σ_m is the area under the hypothetical second stress-strain curve corresponding to zero softening. While the area under the stress-strain curves are really energies per unit volume, σ is the notation used to be consistent with other FS calculation methods. The 5 % true-strain method was chosen for this study because the 5 % true-strain is large enough to overcome any effects due to recovery with the remaining softening being controlled through recrystallization [11], [12], [20], [60], [64].

The amount of softening is often plotted against t_{ip} for a given temperature. Figure 2.11 shows an example of the data collected from a double-hit compression test. The data follow the expected Avrami model for recrystallization kinetics. From the graph, T_{NR} is expected to be between 950 °C and 1000 °C (1742 °F and 1832 °F) where a significant retardation of the recrystallized fraction is seen. If t_{ip} is held constant, fractional softening can be plotted as a function of the deformation temperature, T_{def}. Figure 2.12 shows percent FS as a function of T_{def}. In this example, Palmiere *et al.* followed the previously determined

method that 20 % of softening is due to recovery [21], [57], [60], therefore T_{NR} is the temperature where the fractional softening is equal to 20 %. All softening greater than 20 % is attributed to static recrystallization. From this example, the T_{NR} for the E0-0.09C steel is lower than 900 °C but the point where the curve crosses the 20 % level is not shown on the plot.

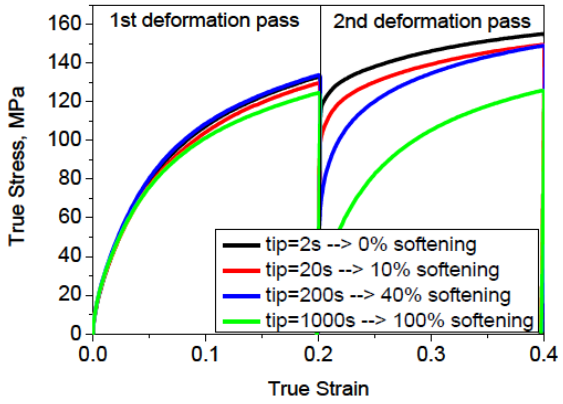

Figure 2.9 Example of flow stress for double-hit deformation tests comparing different t_{ip}'s with the fraction of softening for a Nb microalloyed steel deformed at 1000 °C. Percent softening was calculated following the 2 % offset method [65].

2.5 Physical Metallurgy behind T_{NR}

The value of T_{NR} is influenced by the interaction of four different mechanisms: Recovery, recrystallization, solute drag, and precipitation. Each mechanism depends on the others and all depend on preceding deformation, characterized by T_{def}, strain, strain rate, and composition. Figure 2.13 shows a schematic of the synergistic effects of recovery, recrystallization, deformation, and precipitation on each other. The white arrows show an accelerating effect and the grey arrows show a retarding effect. The focus of this study is primarily the effects of precipitation on recrystallization, with constant deformation parameters. The interactions of interest in the present study are circled. The influence of deformation of interest in this study primarily relates to precipitates, whether strain induced precipitation or a lack of precipitation at higher temperatures. Consequently, the role of precipitation is critical in recrystallization through grain boundary pinning causing inhibition of recrystallization. An increase in precipitation may decrease solute drag effects. As temperature decreases, recrystallization kinetics (rate) also decrease.

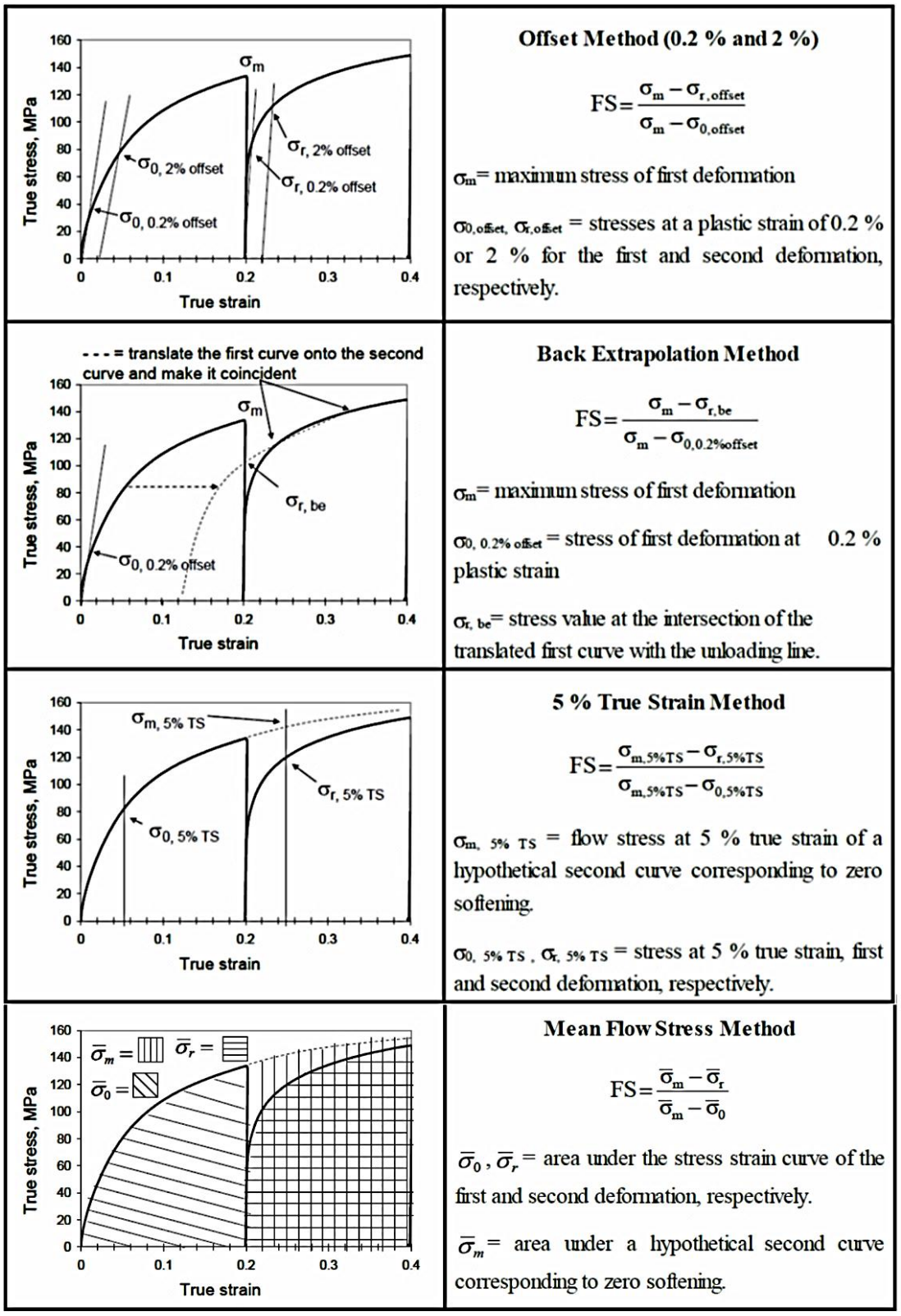

Offset Method (0.2 % and 2 %)

$$FS = \frac{\sigma_m - \sigma_{r,offset}}{\sigma_m - \sigma_{0,offset}}$$

σ_m = maximum stress of first deformation

$\sigma_{0,offset}$, $\sigma_{r,offset}$ = stresses at a plastic strain of 0.2 % or 2 % for the first and second deformation, respectively.

Back Extrapolation Method

$$FS = \frac{\sigma_m - \sigma_{r,be}}{\sigma_m - \sigma_{0,0.2\%offset}}$$

σ_m = maximum stress of first deformation

$\sigma_{0,\ 0.2\%\ offset}$ = stress of first deformation at 0.2 % plastic strain

$\sigma_{r,\ be}$ = stress value at the intersection of the translated first curve with the unloading line.

5 % True Strain Method

$$FS = \frac{\sigma_{m,5\%TS} - \sigma_{r,5\%TS}}{\sigma_{m,5\%TS} - \sigma_{0,5\%TS}}$$

$\sigma_{m,\ 5\%\ TS}$ = flow stress at 5 % true strain of a hypothetical second curve corresponding to zero softening.

$\sigma_{0,\ 5\%\ TS}$, $\sigma_{r,\ 5\%\ TS}$ = stress at 5 % true strain, first and second deformation, respectively.

Mean Flow Stress Method

$$FS = \frac{\bar{\sigma}_m - \bar{\sigma}_r}{\bar{\sigma}_m - \bar{\sigma}_0}$$

$\bar{\sigma}_0$, $\bar{\sigma}_r$ = area under the stress strain curve of the first and second deformation, respectively.

$\bar{\sigma}_m$ = area under a hypothetical second curve corresponding to zero softening.

Figure 2.10 Overview of the four most frequently used methods to calculate the fractional softening (FS) from a double deformation test (Nb microalloyed steel, Tdef = 1000 °C, tip = 200 s) [64]

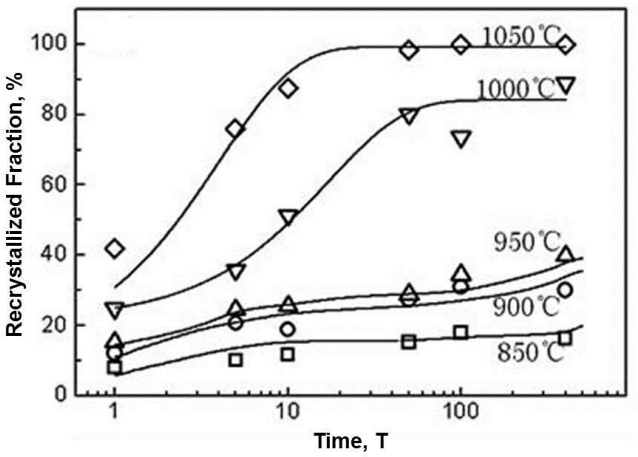

Figure 2.11 Static recrystallization kinetics curves for a high-Nb steel (0.024C-0.1Nb), d_0 = 64 μm, ε = 0.3 determined by double hit compression tests [56].

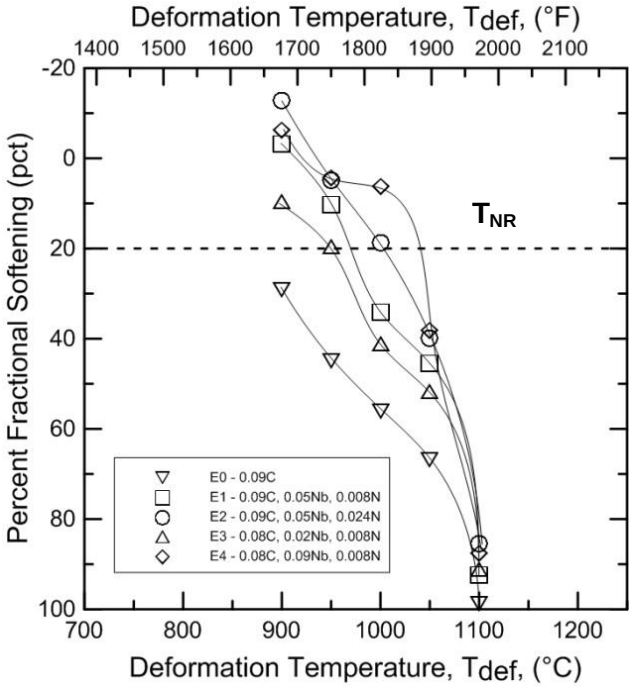

Figure 2.12 Fractional softening plot for several microalloyed steels. T_{NR} is denoted by the dotted line at 20 %. fractional softening (FS). Adapted from [57].

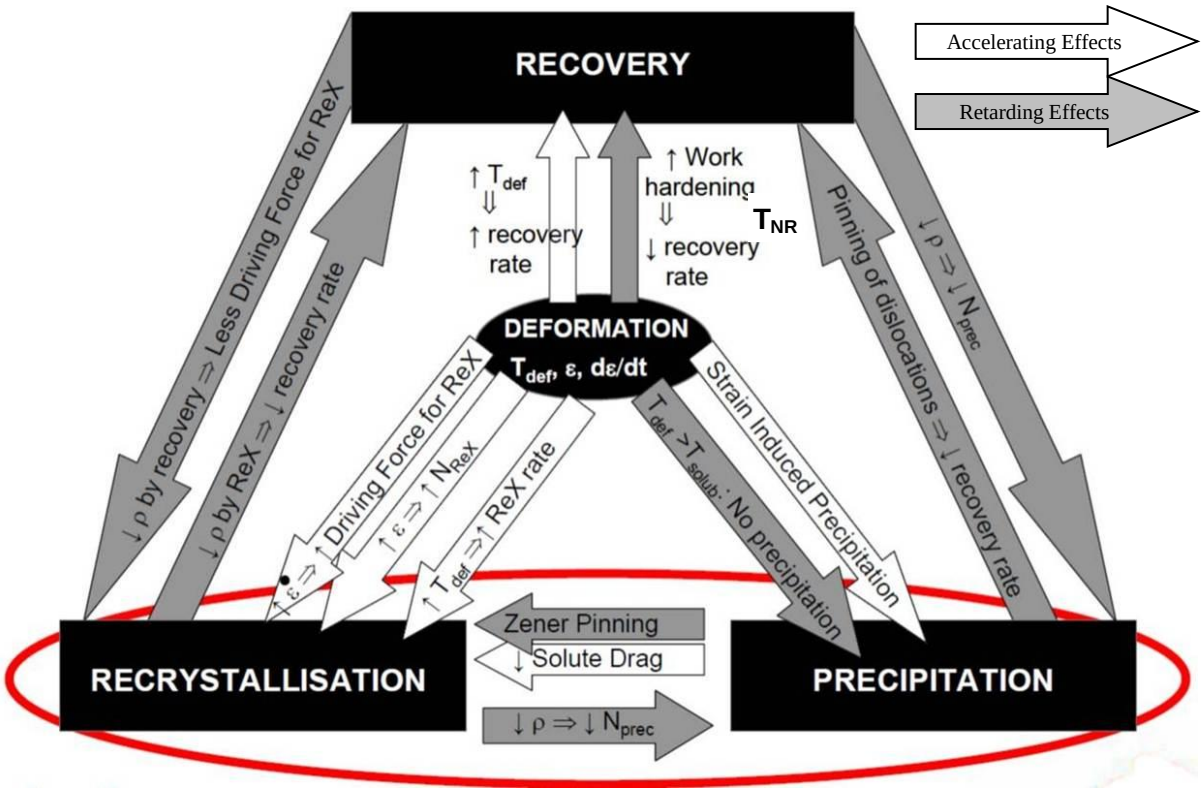

Figure 2.13 Schematic illustration of synergistic effects of recovery, recrystallization, deformation, and precipitation on each other. The white arrows show an accelerating effect and the grey arrows show a retarding effect [12].

CHAPTER 3 : EXPERIMENTAL METHODS

This chapter discusses experimental materials and methods used to determine microalloying effects on T_{NR}. The testing methodology and characterization techniques are presented in detail.

3.1 Material Design

Material for this study was laboratory produced hot-rolled microalloyed plate steel provided by Tata Steel Europe R&D. The laboratory heats were Nb-microalloyed plate steel to meet API X-70 specifications if processed correctly. Table 3.1 gives the chemical composition of the ten alloys that were produced. Each alloy is a Nb-bearing steel with varying amounts of Ti and V. The other alloying elements, e.g. C, Mn, N, etc., are relatively constant. Table 3.1 also gives the descriptive label that will be used to identify each steel.

The specific alloys were chosen to characterize precipitation and solute effects on T_{NR}. A constant level of 0.06 wt pct Nb was chosen as a base level. The Lo-Nb alloy with only 0.027 wt pct Nb was selected to allow the effects of Ti, Al and trace V on T_{NR} to be studied in a lower Nb steel. Since Ti preferentially precipitates as TiN, the Hi-Ti alloys are expected to have most of the N in TiN, which will inhibit other precipitates from forming, thereby focusing on the effect of solid solution elements on T_{NR} or the possible formation of TiC. Solubility calculations were carried out using equations presented by Turkdogan [30]. Appendix A shows the equations used and graphs of the solubility calculations used in this study. The effect of V on T_{NR} will be seen in the changes in T_{NR} by comparing the Lo-V, the Hi-V and the other alloys with trace amounts of V, i.e. the alloys containing less than 10 ppm V.

Table 3.1 – Chemical Compositions of Laboratory Nb-Bearing Microalloyed Steels in wt pct

Material ID	C	Mn	Si	Ti	Nb	V	Al	N	S	P
Lo-V	0.065	1.46	0.016	0.005	0.060	0.021	0.030	0.0046	0.0017	0.012
Hi-V	0.068	1.46	0.017	0.005	0.061	0.056	0.029	0.0040	0.0017	0.012
Lo-Nb	0.063	1.47	0.019	0.006	0.027	<0.001	0.030	0.0041	0.0017	0.012
Hi-Nb	0.066	1.46	0.020	0.007	0.060	<0.001	0.028	0.0039	0.0017	0.011
Lo-Ti	0.062	1.48	0.018	0.028	0.060	<0.001	0.032	0.0050	0.0018	0.011
Hi-Ti	0.065	1.48	0.019	0.099	0.059	<0.001	0.030	0.0040	0.0019	0.011
Lo-Ti-2	0.068	1.47	0.018	0.032	0.059	<0.001	0.031	0.0050	0.0021	0.011
Hi-Ti-2	0.078	1.46	0.022	0.110	0.059	<0.001	0.027	0.0046	0.0020	0.011
Lo-Ti-Lo-V	0.065	1.47	0.019	0.031	0.060	0.012	0.031	0.0046	0.0018	0.012
Hi-Ti-Lo-V	0.070	1.47	0.021	0.100	0.060	0.014	0.030	0.0041	0.002	0.012

3.1.1 Material Manufacturing

The laboratory heats of 60 kg each were cast into 30 kg ingots with low and high amounts of V, Nb, and Ti, respectively. The chemical compositions were determined through standard procedures implemented at Tata Steel Europe. Four additional ingots were supplied for additional study, e.g. additional low and high Ti and low and high Ti with low V. The ingots were then rolled to approximately 30 mm (1.18 in) thick plate. Figure 3.1 shows the Lo-Nb alloy as-received plate from the top. The approximate dimensions of each plate were 1016 mm ± 25 mm (40 in ± 1 in) long, 102 mm (4 in) wide, 30 mm (1.18 in) thick. The marked grid designates the portion of the plate from which torsion specimens were machined. The designation letter (C in Figure 3.1) was an alloy designation for the machine shop reference. The identification lettering in yellow (V55014A) was the alloy designation from Tata Steel Europe. Appendix B shows all as-received material photographs.

Figure 3.1 Top view of as-received Lo-Nb steel. The approximate dimensions of each plate were 1016 mm ±25 mm (40 in ± 1 in) long, 102 mm (4 in) wide, 30 mm (1.18 in) thick. The marked grid designates the portion of the plate from which torsion specimens were machined. The designation letter (C in this case) was an alloy designation for the machine shop reference. The designation lettering in yellow (V55014A) was the alloy designation from Tata Steel Europe.

3.1.2 As-Received Material Characterization

Two sections from each plate were cut and sent to SSAB Americas for chemical analysis to verify the chemical composition. Standard Leco combustion analysis and optical emission spectroscopy (OES) were used to confirm the carbon, nitrogen, sulfur, and remaining elements, respectively. The samples were approximately 25.4 x 25.4 x 3.2 mm (1 x 1 x 1/8 in) for Leco and 38 x 38 x 25.4 mm (1.5 x 1.5 1 in) for OES analysis. The sections were taken from the middle of the plate width.

3.2 Laboratory Testing to Determine T_{NR}

Double-hit deformation tests were conducted to determine T_{NR} for this study using the Gleeble® 3500 system in the standard pocket-jaw set-up.

3.2.1 Double-Hit Compression

With the compression capabilities of the Gleeble® 3500, the following procedure was used:

- Heat to austenitizing temperature of 1250 °C (2282 °F) at 10 °C/s (18 °F/s).
- Soak at 1250 °C (2282 °F) for 10 minutes to ensure most precipitates have gone into solution.
- Cool to a single deformation temperature in the range of 1200 °C-750 °C (2192 °F-1382 °F) at 50 °C (122 °F) decrements at a rate of 1.25 °C/s (2.25 °F/s).
- Deform with strain (ε) of 0.2, a strain rate ($\dot{\varepsilon}$) of 5 s^{-1} followed by a hold time (t_{ip}) of 5 s.
- Deform again with same parameters of ε of 0.2 and $\dot{\varepsilon}$ of 5 s^{-1}.
- Air cool sample to room temperature.

Three samples of each alloy were tested at each temperature to ensure reproducibility of results. Once the general fractional softening curve was formed, the process was repeated around the T_{NR} with 25 °C temperature steps to more accurately determine the T_{NR}. Figure 3.2 shows a schematic of the heating and deformation schedule for the double-hit deformation tests. The parameters chosen in this study fall within common parameter ranges for both double hit deformation testing and multistep hot torsion testing [9], [17], [47], [56], [57], [64], [65]. The reaustenitizing soak temperature was chosen to ensure most precipitates dissolve back into solution. The exception includes TiN for most alloys, see Section 2.3.2. A soak time of 10 min was commonly used in the literature [9], [65] for the specimen geometry chosen, which ensures uniform heating throughout the gauge section. The cooling rate of 1.25 °C/s is consistent with a previously determined cooling rate for multistep hot torsion testing, which gives a t_{ip} of 20 s for torsion testing when deforming at 25 °C decrements [9], [10], [38], [64], [70–73]. The ε and $\dot{\varepsilon}$ are typical values for both double hit deformation testing and multistep hot torsion testing [9], [64], [65].

Figure 3.3 shows true stress-true strain curves for Lo-V alloy at three different test temperatures. The "d03" designation indicates the third test at each condition. The 1200 °C curves are practically identical, indicating complete recrystallization. The second deformation curve at 1000 °C is slightly higher, indicating some strengthening. A strength increase is most evident in the 750 °C curve, where the second deformation step is almost an extrapolation of the first, indicating very little recrystallization.

3.3 Specimen Geometry and Fixturing

Cylindrical compression samples were machined in the rolling direction from as-received hot rolled plate, 10 mm (0.394 in) diameter by 15 mm (0.591 in) long. The diameter to height ratio is 2:3 to limit the potential for buckling during deformation [74]. Appendix C shows a detailed view of the specimen geometry. Figure 3.4 shows a perspective drawing of the ISO-T™ compression fixture that was

used in the Gleeble® 3500. The majority of the compression fixture is stainless steel with a tungsten carbide (WC) platen assembly, referred to as the ISO-T^{TM} anvil assembly [75].\

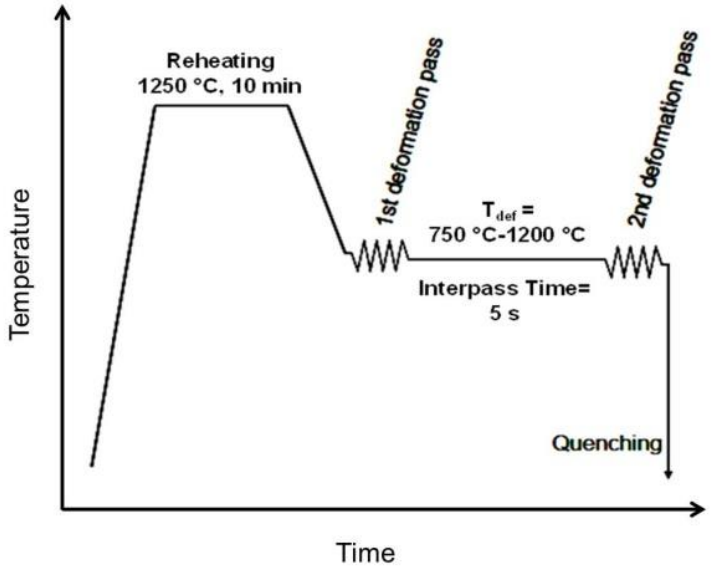

Figure 3.2 Schematic of double-hit deformation test, reheating to 1250 °C for 10 minutes, cooling to deformation temperature between 750 °C and 1200 °C with 5 s interpass time.

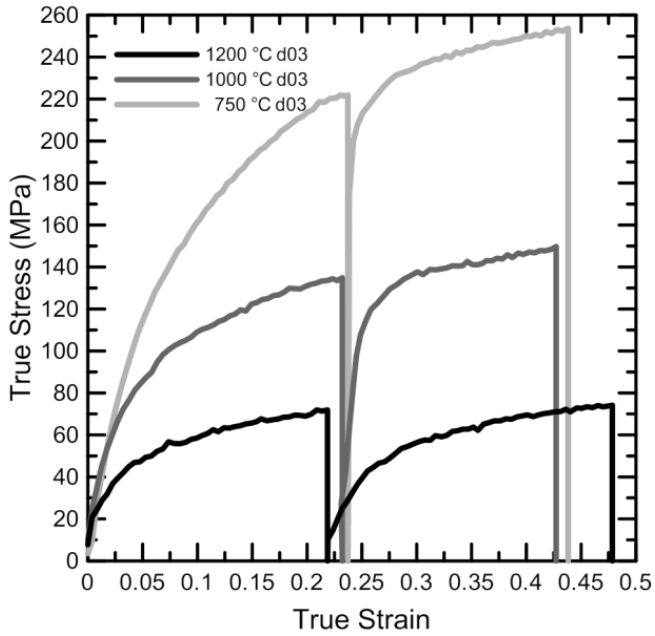

Figure 3.3 Schematic of double-hit deformation test, reheating to 1250 °C for 10 minutes, cooling to deformation temperature between 750 °C and 1200 °C with 5 s interpass time.

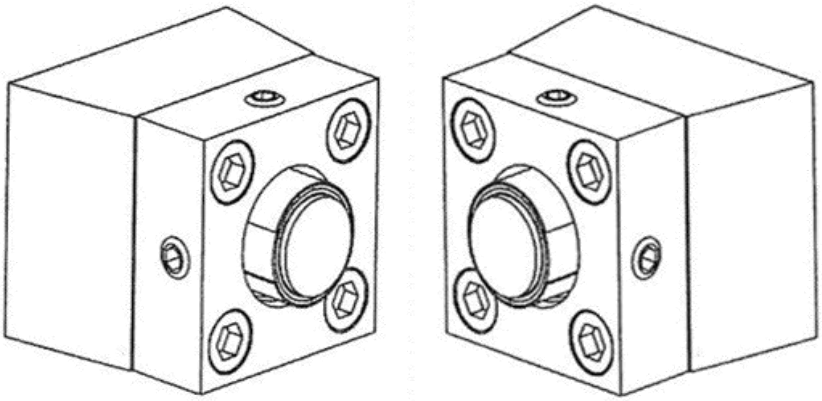

Figure 3.4 Schematic of the assembled ISO-T™ compression fixture [75].

Figure 3.5 shows a schematic of the uniaxial compression setup used in testing. A diffusion barrier/lubricant system was used between the specimen and the WC platens. A single layer of 0.254 mm (0.010 in) graphite foil was used as a lubricant between two layers of 0.254 mm (0.010 in) tantalum (Ta) foil, which acted as a diffusion barrier between the graphite, the WC platens, and the specimen. A thin layer of nickel-based anti-seize compound was applied on each interface to ensure all components stayed in place during setup and help in the release of the Ta foil from the WC platens after testing. A type K control thermocouple was spot welded on the surface at the center of each specimen. The thermocouple wire was 0.254 mm (0.010 in) in diameter with a PFA (fluorocarbon polymer) coating to prevent shorting between the wires away from the specimen. Each thermocouple wire was insulated with a 25 mm (1 in) section of mullite ($3Al_2O_3$-$2SiO_2$) ceramic tubing, 0.508 mm (0.020 in) inner diameter, resistant to 1600 °C (2910 °F).

The melting point of the PFA coating is around 300 °C (572 °C) [76]. While the low melting temperature was generally not an issue, radiated heating from the stainless steel fixturing occasionally affected the integrity of the PFA coating just above the mullite ceramic tubing. Therefore, at least 50.8 mm (2 in) of thermocouple wire was cut off after each test, which was more than sufficient to ensure the in-use thermocouple wire would not be subjected to alloy diffusion into or out of the wire and specimen [77]. For consistency, the positive lead, nickel-chromium (Ni-Cr), was toward the operator while the test was running.

3.4 T_{NR} Determination

Using the 5 % True Strain Method to determine FS from double-hit deformation curve as described in Section 2.4.3, FS was determined for each of the 10 alloys at each testing temperature. Figure 3.6 shows the true stress-true strain curve plot of one Lo-V alloy test with T_{def} of 1000 °C. The values for 5 % true

strain for the first and second curves are denoted by σ_0 and σ_r, respectively as well as the estimated stress of the extrapolated first curve at 5 % true strain of the second curve without softening, denoted by σ_m. From this double-hit test, σ_0 is 86 MPa, σ_r is 131 MPa, and σ_m is 142 MPa. The FS is found to be 20 %.

$$FS = \frac{\sigma_m - \sigma_r}{\sigma_m - \sigma_0} = \frac{142 - 131}{142 - 86} * 100\ \% = 20\ \% \tag{3.1}$$

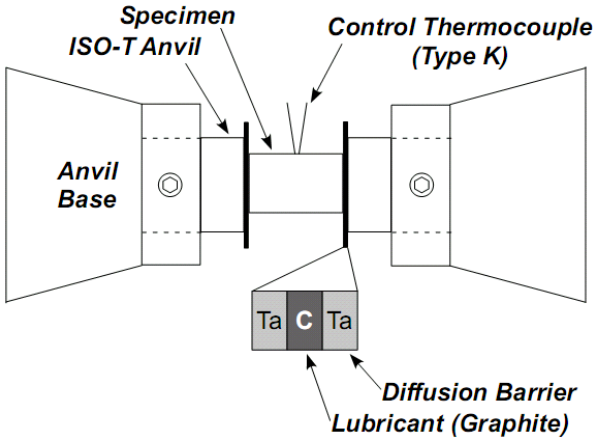

Figure 3.5 Schematic of ISO-T^{TM} compression setup. A type K control thermocouple was spot welded to the surface of each specimen at the center. A layer of tantalum (Ta) foil was used as a diffusion barrier between the specimen and the graphite (C) lubricant as well as the tungsten carbide platens and the graphite [78].

3.5 Compression Test Evaluation

Figure 3.7 shows a compression sample (a) before and (b) after testing. Lubrication and diffusion barriers were used as described in Section 3.3. A true strain of 0.2 was targeted for each deformation pass of the double-hit deformation test, for a total true ε of 0.4. However, slightly more deformation was achieved in some alloys at lower temperatures. A constant $\dot{\varepsilon}$ of 5 s^{-1} was achieved by use of a 4 mm (0.1575 in) slack coupler which allowed the hydraulic ram to retract slightly and accelerate appropriately before compressing the test specimen. This retraction ensured a constant and controlled ram velocity upon initial contact of the specimen and during compression.

Following a procedure outlined by Rothleutner [78] , shape coefficients are used to assess the validity of compression tests by analyzing the shape of the deformed specimen compared to the original [74]. Another key aspect of shape coefficients is to confirm the alignment of the platens during testing. The barreling coefficient, *B*, is the ratio of the final volume of the specimen over the initial volume calculated from mean heights, h_f and h_o, and the mean diameters, d_f and d_o, respectively, as:

$$B = \frac{h_f d_f}{h_o d_0} \tag{3.2}$$

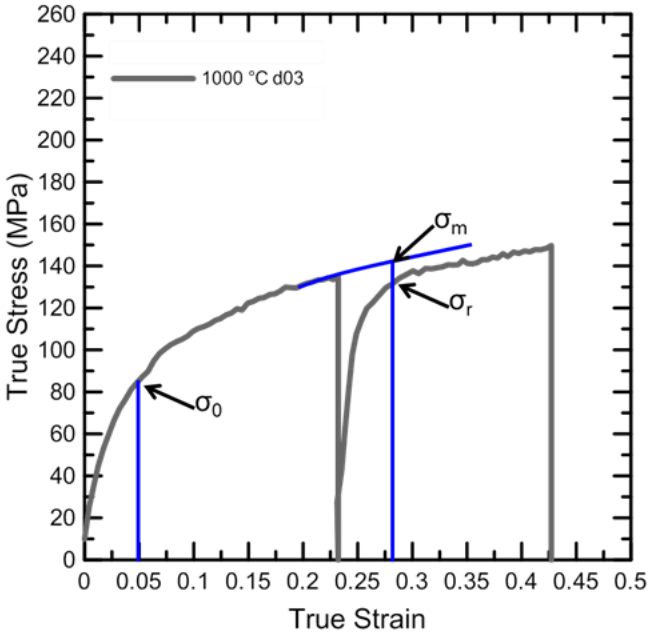

Figure 3.6 True stress- true strain plot of Lo-V alloy at 1000 °C. The label d03 designates the third test of this condition. The values for 5 % true strain for the first and second curves are denoted by σ_0 and σ_r, respectively as well as the estimated stress of the extrapolated first curve at 5 % true strain of the second curve without softening, denoted by σ_m.

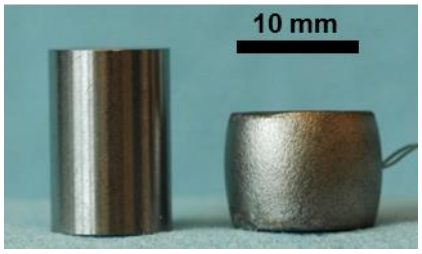

(a) (b)

Figure 3.7 Double-hit deformation specimen (a) before and (b) after testing on a Gleeble® 3500. Original samples were machined to 10 mm (0.394 in) diameter by 15 mm (0.591 in) long and then compressed to a total target strain of 0.4, for a target height of 10 mm long.

Three measurements for each dimension in the initial and final specimen geometry were recorded. Barreling is caused by both friction at the specimen surface preventing radial expansion at the specimen/platen interface and thermal gradients within the specimen [6], [74].

The ovality coefficient, O_v, is defined as the ratio of maximum to minimum final diameters, d_f^{max} and d_f^{min}, respectively, of the deformed specimen determined by:

$$O_v = \frac{d_f^{max}}{d_f^{min}} \tag{3.3}$$

Ovality is influenced by texture and microstructural effects on the deformation behavior, most commonly seen in hexagonal close packed metals.

The height coefficient, *H*, is defined as the ratio of the standard deviation of four height measurements, Sh_f, to the mean height, h_f, of the specimen after testing and gives an indication of parallelism of the specimen and the platens, defined as:

$$H = \frac{Sh_f}{h_f} \tag{3.4}$$

Results for the shape coefficients are presented in Appendix C, Table C-3.

3.6 Austenite Grain Morphology Evaluation

The testing procedure in Section 3.5 was repeated on additional samples, where quenching was employed to "freeze" the austenite grains for later analysis, forming martensite. The microstructural changes were examined above and below the predicted T_{NR}. The laboratory-made steels have low impurities, coupled with low carbon, providing limited hardenability and difficulty revealing austenite grains. Heat treating of the specimens prior to grinding and polishing was necessary. Specimens were heat treated to 500 °C (958 °F) just below the embrittlement nose [1], [79], [80] for 24 hours to allow phosphorous and other solute atoms to diffuse to the prior austenite grain boundaries.

A variety of quenching fluids and rates were evaluated in combination with various heat treatments and etching reagents to reveal prior austenite grains. Appendix C shows the post testing procedure and the effective results associated with the various processes.

3.7 Microstructure Verification

Light optical microscopy (LOM) was used to characterize both the as-received material and the quenched double-hit deformation specimens. As received specimens were analyzed transverse to the original plate rolling direction. Double-hit deformation specimens were analyzed transverse to the compression axis, simulating transverse to the rolling direction.

3.7.1 As Received Material

As received material was cut into approximately 1 cm^3 sections. The sections were mounted in standard 32 mm (1.25 in) Bakelite® mounts, ground flat, and polished to a 1 µm finish with diamond

suspension. The samples were etched with a 2 % nital solution for 3-5 seconds, rinsed with methanol and dried with compressed air.

3.7.2 Quenched Double-Hit Deformation Specimens

The quenched double-hit deformation specimens were used to determine prior austenite grain (PAG) size and morphology. A modified Béchet–Beaujard reagent [12], [79], [81], [82] was used as the etching solution. The etchant contains a 4 % saturated aqueous solution of picric acid, 2 % hydrochloric acid, 2 %Teepol (a wetting agent) and 92 % deionized water. The etchant was heated to 65-70 °C and agitated lightly. Samples were immersed for 20-30 s, rinsed with methanol and dried with compressed air. Some samples required light back polishing to remove the appearance of martensite while retaining the PAGs.

CHAPTER 4 : RESULTS

This chapter presents and discusses the experimental results obtained from characterization and laboratory testing described in Chapter 3. Metallography and material characterization of the as-received material are presented followed by fractional softening results of the double-hit deformation tests, T_{NR} range for each alloy and micrographs of the deformed specimens confirming the T_{NR} range.

4.1 As-Received Material Characterization

The as-received material was sectioned for chemical analysis through Leco combustion analysis and optical emission spectroscopy (OES) chemical testing and light optical microscopy. Exact procedures for the analyses are described in Chapter 3.

4.1.1 Chemical Analysis

Two sections from each plate were sent to SSAB Americas for chemical analysis. Standard Leco combustion analysis tested the amount of C, S, and N in the steel. Optical emission spectroscopy (OES) was used to confirm the remaining elements. Appendix B shows the original chemical analysis provided by Tata Steel Europe along with the results provided by SSAB Americas. The results from the Leco analysis confirmed the concentration of C, S, and N provided by Tata Steel Europe. The remaining elements had good agreement for all alloys, with the exception of the V content. The OES analysis from SSAB for V content was consistently higher by 20-30 ppm for each alloy. This result may be due to a calibration discrepancy or the location of specimen in the plate.

Since the difference was consistent in all alloys and the variation in V measurement is still low, the results are not expected to significantly affect the value of T_{NR}. Any effect would be in the same direction by approximately the same magnitude for all alloys in question. The overall chemistries are in agreement so the original alloying percentages were used for any calculations.

Table 4.1 shows the values of carbon equivalency for the ten alloys used in this study. Since the carbon content is less than 0.12 wt pct for all alloys, the $C_{eq\ Pcm}$ equation was used. The maximum allowable $C_{eq\ Pcm}$ is 0.25 %. Each of the steels is less than the maximum allowable carbon equivalency.

4.1.2 Microstructure

Metallographic samples of the ten alloys in the as-received condition were used to obtain approximate grain sizes and general microstructural constituent identification. The expected microstructure for each alloy was primarily ferrite with some pearlite or bainite colonies from the air-cooled hot-rolled condition. Figure 4.1 shows representative light optical micrographs for the as-received (a) Lo-V and (b) Hi-V alloys from the center of the plate width etched in a 2 % nital solution for

3-5 s. As expected, the microstructure is mostly ferrite with some pearlite or bainite colonies. Appendix B shows the as-received micrographs for all alloys tested in this study.

Table 4.1 – Carbon Equivalency for Carbon less than 0.12 wt pct

Material ID	$C_{eq\ Pcm}$ (%)
Lo-V	0.141
Hi-V	0.147
Lo-Nb	0.137
Hi-Nb	0.140
Lo-Ti	0.137
Hi-Ti	0.140
Lo-Ti-2	0.142
Hi-Ti-2	0.152
Lo-Ti-Lo-V	0.140
Hi-Ti-Lo-V	0.146

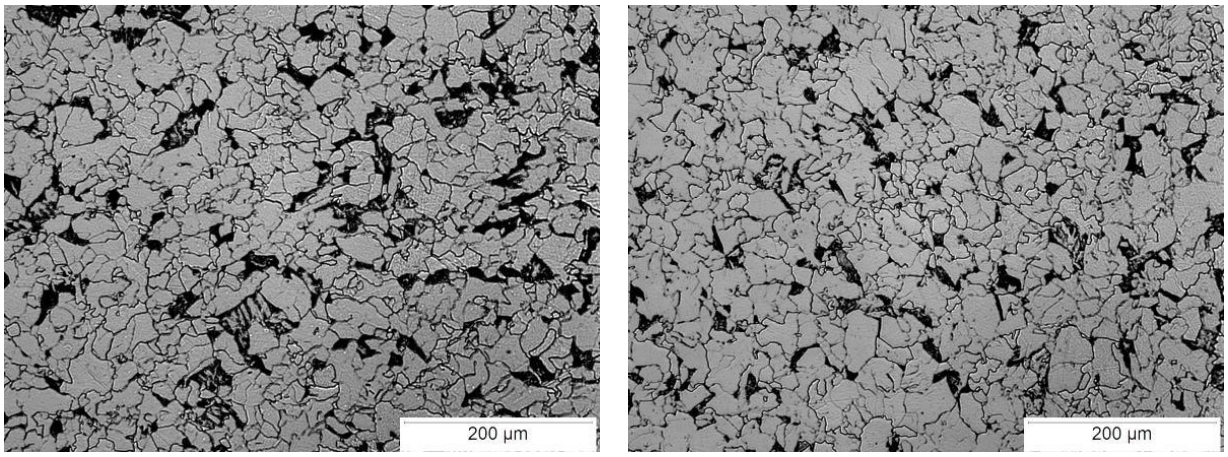

(a) (b)

Figure 4.1 Representative light optical micrographs for the as-received (a) Lo-V and (b) Hi-V alloys from the center of the plate width etched in a 2 % nital solution for 3-5 s.

4.2 Laboratory Testing to Determine T_{NR}

Following the procedure outlined in Section 3.2.1, double-hit deformation tests were conducted on a Gleeble® 3500 to determine fractional softening (FS) and ultimately T_{NR}.

4.2.1 Fractional Softening

Through double-hit deformation testing, T_{NR} is determined by finding the percent fractional softening (FS) at various temperatures and identifying the temperature where FS is equal to 20 % [12], [21],

[47], [57], [60], [67], [68], [83]. Percent fractional softening is found by comparing the two stress-strain curves in a double-hit deformation test, as outlined in Section 0. Three samples were tested at each condition to ensure reproducibility of results.

Fractional softening for the ten alloys at each temperature was calculated using Equation (2.4). Table 4.2 to Table 4.11 show the FS for each test, the reported average for each temperature, and the range of FS for each condition. Blanks in the tables indicate a non-useable test. The temperatures above and below 20 %, FS, i.e. around T_{NR}, are highlighted. Figures 4.2 to 4.11 show the plots of FS versus T_{def} for each alloy. The circles indicate the average of the three conditions with the range of the three conditions denoted by the uncertainty limits.

Table 4.2 – Percent Fractional Softening of the Lo-V Alloy at Various Test Temperatures

Temp (°C)	Run 1 FS (%)	Run 2 FS (%)	Run 3 FS (%)	Average FS (%)	FS Range (%)
1200	100		100	100	100
1150		83	82	82	82-83
1100	76	79	81	79	76-81
1050	54	51	50	52	50-54
1000	24	20	16	20	16-24
950	10	13	15	12	10-13
900	14	6	11	10	6-14
850	7	7	6	7	6-7
800	3	0	3	2	0-3
750	4	4	2	3	2-4

Table 4.3 – Percent Fractional Softening of the Hi-V Alloy at Various Test Temperatures

Temp (°C)	Run 1 FS (%)	Run 2 FS (%)	Run 3 FS (%)	Average FS (%)	FS Range (%)
1200	99	91	94	95	91-95
1150	93	87		90	87-93
1100	72	70	74	72	70-74
1050	40	45	34	40	34-45
1000	14	16		15	14-16
950	14	8	13	11	8-14
900	14	13		14	13-14
850	8	6	11	9	6-11
800	7		7	7	7
750		8	5	7	5-8

Table 4.4 –Percent Fractional Softening of the Lo-Nb Alloy at Various Test Temperatures

Temp (°C)	Run 1 FS (%)	Run 2 FS (%)	Run 3 FS (%)	Average FS (%)	FS Range (%)
1200	90	86	94	90	86-94
1150	89	88	90	89	88-90
1100	76	80	76	78	76-80
1050	67	58		63	58-67
1000	34	34	35	34	34-35
950		14	17	15	14-17
900	11	18	16	15	11-18
850	13	11	9	11	9-13
800	12	9	13	11	9-13
750	12	9		11	9-12

Table 4.5 – Percent Fractional Softening of the Hi-Nb Alloy at Various Test Temperatures

Temp (°C)	Run 1 FS (%)	Run 2 FS (%)	Run 3 FS (%)	Average FS (%)	FS Range (%)
1200		95	85	90	85-95
1150	88	84	89	87	84-89
1100	79	70	78	76	70-79
1050	49		53	51	49-53
1000	25	19	17	20	17-25
950	13	11	10	11	10-13
900	9	10	10	10	9-10
850	5	6	5	5	5-6
800	7	5	6	6	5-7
750	7	4	8	6	4-8

Table 4.6 – Percent Fractional Softening of the Lo-Ti Alloy at Various Test Temperatures

Temp (°C)	Run 1 FS (%)	Run 2 FS (%)	Run 3 FS (%)	Average FS (%)	FS Range (%)
1200	100		93	97	93-100
1150	86	82	88	85	82-88
1100	70	78	70	73	70-78
1050	57	51	57	55	51-57
1000	26	23	24	24	23-26
950	12	11	11	11	11-12
900	15	14	14	14	14-15
850	10	9	10	10	9-10
800	6	8	5	6	5-8
750	8	4	4	5	4-8

Table 4.7 – Percent Fractional Softening of the Hi-Ti Alloy at Various Test Temperatures

Temp (°C)	Run 1 FS (%)	Run 2 FS (%)	Run 3 FS (%)	Average FS (%)	FS Range (%)
1200	82	86	76	81	76-86
1150	86	77	76	80	76-86
1100	78	82	88	82	78-88
1050	28	36	44	36	28-44
1000	17	17	13	16	13-17
950		9	10	9	9-10
900	14		15	14	14-15
850	8	5	6	6	5-8
800			9	9	9
750	2	1	4	2	1-4

Table 4.8 – Percent Fractional Softening of the Lo-Ti-2 Alloy at Various Test Temperatures

Temp (°C)	Run 1 FS (%)	Run 2 FS (%)	Run 3 FS (%)	Average FS (%)	FS Range (%)
1200	84	72	87	81	72-87
1150	85	88	87	87	85-88
1100	90	79	75	81	75-90
1050	36	52	64	51	36-64
1000	15	15	16	15	15-16
950	14	10	16	13	10-16
900	15	15	15	15	15
850	10	7	12	10	7-12
800	6		7	7	6-7
750	12	5	9	8	5-12

Table 4.9 – Percent Fractional Softening of the Hi-Ti-2 Alloy at Various Test Temperatures

Temp (°C)	Run 1 FS (%)	Run 2 FS (%)	Run 3 FS (%)	Average FS (%)	FS Range (%)
1200	94	92	93	93	92-94
1150		79	98	89	79-98
1100	81	55	73	69	55-81
1050	34	59	51	48	34-59
1000	15	10	10	12	10-15
950	12	13	12	12	12-13
900	10	11	10	10	10-11
850	2	3	3	3	2-3
800	3	3	3	3	3
750	2	-1	-1	0	-1-2

Table 4.10 – Percent Fractional Softening of the Lo-Ti-Lo-V Alloy at Various Test Temperatures

Temp (°C)	Run 1 FS (%)	Run 2 FS (%)	Run 3 FS (%)	Average FS (%)	FS Range (%)
1200	74	74	70	73	70-74
1150	73	72	67	71	67-73
1100	69	55	65	63	55-69
1050	53	49	54	52	49-54
1000	17	18	15	17	15-18
950	11	12	12	12	11-12
900	13	13	13	13	13
850	7	8	13	9	7-13
800	3	7	8	6	3-8
750	12		7	10	7-12

Table 4.11 – Percent Fractional Softening of the Hi-Ti-Lo-V Alloy at Various Test Temperatures

Temp (°C)	Run 1 FS (%)	Run 2 FS (%)	Run 3 FS (%)	Average FS (%)	FS Range (%)
1200	94		95	94	94-95
1150	97	87		92	87-97
1100	76	87	78	80	76-87
1050		24	39	31	24-39
1000	10	14	20	15	10-20
950	12	15	14	13	12-15
900	9	13	12	12	9-13
850	10	4	4	6	4-10
800	2	1	2	2	1-2
750	3	2	1	2	1-3

Tests were conducted just above and just below T_{NR} for the primary six alloys to better determine T_{NR}. Figure 4.12 shows the FS for the six main alloys at 25 °C increments around T_{NR}. One sample per condition was tested. The curves for each alloy appear to show two distinct slopes – one above T_{NR} and one below T_{NR}. The FS slope above T_{NR} appears shallower than the steeper slope below T_{NR}. The exception of this trend is the Lo-Nb alloy. The Lo-Nb alloy shows a T_{NR} around 962 °C, much lower than the other materials tested. The Lo-V, Hi-Nb, and Lo-Ti alloys show similar recrystallization temperatures, between 1000 °C and 1015 °C. The T_{NR} for the Hi-Ti alloy is around 1025 °C, with the T_{NR} of the Hi-V alloy near 1038 °C. The Lo-Nb steel would show a similar slope difference above T_{NR} had a point been plotted at 925 °C.

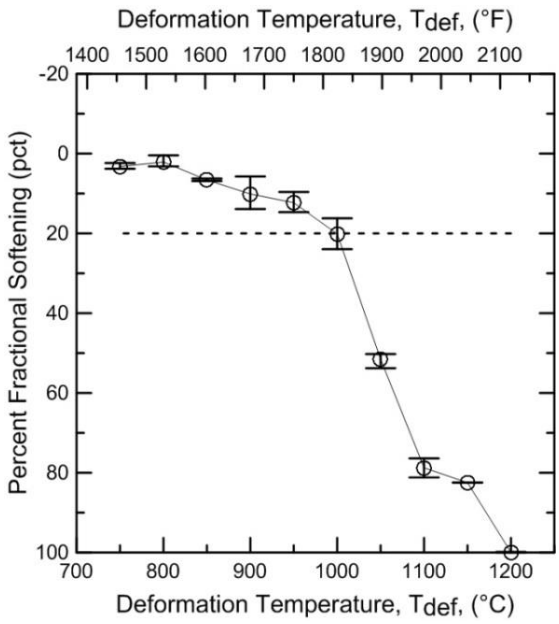

Figure 4.2 Fractional softening plot for the Lo-V alloy. T_{NR} is denoted by the dotted line at 20 %. FS which intersects close to 1000 °C. The circles indicate the average of the three conditions with the maximum and minimum of the three conditions denoted by the uncertainty limits.

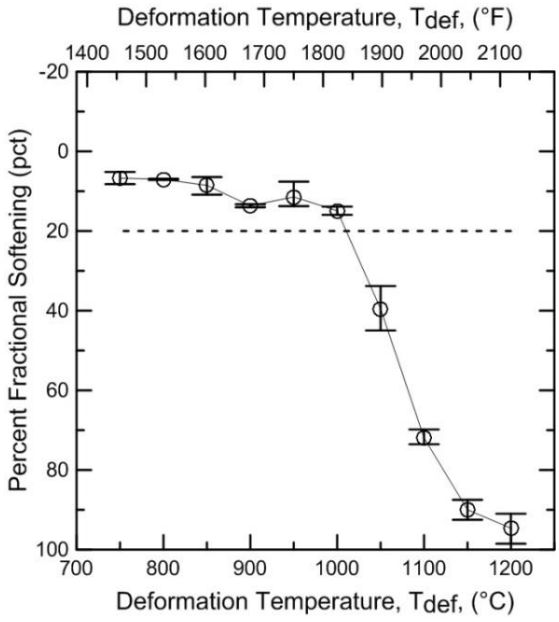

Figure 4.3 Fractional softening plot for the Hi-V alloy. T_{NR} is denoted by the dotted line at 20 %. FS which intersects between 1000 °C and 1050 °C. The circles indicate the average of the three conditions with the maximum and minimum of the three conditions denoted by the uncertainty limits.

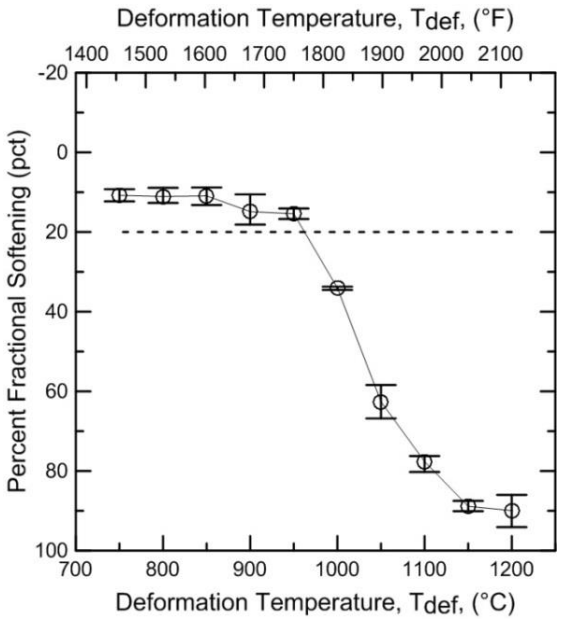

Figure 4.4 Fractional softening plot for the Lo-Nb alloy. T_{NR} is denoted by the dotted line at 20 %. FS which intersects between 950 °C and 1000 °C. The circles indicate the average of the three conditions with the maximum and minimum of the three conditions denoted by the uncertainty limits.

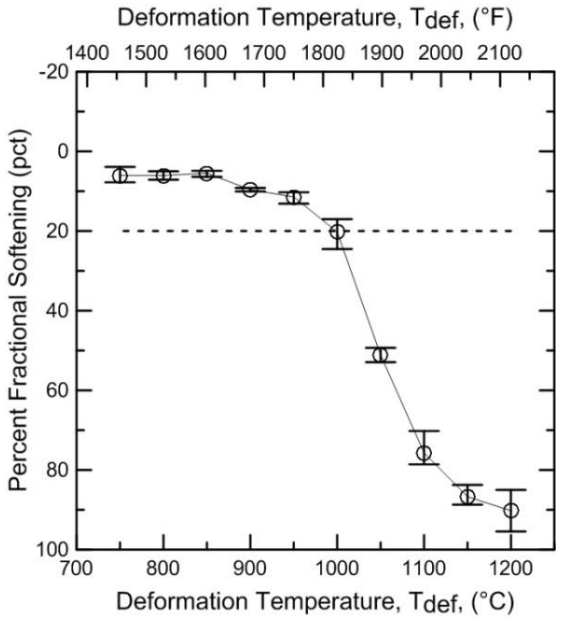

Figure 4.5 Fractional softening plot for the Hi-Nb alloy. T_{NR} is denoted by the dotted line at 20 %. FS which intersects close to 1000 °C. The circles indicate the average of the three conditions with the maximum and minimum of the three conditions denoted by the uncertainty limits.

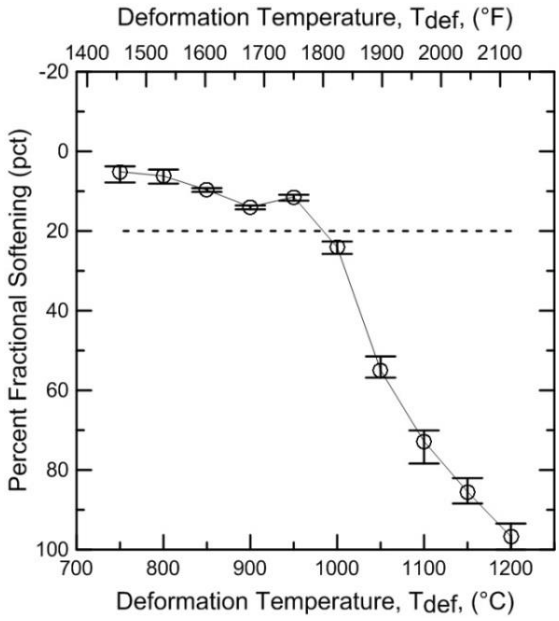

Figure 4.6 Fractional softening plot for the Lo-Ti alloy. T_{NR} is denoted by the dotted line at 20 %. FS which intersects between 950 °C and 1000 °C. The circles indicate the average of the three conditions with the maximum and minimum of the three conditions denoted by the uncertainty limits.

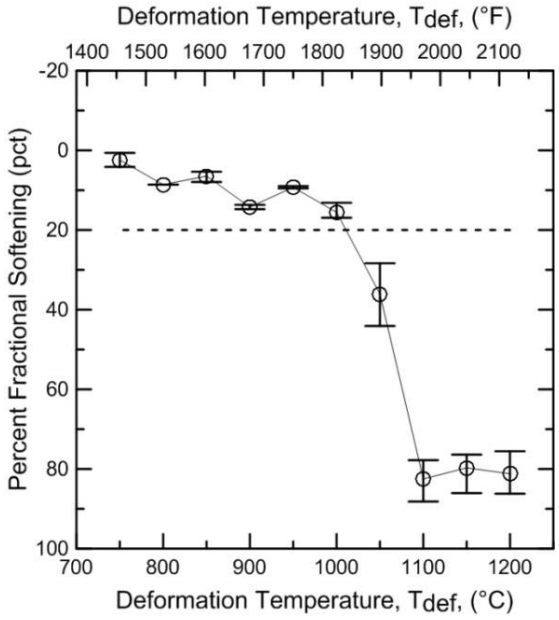

Figure 4.7 Fractional softening plot for the Hi-Ti alloy. T_{NR} is denoted by the dotted line at 20 %. FS which intersects between 1000 °C and 1050 °C. The circles indicate the average of the three conditions with the maximum and minimum of the three conditions denoted by the uncertainty limits.

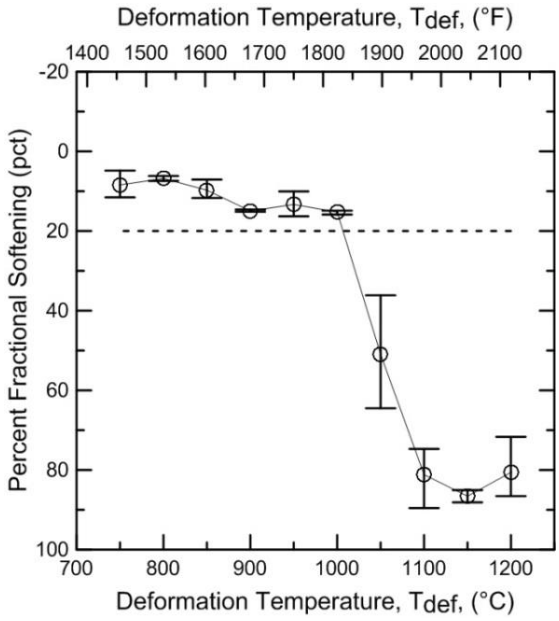

Figure 4.8 Fractional softening plot for the Lo-Ti-2 alloy. T_{NR} is denoted by the dotted line at 20 %. FS which intersects between 1000 °C and 1050 °C. The circles indicate the average of the three conditions with the maximum and minimum of the three conditions denoted by t the uncertainty limits.

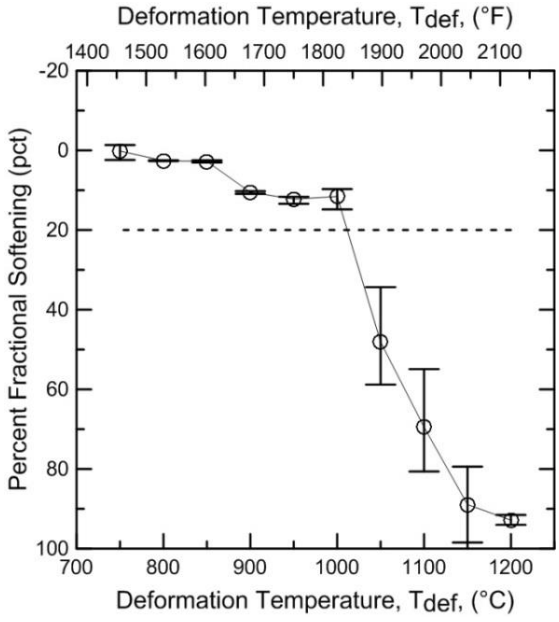

Figure 4.9 Fractional softening plot for the Hi-Ti-2 alloy. T_{NR} is denoted by the dotted line at 20 %. FS which intersects between 1000 °C and 1050 °C. The circles indicate the average of the three conditions with the maximum and minimum of the three conditions denoted by the uncertainty limits.

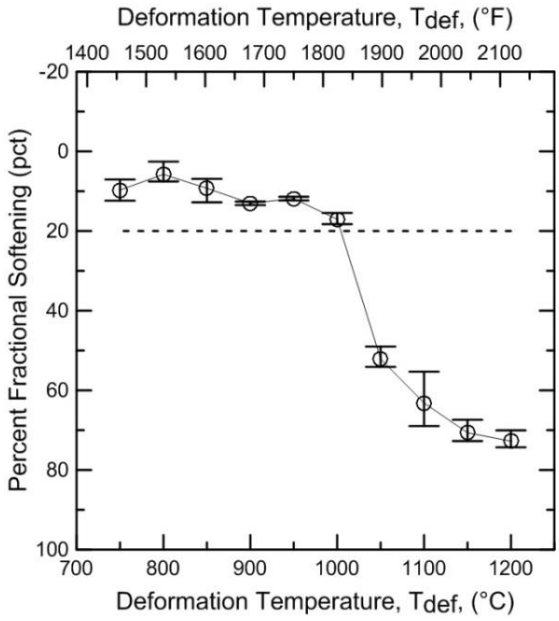

Figure 4.10 Fractional softening plot for the Lo-Ti-Lo-V alloy. T_{NR} is denoted by the dotted line at 20 %. FS which intersects between 1000 °C and 1050 °C. The circles indicate the average of the three conditions with the maximum and minimum of the three conditions denoted by the uncertainty limits.

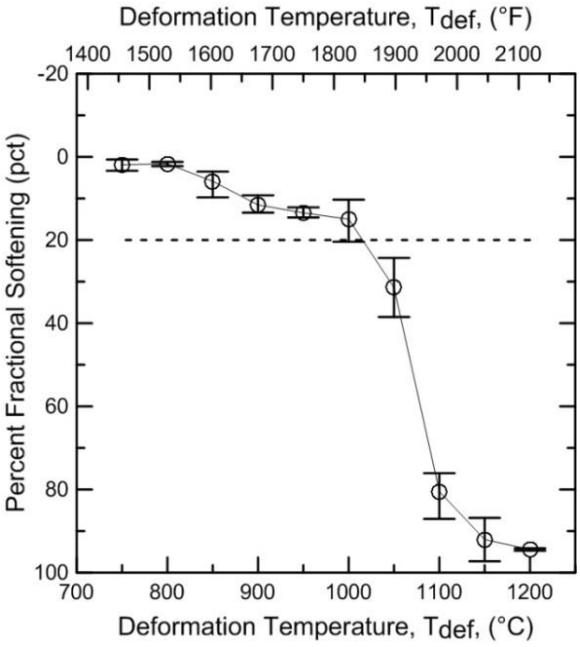

Figure 4.11 Fractional softening plot for the Hi-Ti-Lo-V alloy. T_{NR} is denoted by the dotted line at 20 %. FS which intersects between 1000 °C and 1050 °C. The circles indicate the average of the three conditions with the maximum and minimum of the three conditions denoted by the uncertainty limits.

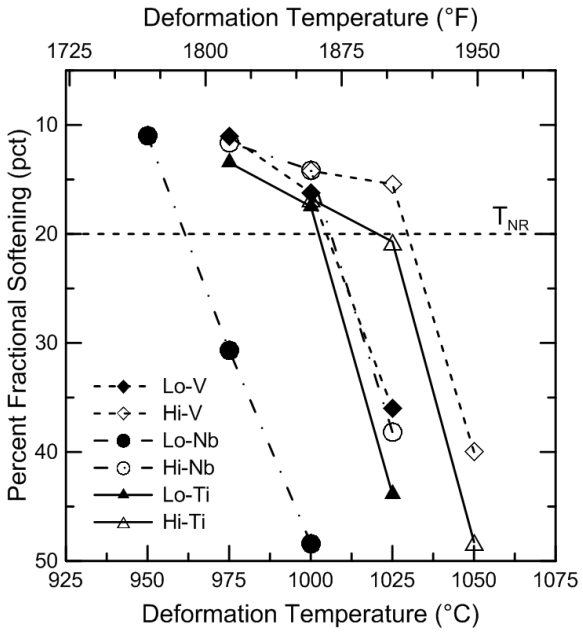

Figure 4.12 Fractional softening plot for the Lo-V, Hi-V, Lo-Nb, Hi-Nb, Lo-Ti, and Hi-Ti alloys just above and just below the previously determined T_{NR} range. The T_{NR} for most alloys is between 1000 °C and 1025 °C.

4.2.2 T_{NR} Results

The T_{NR} was found for each alloy through double-hit deformation, calculating fractional softening (FS) for each test, using the method that 20% FS is the T_{NR}, discussed in Section 2.4.3, T_{NR}. Table 4.12 shows the T_{NR} for each alloy and the temperature range around 20 % FS.

Table 4.12– T_{NR} Values Interpolated from Collected Double-Hit Deformation Testing with Range of Expected T_{NR} Values

Material ID	T_{NR} (°C)	T_{NR} (°F)	Range (°C)
Lo-V	1005	1841	975-1025
Hi-V	1030	1885	1000-1050
Lo-Nb	961	1763	950-1000
Hi-Nb	1006	1843	975-1025
Lo-Ti	1002	1836	975-1025
Hi-Ti	1024	1876	1000-1050
Lo-Ti-2	1007	1844	1000-1050
Hi-Ti-2	1010	1849	1000-1050
Lo-Ti-Lo-V	1004	1840	1000-1050
Hi-Ti-Lo-V	1015	1860	1000-1050

4.2.3 Microstructure

To verify T_{NR}, the microstructures were examined for each alloy above and below the predicted T_{NR}. Using an aqueous picric solution outlined in Section 3.7.2, the prior austenite grains (PAGs) were revealed and photo micrographs were taken on the light optical microscope (LOM). Figure 4.13 shows representative light micrographs from transverse cross-sections of water quenched and tempered compression samples showing prior austenite grains (PAGs) for the Lo-V alloy at (a) below the expected T_{NR}, compressed at 975 °C and (b) above the expected T_{NR}, compressed at 1025 °C etched with a modified Béchet–Beaujard aqueous picric reagent [3], [11-13]. Figure 4.13a shows some deformed grains, as expected showing complete recrystallization did not occur. Figure 4.13b shows equiaxed grains indicating complete recrystallization occurred. Appendix D shows all light micrographs for the alloys tested below and above T_{NR} and a table of various techniques used to attempt to reveal the PAGs such as variations in quench media, heat treatments, etchants, and time suspended in the etchants.

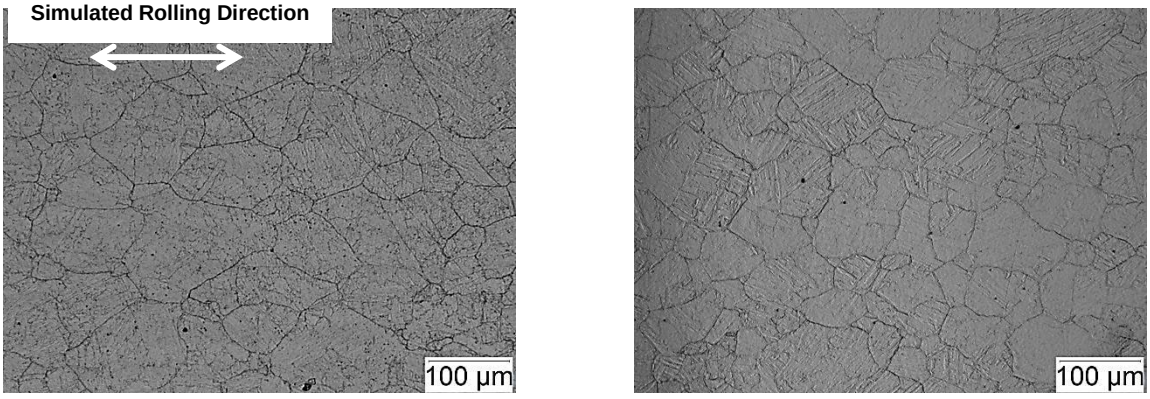

(a) (b)

Figure 4.13 Representative light micrographs from transverse cross-sections of water quenched and tempered compression samples showing prior austenite grains (PAGs) for the Lo-V alloy at (a) below the expected T_{NR}, compressed at 975 °C and (b) above the expected T_{NR}, compressed at 1025 °C C etched with a modified Béchet–Beaujard aqueous picric reagent [3], [11-13]. Figure 4.13a shows some deformed grains, as expected showing complete recrystallization did not occur. Figure 4.13b shows all equiaxed grains indicating complete recrystallization occurred.

CHAPTER 5 : DISCUSSION

This chapter discusses the relationship between microalloy additions and their effects on the non-recrystallization temperature for the steels in this study. A comparison of the T_{NR} results of this study with empirical formulas from the literature is also presented and discussed.

5.1 Synergistic Effect of MA Elements

Figure 5.1 compares the experimental T_{NR} values of the six primary alloys. The experimental T_{NR} is above each bar in °C. The Hi-Nb alloy is the baseline for all of the T_{NR} comparisons because all alloys had Nb levels near 0.060 wt pct, which is the level in the Hi-Nb alloy, with the exception of the Lo-Nb alloy. The V and Ti alloys had further additions of V and Ti, making the Hi-Nb alloy the control.

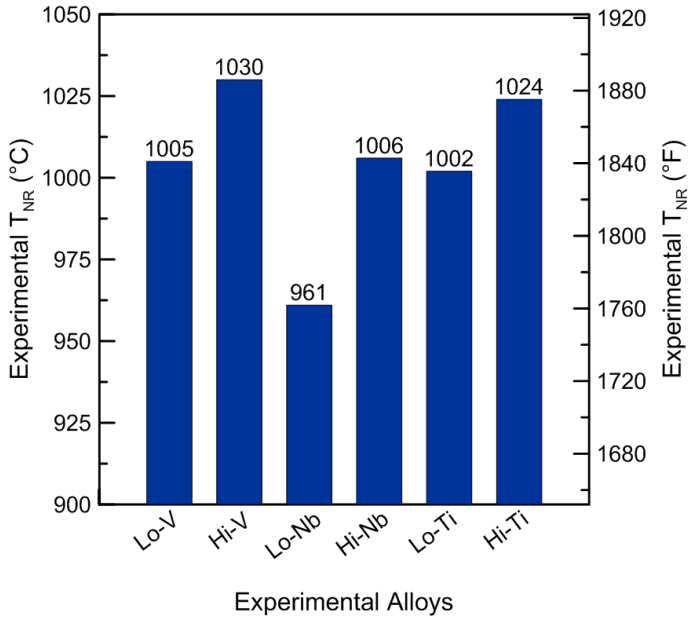

Figure 5.1 Bar graph showing the experimental T_{NR} for the six primary alloys.

Vanadium has been found to form vanadium carbonitrides (V(C,N)) and/or complex niobium-vanadium-carbonitrides ((NbV)(C,N)) at various equilibrium precipitate compositions. Generally, V(C,N) are believed to be N-rich, however in certain conditions, V(C,N) has been found to be C-rich [84]. As N levels increase, temperature increases, or C decreases, V(C,N) become N-rich, as expected. As V levels increase, the V(C,N) precipitates were found to become more C-rich. These findings allude to V forming V(C,N) more readily.

Vanadium is known to interact with Nb-bearing steels and retard recrystallization kinetics [84], [85]. The more complex (NbV)(C,N) appear to drastically inhibit recrystallization in HSLA steels [85]. As V increases, the volume fraction of (Nb,V)(C,N) precipitates also increases, thus inhibiting recrystallization kinetics. These types of complex precipitates can contribute to an increase in T_{NR}.

The current study does not look specifically at the specific types of precipitates formed, but only tries to make suggestions for the observed results based on previous studies from the literature. Future work is intended to provide insight into the mechanisms and composition of believed precipitates affecting T_{NR}.

5.1.1 Comparison of Lo-Nb and Hi-Nb T_{NR}

The Lo-Nb alloy has an experimental T_{NR} of 961 °C (1762 °F), lower than the Hi-Nb alloy having a measured T_{NR} of 1006 °C (1843 °F). Table 5.1 shows the amount of C, Nb, V, Ti, and N for the Lo-Nb and Hi-Nb alloys for reference. Table 5.2 shows the calculated precipitation or dissolution temperature for NbN, NbC, and TiN in °C. Appendix A shows solubility equations and calculations for all alloys. Comparing the alloying additions of the two steels, the only substantial difference is the amount of Nb. The Lo-Nb alloy has 0.027 wt pct Nb, roughly half of the Hi-Nb alloy with 0.060 wt pct Nb. The Lo-Nb alloy is not expected to have any NbN precipitates above 1021 °C (1871 °F) with NbC forming below 985 °C (1805 °F). However, Nb(C,N) are expected to be more stable than NbC, therefore precipitating at higher temperatures. These precipitation temperatures are in contrast to the Hi-Nb alloy with both NbN and NbC forming around the same temperature –1072 °C and 1074 °C (1962 °F and 1965 °F), respectively. TiN precipitates form at roughly the same temperature for both Lo-Nb and Hi-Nb alloys at 1305 °C and 1312 °C (2380 °F and 2393 °F), respectively. The NbN and NbC in the Hi-Nb alloy would be able to pin grain boundaries and inhibit recrystallization at higher temperatures, compared to the Lo-Nb alloy. The TiN are believed to be too coarse to have much pinning effect. Thus, the T_{NR} of the Lo-Nb alloy is lower since pinning precipitates are not expected until lower temperatures. Therefore for a fixed N in the steel, the higher the Nb content, the formation of the precipitates will occur at a higher temperature causing a higher T_{NR}.

Table 5.1– Amounts of C, Nb, V, Ti, and N for the Lo-Nb and Hi-Nb Alloys in wt pct

Element	Lo-Nb	Hi-Nb
C	0.0630	0.0660
Nb	0.0270	0.0600
V	<0.0010	<0.0010
Ti	0.0060	0.0070
N	0.0041	0.0039

Table 5.2– Temperature of Precipitate Formation or Dissolution for the Lo-Nb and Hi-Nb Alloys in °C

Precipitate	Lo-Nb	Hi-Nb
NbN	1021	1072
NbC	985	1074
TiN	1305	1312

5.1.2 Comparison of Lo-V, Hi-V, and Hi-Nb T_{NR}

The Lo-V alloy has an experimental T_{NR} of 1005 °C (1841 °F), the Hi-V alloy has an experimental T_{NR} of 1030 °C (1886 °F), compared to the Hi-Nb alloy with an experimental T_{NR} of 1006 °C (1843 °F). Table 5.3 shows the amount of C, Nb, V, Ti, and N for the Lo-Nb and Hi-Nb alloys for reference. Table 5.4 shows the calculated precipitation temperature for NbN, NbC, and TiN in °C. Comparing the alloying additions of the three steels, the only major difference is the amount of V between the three alloys. There are small titanium variations, as the Hi-Nb alloy has 70 ppm Ti compared to the 50 ppm Ti in the Lo-V and Hi-V alloys. The Hi-Nb alloy has only trace amounts of V, so it is assumed that V does not play any role in affecting T_{NR} in that steel. During cooling the TiN precipitates at high temperatures. The TiN can then coarsen and the coarsened precipitates will no longer be effective in pinning grain boundaries. The remaining free N is still high enough to form NbN, Nb(C,N) or the complex (Nb,V)(C,N) at lower temperatures. The remaining levels of N and the uniform levels of Nb fall in line with the expected temperature range of Nb-rich precipitation formation. For each alloy from a simple Fe-V-C solubility perspective, the V is expected to remain in solution at the experimentally found values of T_{NR}. Since the precipitation is occurring at roughly the same temperatures, some conclusions can be drawn. The Lo-V steel has a similar T_{NR} as the Hi-Nb steel because of the same mechanisms, i.e. formation of Nb-rich precipitates which provide the grain boundary pinning. It can be postulated that V atoms in low concentrations have a weak effect on T_{NR} as exhibited by the Lo-V alloy. However, the T_{NR} of the Hi-V alloy is higher than the Hi-Nb alloy. Holding everything else constant the high amounts of V seem to be playing a role in retarding recrystallization and thus increasing the T_{NR}, which is consistent with previous literature [85]. There are two possibilities as to the role of V in the higher T_{NR} of the Hi-V alloy – precipitates containing vanadium or vanadium in solid solution. Strain-induced precipitation may be an explanation, or precipitation as a mixed NbV(C,N) may be occurring. Solute V atoms may also be inhibiting grain boundary movement thus increasing the T_{NR}. As the atomic radius of V is almost the same as Fe and does not impose much strain on the lattice as a substitutional atom, the postulate that solute V is playing a significant role in increasing T_{NR} seems unlikely. This can be confirmed by the work of Speer and Hansen, 1989 [34], showing small amounts of strain-induced carbonitride precipitates are much more effective in inhibiting recrystallization kinetics than solute atoms at order of magnitude higher amounts.

Table 5.3– Amounts of C, Nb, V, Ti, and N for the Lo-V, Hi-V, and Hi-Nb Alloys in wt pct

Element	Lo-V	Hi-V	Hi-Nb
C	0.0650	0.0680	0.0660
Nb	0.0600	0.0610	0.0600
V	0.0210	0.0560	<0.0010
Ti	0.0050	0.0050	0.0070
N	0.0046	0.0040	0.0039

Table 5.4– Temperature of Precipitate Formation for the Lo-V, Hi-V, and Hi-Nb Alloys in °C

Precipitate	Lo-V	Hi-V	Hi-Nb
VN	836	898	644
VC	662	724	514
NbN	1096	1086	1072
NbC	1072	1079	1074
TiN	1300	1291	1312

5.1.3 Comparison of Lo-Ti, Hi-Ti, and Hi-Nb T_{NR}

The Lo-Ti alloy has an experimental T_{NR} of 1002 °C (1836 °F), the Hi-Ti alloy has an experimental T_{NR} of 1024 °C (1875 °F) and the Hi-Nb alloy with an experimental T_{NR} of 1006 °C (1843 °F). Table 5.5 shows the amount of C, Nb, V, Ti, and N for the Lo-Ti, Hi-Ti, and Hi-Nb alloys for reference. Table 5.6 shows the calculated precipitation temperature for NbN, NbC, and TiN in °C. Comparing the alloying additions of the three steels, the only major difference is the amount of Ti. TiN for all of these three alloys forms at very high temperatures. Therefore, TiN is not expected to meaningfully contribute to inhibiting T_{NR}. However, the amount of free-N and free-Ti after TiN formation influences further precipitate formation. NbN precipitates do not even form in the Lo-Ti and Hi-Ti alloys until below the T_{NR} found for the steels. In contrast, NbC will form and are believed to be the main contributor influencing T_{NR}. The remaining free-N, after TiN formation, for the Lo-Ti alloy is about 8 ppm and 1 ppm for the Hi-Ti alloy, compared with the 30 ppm remaining in the Hi-Nb alloy, calculated at 1000 °C (1832 °F). This limited N clearly explains the low NbN precipitate formation in the Lo-Ti and Hi-Ti alloys. Importantly, the remaining Ti for the two alloys is 136 ppm and 855 ppm, respectively, compared to the 37 ppm Ti remaining in the Hi-Nb alloy after considering TiN formation. Solubility calculations presented in Section 2.3.2 show the Hi-Ti alloy has TiC formation at 1126 °C (2050 °F), followed by NbC precipitation at 1070 °C (1958 °F). It is very likely the combination of TiC and NbC influences the T_{NR}. In the Lo-Ti alloy, TiC and NbN are not expected to form at temperatures above T_{NR}. Therefore, NbC is most likely the biggest inhibitor of grain boundary movement and thus T_{NR} in the Lo-Ti alloy. The Lo-Ti alloy has a T_{NR} very close to the Hi-Nb alloy. NbN and NbC are the most likely inhibitor of T_{NR} in the Hi-Nb alloy. It

appears the amount of NbC in the Lo-Ti alloy pins grain boundaries as much as the combined NbN/NbC precipitation in the Hi-Nb alloy, since all of the C and Nb are available for precipitation at the expected temperature in the Lo-Ti alloy.

Table 5.5– Amounts of C, Nb, V, Ti, and N for the Lo-Ti, Hi-Ti, and Hi-Nb Alloys in wt pct

Element	Lo-Ti	Hi-Ti	Hi-Nb
C	0.0620	0.0650	0.0660
Nb	0.0600	0.0590	0.0600
V	<0.0010	<0.0010	<0.0010
Ti	0.0280	0.0990	0.0070
N	0.0050	0.0040	0.0039

Table 5.6– Temperature of Precipitate Formation for the Lo-Ti, Hi-Ti, and Hi-Nb Alloys in °C

Precipitate	Lo-Ti	Hi-Ti	Hi-Nb
NbN	978	865	1072
NbC	1067	1070	1074
TiN	1433	1521	1312
TiC	929	1126	827

5.2 T_{NR} Empirical Equation Comparison

The T_{NR} values were found through linear interpolation of the double-hit deformation tests. Table 5.7 compares the experimentally-found T_{NR} with the predicted T_{NR} from the literature. It is seen that the Boratto equation does not predict the T_{NR} for the experimental steels very well. The Bai 2011 equation more closely matched the measured T_{NR}, only being slightly high for all alloys, but within at least 30 °C (56 °F). The Fletcher 1 equation consistently predicts a lower T_{NR} than the experimental results, but the spread is similar to the Bai 1 equation, with a maximum difference of 33 ˚C (60 °F). The Bai 1993 equation will not be used as a comparison in this study as the value for β cannot be determined with the parameters examined in this study. The Fletcher 2 equation predicts a T_{NR} much lower than the current experimental results. It should be kept in mind that while models are useful, they usually do not explain the actual physical phenomenon occurring and may be applicable under different conditions.

Figure 5.2 shows the predicted T_{NR} values from the four empirical equations as a function of the experimentally found T_{NR} values. Figure 5.2a shows the comparison between the empirical values of T_{NR} and the experimental values of T_{NR} with the same temperature range for both axis. Figure 5.2b shows the same comparison with a smaller temperature range on the experimental T_{NR} axis. The dotted line on both Figure 5.2a and Figure 5.2b is a 1:1 line representing perfect correlation between the predicted and

experimental values of T_{NR}. The Boratto equation shows a lot of scatter and has an R^2 of 0.64 and a slope of 3.09 for the alloys in this study. The Bai 2011 equation has a better fit, with an R^2 of 0.77 and a slope of 0.97- almost near perfect 1.0. These values indicate that the Bai 2011 equation is a reasonable predictor of T_{NR}. The Fletcher 1 equation has an even better fit with an R^2 of 0.81, with a slope slightly lower than the Bai 2011 equation of 0.94, meaning the Fletcher 1 equation is also a reasonable equation to use to predict T_{NR}. The Fletcher 2 equation shows a lot of scatter in the data, and R^2 of 0.24 and a slope of 0.46. This slope indicates the predicted values of T_{NR} using the Fletcher 2 equation will be much lower than the experimental results. The dotted line shows the 1:1 fit if the predicted values equaled the experimental values.

Table 5.8 shows the range of alloying elements used in this study along with the ranges used in the empirical T_{NR} models from the literature. All values are in wt pct. Dashes in the table are non-reported elements where the value of the element is unknown. For the most part, the experimental steels fall within the ranges used in the literature. More discussion comparing the empirical T_{NR} equations is given in the following sub-sections.

Table 5.7– Comparison of the T_{NR} Predictions from the Empirical Equations from the Literature and the Temperature Range for T_{NR} Based on the Data Collected

Material ID	Experimental T_{NR} (°C)	Boratto[50] Eq (2.4)	Bai 1[28] Eq (2.5)	Fletcher 1 [59] Eq (2.6)	Fletcher 2 [59] Eq (2.8)
Lo-V	1005	1138	1029	999	958
Hi-V	1030	1148	1033	1011	944
Lo-Nb	961	994	965	938	922
Hi-Nb	1006	1156	1029	992	979
Lo-Ti	1002	1175	1022	993	980
Hi-Ti	1024	1233	1024	991	978
Lo-Ti-2	1007	1176	1028	989	977
Hi-Ti-2	1010	1247	1037	986	969
Lo-Ti-Lo-V	1004	1162	1025	996	963
Hi-Ti-Lo-V	1015	1224	1031	995	960

5.2.1 Boratto Equation Comparison

The commonly used Boratto equation [50] is given by,

$$T_{NR} = 887 + 464C + \left(6445Nb - 644\sqrt{Nb}\right) + \left(732V - 230\sqrt{V}\right) + 890Ti + 363Al - 357Si \quad (5.1)$$

where *C, Nb, V, Ti, Al,* and *Si* are the elements in wt pct of the steel. There are issues with using this equation since in some industrial applications it inaccurately predicts T_{NR}. The prediction for the Lo-Nb

steel is the closest prediction of 994 °C (1821 °F), with the experimental T_{NR} of 961 °C (1762 °F). The predicted T_{NR} for all other alloys using the Boratto equation are exceptionally high. These discrepancies are believed to occur due to the lack of accounting for nitrogen in the Boratto equation. Nitrogen is a known precipitate former, and the nitrides respond differently than the dissolved compounds. However, finely dispersed precipitates can pin grain boundaries, thus retarding recrystallization more effectively than solutes alone. In contrast, coarse nitrides are very poor strengtheners. This condition may be most evident analyzing the Hi-Ti alloy, with an experimentally found T_{NR} of 1024 (1875 °F) and a predicted T_{NR} of 1224 °C (2235 °F). It is believed the major factor contributing to a higher T_{NR} is the formation of TiN which pinned grain boundaries. Since not all TiN was dissolved during the reaustenitizing step, some TiN remained prior to cooling and deformation. The TiN precipitates may have coarsened and limited the effect TiN had on pinning grain boundaries, accounting for the discrepancy between the predicted Boratto equation values of T_{NR} and the experimental values of T_{NR}.

Table 5.8– Range of Alloy Content for this Study and the Ranges Used in the Literature for Empirical T_{NR} Calculations

Element	This Study		Boratto Equation		Bai 1 Equation		Fletcher 1 and 2 Equations	
	Min	Max	Min	Max	Min	Max	Min	Max
C	0.062	0.078	0.040	0.170	0.050	0.060	0.050	0.180
Si	0.016	0.022	0.150	0.500	0.250	0.250	0.030	0.500
Mn	1.460	1.480	1.460	1.480	1.550	1.600	0.560	1.860
P	0.011	0.012	-	-	-	-	-	-
S	0.002	0.002	-	-	-	-	-	-
Al	0.027	0.032	0.002	0.065	-	-	0.015	0.050
Nb	0.027	0.061	0.000	0.060	0.075	0.090	0.001	0.043
V	<0.001	0.056	0.000	0.120	-	-	0.001	0.120
Ti	0.005	0.110	0.000	0.110	0.015	0.015	0.001	0.015
N	0.004	0.005	-	-	-	-	0.008	0.019
Mo	0.000	0.000	0.000	0.310	low	high	0.000	0.410
Cr	0.000	0.000	0.000	0.670	-	-	0.000	0.670
Ni	0.000	0.000	0.000	0.450	-	-	0.000	0.390

Another factor to consider is the range of alloying elements that are adequately modeled by the Boratto equation. Table 5.8 shows the composition range used in the Boratto study to establish the correlation between T_{NR} and chemical composition with the composition range used in this study. The composition of the steels used in the current study fall within the range used to determine the Boratto equation except for Si being a magnitude lower and an exception of one Nb grade having 0.061 wt pct Nb

and the Borratto study had a maximum Nb level of 0.060 wt pct. This 100 ppm difference in Nb is not believed to have a significant effect on the comparison of the Boratto equation with the experimental steels. Phosphorous, sulfur and nitrogen may not have been reported in the Boratto report because those elements may have been constant throughout the test, but this is not known for certainty.

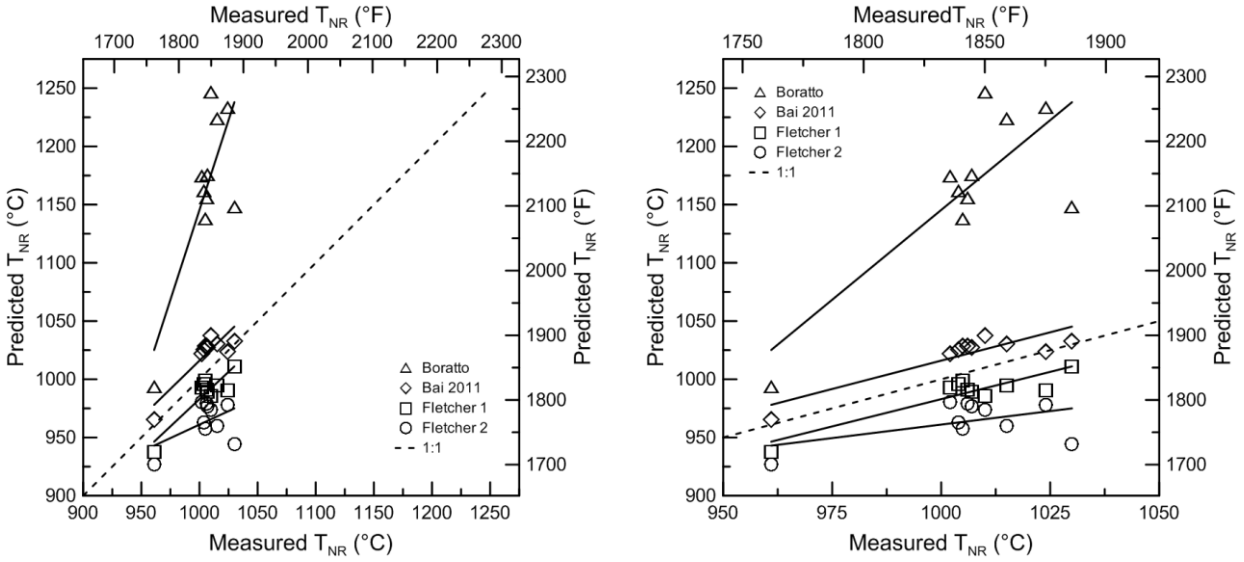

Figure 5.2 Empirical T_{NR} equation predictions plotted against experimentally measured values of T_{NR} for the ten alloys of interest in this study showing (a) the fits with similar scales and (b) the fits with the experimental scale covering a smaller range in temperatures. The dotted line is a 1:1 line showing a perfect fit between the predicted empirical T_{NR} values and the experimental T_{NR} values.

Looking at the equation in a purely mathematical sense, Nb and V both have a square root component subtracted from the equation. Mathematically in order to increase T_{NR}, the steel composition must contain at least 0.01 wt pct Nb and 0.10 wt pct V to overcome the negative effects under in the radical. For all alloys of interest in this study, the Nb content was greater than 0.01 wt pct, nominally 0.06 wt pct for all alloys except the Lo-Nb alloy with 0.027 wt pct. The difference between the experimental result for the Lo-Nb alloy and the Boratto equation is approximately 30 °C (60 °F), having approximately half the Nb of the other steels. The maximum difference between the experimental results and the predicted Boratto result is 237 °C (426 °F). Niobium is known for its strong influence on T_{NR}, and is shown in the equation having an order of magnitude higher coefficient than the other MA elements. It appears this value is slightly exaggerated as the T_{NR} for the alloy with the least Nb was most closely predicted.

The V content for all alloys in this study is lower than the necessary 0.1V wt pct V to overcome the negative effects of the radical. These smaller values for V mean the calculated T_{NR} would be higher due to

the V, not lower. When V is absent, the calculated T_{NR} is higher, as there is no V present to lower the value of T_{NR}. For example, the Lo-Ti was not intended to be produced with V, however some residual V may be present. The T_{NR} calculated for the Lo-Ti alloy without V is equal to 1175 °C (2147 °F), and with a residual V (0.001 wt pct), the calculated T_{NR} is 1168 °C (2135 °F). While this by no means accounts for the entire discrepancy between the Boratto results and the experimental results, it is something that must be kept in mind.

Silicon is also a major contributor to the Boratto equation, with a rather large negative effect. Silicon is known for decreasing the solubility of NbC in austenite [50], which affects the amount of dissolved Nb during the reheat process, thereby leaving NbC precipitates before cooling and deformation. Thus, Nb is not able to form as many finely dispersed precipitates as expected through solubility calculations, resulting in fewer pinned grain boundaries and a lower T_{NR}. The Si levels in the experimental steels are an order of magnitude lower than the Si levels Boratto used, which leads to inconclusive evidence of the effect Si plays on T_{NR}.

It is well known that deformation parameters (i.e. strain, strain rate, interpass time, etc.) effect T_{NR}. The Boratto equation was found using a regression model from multistep hot-torsion data. The testing schedule more accurately models a rolling plate mill than pure double-hit deformation testing by multiple deformation steps at continuously lower temperature. While this experimental difference may affect the coefficients used in the Boratto T_{NR} model, it is not believed to contribute to the drastic differences seen between the model and the experimental data. Overall, the Boratto equation appears to be inadequate for modeling T_{NR}.

5.2.2 Bai 2011 Equation Comparison

The simplified Bai equation [28] derived from solubility calculations is again given by,

$$T_{NR} = 174 \log\left[Nb\left(C + \frac{12}{14}N\right)\right] + 1444 \tag{5.2}$$

where *Nb*, and *C* are the elements in wt pct of the steel and *N* is the free N remaining after TiN precipitation, has a very good correlation to the experimental T_{NR}. While Ti has no direct input into the Bai 2011 equation, the role of Ti as TiN is taken into some account for the final T_{NR} prediction since the remaining N level is used in the equation. The Bai 2011 equation accurately predicts the T_{NR} for the Hi-Ti alloy, and was less than 5 °C higher than the experimental T_{NR} values for the Hi-V and Lo-Nb alloys, while the maximum difference was 27 °C (49 °F) for the Hi-Ti-2 alloy. The minimum difference is negligible, and the maximum difference is within expected limits of a rolling mill. In fact, with the exception of the Hi-T-2 alloy, all values fall within 25 °C (44 °F). It should be noted that the predicted T_{NR} values were all higher, even though they were still close to the experimental values.

In the Bai 1 equation, the nitrogen content is the effective free nitrogen remaining after subtracting nitrogen combined with Ti from the total nitrogen from the experimental steels studied by Bai *et al.*[28]. The Ti was held constant at 0.015 wt pct. The Ti content in this study ranges from 0.005-0.110 wt pct. Interestingly, the alloy with the closest Ti content to Bai *et al.*'s steels, the Lo-Ti alloy with 0.028 wt pct Ti, was not the closest predicted value of T_{NR}. The Hi-Ti, Hi-V, and Lo-Nb alloys were most closely predicted, all within 5 °C (9 °F). The Hi-Ti-2 alloy, having 0.11 wt pct Ti and just over 1 ppm free N (from an original 0.0046 wt pct), had the highest difference between Equation (5.2) and the experimental results, of 27 °C (49 °F).

Overall, the Bai 2011 equation is a fairly good estimator of T_{NR}. Ideally the equation would include V and Ti, along with carbide and nitride formation for the V and Ti. However, since Nb has the strongest influence retarding T_{NR}, the equation is able to accurately predict T_{NR} without including the other MA elements.

5.2.3 Fletcher 1 Equation Comparison

Unlike the Boratto equation and the Bai 2011 equation, the Fletcher 1 equation predicted a consistently lower T_{NR} than the experimental results. The Fletcher 1 equation is given by,

$$T_{NR} = 849 - 349C + 676\sqrt{Nb} + 337V \;\; (R^2 = 0.72) \tag{5.3}$$

where *C*, *Nb*, and, *V* are the elements in wt pct. The predicted T_{NR} values are within 33 °C (60 °F) of the experimental T_{NR} values. These values are similar to the predicted values using the Bai 1 equation. Interestingly, the Hi-Ti prediction was off by the most, but was the most closely predicted T_{NR} value using the Bai 1 equation. The Lo-V alloy was the closest prediction, being only 6 °C lower than the experimental value. The Hi-Ti and Hi-Ti-2 predictions have the highest difference in predicted versus experimental T_{NR} values. The equation shows a lower T_{NR} with the addition of C, but this is known to be untrue, even in a simple C-Mn steel. The next highest difference is with the Lo-Nb alloy, where the Fletcher 1 equation predicts a T_{NR} of 938 °C (1721 °F), a difference of 23 °C (41 °F). The experimental Nb levels are higher than the Nb levels used by Fletcher [59], which may also contribute to the discrepancy. The reported R^2 value is 0.72, meaning there is a positive correlation between Equation (2.6) and the steels studied by Fletcher, but the correlation is not particularly strong.

While the Fletcher 1 equation includes C, Nb, and V, it still lacks Ti and N. Both Ti and N are well known for their role in retarding T_{NR}. Since Ti is known to raise T_{NR}, one could postulate that the predicted T_{NR} values may be closer to the experimental values by including Ti and N. Measurement uncertainties could also be a source of discrepancy. The R^2 value is not very strong, and the C addition subtracts from T_{NR}, showing a decrease in T_{NR}, meaning C actually promotes recrystallization. This equation consistently

predicted a lower T_{NR} than the experimental values, but the difference in T_{NR} values was not extremely significant, all being within 30 °C (54 °F)..

5.2.4 Bai 1993 Equation Comparison

An equation formulated by Bai [9] incorporating both alloy content and strain is given by,

$$T_{NR} = \beta e^{-0.36\varepsilon} \tag{5.4}$$

where β is an alloy-dependent coefficient and ε is strain. The value of the coefficient β was found experimentally for the steels studied by Bai using various pass strains. Since only one pass strain was utilized in the current study, β cannot readily be found. If β is assumed, following the work of Fletcher [59], to be 1100 °C, the predicted T_{NR} would be constant for each alloy. Therefore the Bai 1993 equation will not be used in the current study to determine T_{NR}.

5.2.5 Fletcher 2 Equation Comparison

Fletcher [59] also calculated a T_{NR} equation utilizing strain, given by

$$T_{NR} = 203 - 310C - 149\sqrt{V} + 657\sqrt{Nb} + 683e^{-0.36\varepsilon} \tag{5.5}$$

where *C, V,* and *Nb*, are the elements in wt pct , ε is the pass strain, and β is assumed to be 1100 °C. While Equation (2.8) includes C, V, Nb, and ε, the predicted T_{NR} values for the alloys in this study are not as close as other equations from the literature. The coefficient for C is still negative, and the V term is now under the radical. The ε term is taken from the Bai 1993 equation. The Fletcher 2 equation is consistent in predicting lower T_{NR} values than the experimental values. The closest prediction is the Lo-Ti alloy, calculating a T_{NR} 26 °C (48 °F) lower than the experimentally found value of 1002 °C (1836 °F). The largest difference in T_{NR} values was for the Hi-V alloy, having the Fletcher 2 equation predicting a value 86 °C (154 °F) lower than the experimental 944 °C (1732 °F). Ironically, the Hi-V alloy was found to have the highest T_{NR}, even though the Fletcher 2 equation predicted it would have the lowest value.

5.2.6 T_{NR} Summary

It is clearly apparent that the Boratto equation is not sufficient to predict the T_{NR} values for the alloys in this study. Neither is the Fletcher 2 equation adequate to predict T_{NR}, even though the equation includes multiple MA elements and strain. The Fletcher 1 equation had a better R^2 value than the Bai 2011 equation. The Bai 2011 equation does a reasonably good job of predicting the values for T_{NR} for the steels in the present study.

5.3 Implications of Empirical T_{NR} Equations

The Bai 2011 and Fletcher 1 equation can reasonably predict T_{NR} for the alloys in this study however, both equations are incomplete to explain why one alloy would behave a certain way compared with another. The Bai 2011 equation accurately predicts the T_{NR} for the Hi-Ti, No-Nb, and Hi-V alloys. While the Lo-Nb alloy appears to be an outlier compared with the other alloys, the result is easy to explain. The Lo-Nb alloy only contains 0.027 wt pct Nb, less than half the Nb of the other alloys. The Ti addition is moderate-to low compared with the other alloys. Therefore, a significant amount of N is in solution after TiN formation. With the remaining free N, the solubility equation for NbN does predict some precipitation below 1000 °C (1832 °F), however, close to 0.023 wt pct Nb is predicted to remain in solution. Given the total Nb was only 0.027 wt pct, any grain boundary pinning or inhibiting of the Lo-Nb steel is primarily through Nb solid solution and possibly TiN.

The interesting alloy is the Hi-V, which was not originally expected to have the highest T_{NR}. Again, the Bai 2011 equation accurately predicted the T_{NR} of the Hi-V alloy. At first this prediction may seem confusing since the Bai 2011 equation does not account for V. Looking closer at the composition of the Hi-V alloy is the key. The Hi-V alloy has 0.068 wt pct C, slightly above the average C for the ten alloys. There is relatively high amount of free N after TiN formation for the Hi-V alloy compared with the free N of the other alloys, promoting the formation of Nb(C,N). It is believed the Nb and Nb(C,N) dominate the retardation of T_{NR}. Comparing the Hi-V alloy to the Hi-Nb alloy since their compositions are comparable with the exception of V addition, one might expect the T_{NR} for both alloys to be similar. The Hi-Nb alloy has slightly higher Ti (0.007 vs. 0.005 wt pct) and slightly lower N (0.0039 vs. 0.004 wt pct) than the Hi-V alloy. This difference results in less free N for NbN to form in the Hi-Nb steel as compared to the Hi-V steel. Since the Bai 2011 equation only includes the free N after TiN formation, the predicted T_{NR} values for each alloy, especially the Hi-V, Lo-Nb, and Hi-Ti , are close to the experimental values. Interestingly, the Bai 2011 equation was slightly off on the prediction of the Hi-Nb alloy. Since the Hi-V alloy, with similar alloy content as the Hi-Nb alloy really only differs in V content, a synergistic retardation of T_{NR} must be taking place. The Hi-Nb, without V, has fewer elements to inhibit grain boundary movement.

A limitation to the Bai 2011 equation is the assumption that all possible TiN precipitation occurred. As many solubility calculations exist in the literature, and they do not all agree, one must assess the best equations to utilize for a given situation. This situation leaves discrepancies in the amount of free N available to for Nb(C,N). The Bai 2011 equation is based on a solubility equation presented by Irvine in 1967 for Nb(C,N) precipitation. All solubility equations have limitations through the assumptions of complete precipitation of the free elements. It is possible that the amount of predicted N(C,N) precipitation is not actually forming, thus the inhibiting effects of Nb on T_{NR} are weaker as the Nb is acting as a solid

solution strengthener instead of precipitation pinning of grain boundaries, which may explain the discrepancy between the Bai 2011 equation and experimental results for the Hi-Nb alloy.

Boratto suggested that Si accelerates recrystallization (decreasing the T_{NR}) and postulated that the role of Si was to reduce the solubility of NbC in austenite. With this effect of Si would be seen on reheating, not allowing all the Nb to dissolve and later form fine precipitates. The Lo-Nb and Hi-Ti alloys have the same Si content, and Lo-Nb had the lowest T_{NR}, the amount of N was also the same for both steels. However, the Hi-Ti alloy has twice the Ti of the Lo-Nb steel, pointing to a stronger effect of TiN and Nb in solution rather than the effect of Si. Since the Si in the experimental steels is an order of magnitude lower than the Si use in Boratto's steels, the effect in this study remains indefinite.

CHAPTER 6 : SUMMARY

The purpose of this project was to determine the effect of multiple microalloying elements on the non-recrystallization temperature (T_{NR}) in Nb-bearing plate steel. The T_{NR} is influenced by both alloying elements and deformation parameters. This study focused on the influence of alloying elements only. In particular, the objective was to experimentally determine the T_{NR} for various laboratory-grade steels with systematically varying amounts of V, Nb, and Ti, with C and N held fairly constant. The synergistic effects of these MA elements both through solid solution and precipitation were examined as well as a validation and comparison of empirical T_{NR} formulas from the literature.

Ten Nb-bearing steels were produced in a laboratory at Tata Steel Europe with 0.065 wt pct C, 0.044 wt pct N, and varying amounts of V, Nb, and Ti. Double-hit deformation tests were conducted using the Gleeble® 3500 thermomechanical simulator between the temperatures of 1200 and 750 °C (2192 and 1382 °F). The fractional softening (FS) was found for each double-hit test and plotted as a function of temperature. T_{NR} was determined by finding the temperature at which FS was 20 %, since 20% softening is due to recovery. Light optical micrographs were examined for samples quenched from just above and just below the experimentally determined values of T_{NR}. The T_{NR} values were compared with predicted values using empirical equations from the literature. A summary of important observations and conclusions from this study are listed below.

1. The Bai 2011 equation is a good predictor of T_{NR} for the steels used in this study. While the model does not have a direct input for Ti, the N content is post TiN formation, thus taking Ti into account. The V levels in this study were fairly low. With the strong influence of Nb on T_{NR}, the Nb overpowered most effects to which V may have contributed. The Fletcher 1 equation also predicted reasonable T_{NR} values for the experimental steels, but were consistently low. The Fletcher 1 equation included Nb and V, but did not include N and Ti, which are well known for their influence on T_{NR}. The Boratto equation was a poor predictor of T_{NR} for the ten experimental steels. Some reasons for the discrepancies may be due to the higher levels of Si used by Boratto *et al.*, the extremely high coefficient on the Nb term, and/or the square root term for V.

2. The light optical micrographs just below T_{NR} were not as deformed as previously predicted. It is known in industry that the region between T_{NR} and T_R has somewhat

unpredictable recrystallization behavior- resulting in an almost duplex-like microstructure of partially recrystallized grains and deformed grains. As a rule of thumb, deformation does not take place between the T_{NR} and T_R, which is approximately the region up to 75 °C (135 °F) below T_{NR}. The micrographs examined below T_{NR} were at most 25 °C (45°F) below the T_{NR}, resulting in a high fraction of recrystallized grains. Also, since only one deformation step took place before quenching the samples, the grain size is much larger than is expected from a true rolling schedule at the same temperature. The micrographs were for qualitative analysis only.

3. Strain, strain rate, and interpass time were held constant for each test. It is well known that the deformation parameters affect T_{NR}. This study, however, wanted to focus on the effects of alloying elements only. It is known and understood that the model is not fully applicable to a true rolling schedule as only alloy content was varied.

4. Niobium was found to play a dominating role in the T_{NR}. While it is evident that the V in both V alloys was overpowered by the Nb, some influence of V was seen in the Hi-V alloy with a higher T_{NR} than the Hi-Nb alloy with a similar chemical composition. The magnitude of the V effect is unverifiable due to the limiting number of V alloys and the overpowering effect of Nb. The V is believed to increase T_{NR} through solute drag or other combination of V on Nb(C,N). More V and/or C and N is needed to see the role vanadium-carbo-nitrides have on the T_{NR} in Nb-bearing plate steels.

5. It is evident that precipitation affected the T_{NR}, whether through grain boundary pinning or by limiting free N or C to prevent nitrides or carbides from forming. This effect was evident by comparing the Hi-Nb alloy to the Lo-Ti alloy.

6.1 Microstructure

Compression samples were quenched just above and just below the experimental T_{NR} for microstructural analysis. The light optical micrographs revealed the microstructure just below T_{NR} was not as deformed as previously predicted for each alloy. Figure 6.1 shows light optical micrographs revealing the PAGs for the Hi-V alloy (a) just below T_{NR} deformed at 1000 °C (1832 °F), (b) just above T_{NR} deformed at 1050 °C (1922 °F), and the Lo-Nb alloy (c) just below T_{NR} deformed at 950 °C (1742 °F), and (d) just above T_{NR} deformed at 975 °C (1787 °F). Figure 6.1a and Figure 6.1c show some deformed grains and some recrystallized grains. Figure 6.1b and Figure 6.1d show complete recrystallized grains. Figure 6.1a shows the microstructure approximately 30 °C below the T_{NR}. Figure 6.1b shows the microstructure approximately 20 °C above the recrystallization temperature. In contrast, Figure 6.1c shows the microstructure only 10 °C below the recrystallization temperature and Figure 6.1d shows the microstructure approximately 15 °C above the T_{NR}.

It is known in industry that the region between T_{NR} and T_R has somewhat unpredictable recrystallization behavior- resulting in an almost duplex-like microstructure of partially recrystallized grains and deformed grains. As a rule of thumb, deformation does not take place between the T_{NR} and T_R, which is approximately the region up to 75 °C (135 °F)[2], [28] below T_{NR}. The micrographs examined below T_{NR} were at most 30 °C (54 °F) below the T_{NR}, resulting in a high fraction of recrystallized grains. Therefore, the micrographs are inconclusive in verifying the exact T_{NR}. The FS alone will be used for the T_{NR} values. Also, since only one deformation step took place before quenching the samples, the grain size is much larger than what is expected from a true rolling schedule at the same temperature. The micrographs were for qualitative analysis only.

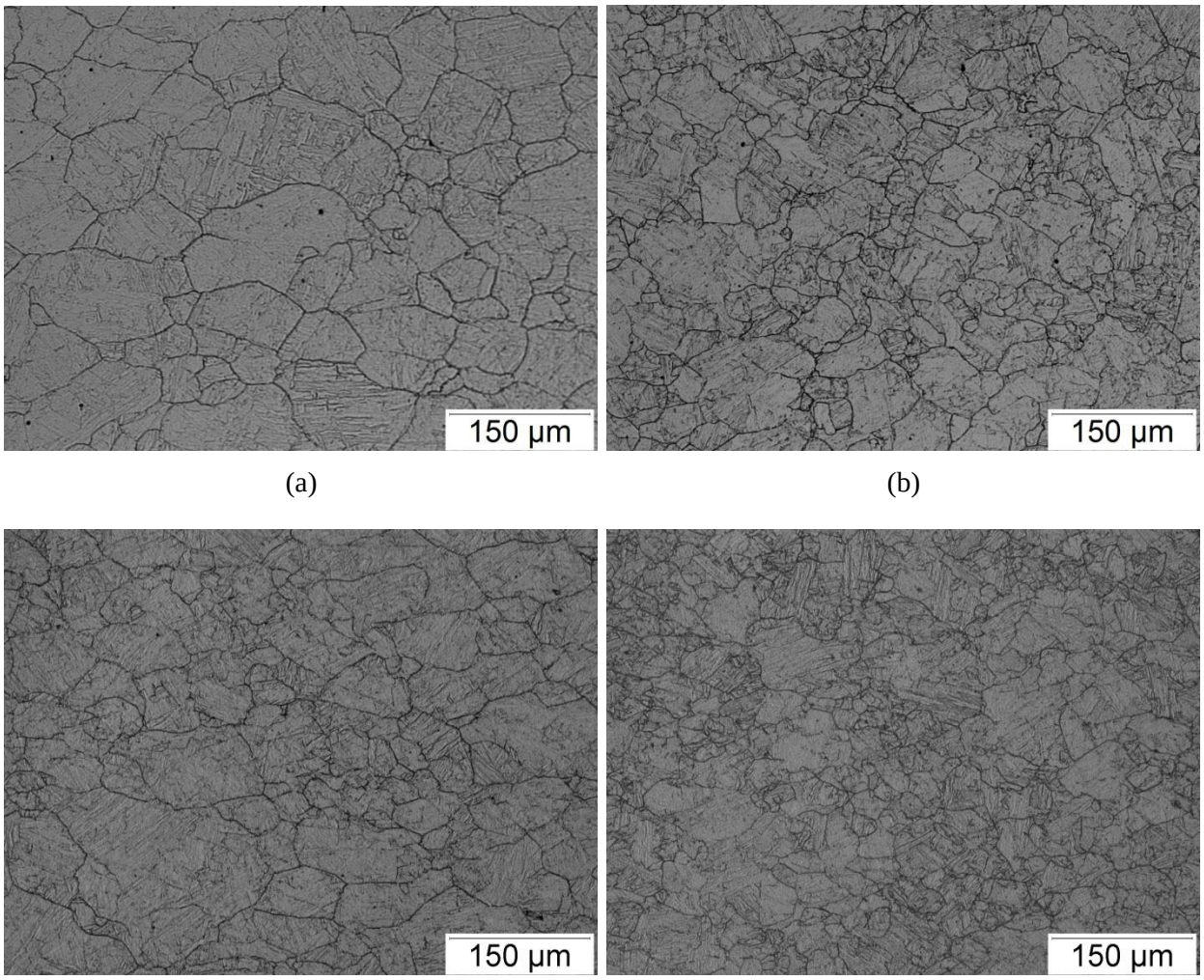

Figure 6.1 Light optical micrographs revealing the prior austenite grains (PAGs) of (a) the Hi-V alloy just below T_{NR} deformed at 1000 °C (1832 °F), (b) the Hi-V alloy just above T_{NR} deformed at 1050 °C (1922 °F), (c) the Lo-V alloy just below T_{NR} deformed at 950 °C (1742 °F),and (d) the Lo-V alloy just above T_{NR} deformed at 975 °C (1787 °F). Both micrographs below T_{NR} show some deformed grains with some recrystallized grains, while both micrographs above T_{NR} show complete recrystallization and possibly even some grain growth. Each sample was etched with a modified Béchet–Beaujard reagent discussed in Section 3.7.2.

CHAPTER 7 : FUTURE WORK

In order to further support the research of this study and provide insight to unanswered questions such relating to the synergistic effects of multiple microalloying elements on the T_{NR} of Nb-bearing plate steels, further testing and analysis is necessary. The follow points are areas of interest.

1. This study focused on qualitative and theoretical analysis to explain results. Understanding precipitation, both on cooling and strain-induced precipitation as well as quantifying the amount and size may lead to better understanding of non-recrystallization temperatures and help develop models to incorporate that information.

2. A thermomechanical simulation of a true plate hot rolling mill would better compare laboratory results with real-world data. A suggested approach is conducting multistep hot torsion testing with varying strain and strain rates. A test using the deformation parameters in this study would also be beneficial to verify the results utilizing another approach. The Bai 1993 equation is suggested as a starting point to model various pass strains.

3. Further testing following the method from this thesis, but with a plain carbon steel as well as a Nb-free MA steel would be beneficial in determining baselines and a control group. This testing would be beneficial because the V was overpowered by the Nb. With a plain carbon steel as a control group and a Nb-free MA steel in the test matrix, more conclusive results for V and possibly even Ti are achievable.

REFERENCES

[1] G. Krauss, *Steels: Processing, Structure, and Performance*. ASM International, 2005, p. 613.

[2] R. L. Bodnar, R. O. Adebanjo, and S. S. Hansen, "Determination of the TR and Ar3 temperatures from roll force measurements," in *37th Mechanical Working and Steel Processing Conference*, 1996, pp. 743–757.

[3] R. Mendoza, J. Huante, V. Camacho, O. Alvarez-Fregoso, and J. a. Juarez-Islas, "Development of an API 5L X-70 grade steel for sour gas resistance pipeline application," *Journal of Materials Engineering and Performance*, vol. 8, pp. 549–555, 1999.

[4] American Petroleum Institute, "Specification for line pipe," American Petroleum Institute, 2009.

[5] T. Gladman, *The Physical Metallurgy of Microalloyed Steels*, 2nd ed. London: Maney Publishing, 2002, p. 363.

[6] W. F. Hosford and R. M. Caddell, *Metal Forming: Mechanics and Metallurgy*, 3rd ed. New York: Cambridge University Press, 2007, p. 312.

[7] S. F. Medina and J. E. Mancilla, "Influence of alloying elements in solution on static recrystallization kinetics of hot deformed steels," *ISIJ international*, vol. 36, pp. 1063–1069, 1996.

[8] W. C. Leslie, *The Physical Metallurgy of Steels*. Marietta, OH: CBLS Publisher & Book Distributor, 1981, p. 396.

[9] D. Q. Bai, S. Yue, W. P. Sun, and J. J. Jonas, "Effect of deformation parameters on the no-recrystallization temperature in Nb-bearing steels," *Metallurgical Transactions A*, vol. 24, pp. 2151–2159, 1993.

[10] S. Vervynckt, K. Verbeken, P. Thibaux, M. Liebeherr, and Y. Houbaert, "Austenite recrystallization–precipitation interaction in niobium microalloyed steels," *ISIJ International*, vol. 49, pp. 911–920, 2009.

[11] S. Vervynckt, K. Verbeken, P. Thibaux, M. Liebeherr, and Y. Houbaert, "Control of the austenite recrystallization in niobium microalloyed steels," *Materials Science Forum*, vol. 638–642, pp. 3567–3572, 2010.

[12] S. Vervynckt, K. Verbeken, B. Lopez, and J. J. Jonas, "Modern HSLA steels and role of non-recrystallisation temperature," *International Materials Reviews*, vol. 57, pp. 187–207, 2012.

[13] G. E. Dieter, *Mechanical Metallurgy*, 3rd ed., vol. 45. McGraw-Hill London, 1986.

[14] E. P. Degarmo, J. T. Black, and R. A. Kohser, *Materials and Processes in Manufacturing*, 9th ed. Hoboken, NJ: John Wiley & Sons, Inc., 2003, p. 1154.

[15] V. B. Ginzburg, *Metallurgical Design of Flat Rolled Steels*. New York: Marcel Dekker, 2004, p. 726.

[16] W. L. Roberts, *Hot Rolling of Steel*, 1st ed. New York: Marcel Dekker, 1983, p. 1033.

[17] F. H. Samuel, S. Yue, J. J. Jonas, and K. R. Barnes, "Effect of dynamic recrystallization on microstructural evolution during strip rolling," *ISIJ International*, vol. 30, pp. 216–225, 1990.

[18] L. N. Pussegoda and J. J. Jonas, "Comparison of dynamic recrystallization and conventional controlled rolling schedules by laboratory simulation," *ISIJ International*, vol. 31, pp. 278–288, 1991.

[19] P. A. Manohar, T. Chandraand, and C. Killmore, "Continuous cooling transformation behaviour of microalloyed steels contaiting Ti, Nb, Mn, and Mo," *ISIJ International*, vol. 36, pp. 1486–1493, 1996.

[20] R. D. Doherty, D. A. Hughes, F. J. Humphreys, J. J. Jonas, D. Juul Jensen, M. E. Kassner, W. E. King, T. R. McNelley, H. J. McQueen, and A. D. Rollett, "Current issues in recrystallization: A review," *Materials Science and Engineering A*, vol. 238, pp. 219–274, 1997.

[21] A. J. DeArdo, "Niobium in modern steels," *International Materials Reviews*, vol. 48, pp. 371–402, 2003.

[22] S. S. Gorelik, *Recrystallization in Metals and Alloys*, 2nd ed. Moscow: MIR Publishers, 1981, p. 479.

[23] F. J. Humphreys and M. Hatherly, *Recrystallization and Related Annealing Phenomena*, 2nd ed. Elsevier Science & Technology Books, 2004, p. 658.

[24] L. Lan, C. Qiu, D. Zhao, X. Gao, and L. Du, "Dynamic and static recrystallization behavior of low carbon high niobium microalloyed steel," *Journal of Iron and Steel Research, International*, vol. 18, pp. 55–60, 2011.

[25] R. Abbaschian, L. Abbaschian, and R. E. Reed-Hill, *Physical Metallurgy Principles*, 4th ed. Stamford, CT: Cengage Learning, 2009, p. 750.

[26] B. F. Decker and D. Harker, "Recrystallization in rolled copper," *Journal of Metals*, vol. 188, pp. 887–890, 1950.

[27] E. Poliak, "Recrystallization during hot rolling," in *Austenite Processing Symposium (Internal company presentation)*, 2008, p. 47.

[28] D. Q. Bai, R. L. Bodnar, J. Ward, J. Dorricott, and S. Sanders, "Development of discrete X80 line pipe plate at SSAB Americas," in *International Symposium on the Recent Developments in Plate Steels*, 2011, pp. 13–22.

[29] S. Jansto, "Niobium-bearing structural steels for the 21st centruy," in *Niobium Bearing Structural Steels*, 2010, pp. 1–27.

[30] E. T. Turkdogan, "Causes and effects of nitride and carbonitride precipitation during continuous casting," *Iron and Steelmaker*, vol. 16, no. 5, pp. 61–75, 1987.

[31] P. R. Rios, “Expression for solubility product of niobium carbonitride in austenite,” *Materials Science and Technology*, vol. 4, pp. 324–327, 1988.

[32] A. J. DeArdo, M. J. Hua, K. G. Cho, and C. I. Garcia, “On strength of microalloyed steels: An interpretive review,” *Materials Science and Technology*, vol. 25, pp. 1074–1082, Sep. 2009.

[33] J. G. Speer, J. R. Michael, and S. S. Hansen, “Carbonitride precipitation in niobium / vanadium microalloyed steels,” *Metallurgical Transactions A*, vol. 18, pp. 211–222, 1986.

[34] J. G. Speer and S. S. Hansen, “Austenite recrystallization and carbonitride precipitation in niobium microalloyed steels,” *Metallurgical Transactions A*, vol. 20, pp. 25–38, 1989.

[35] H. L. Andrade, M. G. Akben, and J. J. Jonas, “Effect of molybdenum, niobium, and vanadium on static recovery and recrystallization and on solute strengthening in microalloyed steels,” *Metallurgical Transactions A*, vol. 14, pp. 1967–1977, 1983.

[36] L. J. Cuddy and J. C. Raley, “Austenite grain coarsening in microalloyed steels,” *Metallurgical Transactions A*, vol. 14, pp. 1989–1995, 1983.

[37] S. Zajac, T. Siwecki, B. Hutchinson, and M. Attlegård, “Recrystallization controlled rolling and accelerated cooling for high strength and toughness in V-Ti-N steels,” *Metallurgical Transactions A*, vol. 22, pp. 2681–2694, 1991.

[38] L. Jiang, A. O. Humphreys, and J. J. Jonas, “Effect of silicon on the interaction between recrystallization and precipitation in niobium microalloyed steels,” *ISIJ International*, vol. 44, pp. 381–387, 2004.

[39] S. H. Mousavi Anijdan and S. Yue, “The necessity of dynamic precipitation for the occurrence of no-recrystallization temperature in Nb-microalloyed steel,” *Materials Science and Engineering: A*, vol. 528, pp. 803–807, 2011.

[40] S. S. Hansen, J. B. Vander Sande, and M. Cohen, “Niobium carbonitride precipitation and austenite recrystallization in hot-rolled microalloyed steels,” *Metallurgical Transactions A*, vol. 11, pp. 387–402, 1980.

[41] B. Dutta and C. M. Sellars, “Effect of composition and process variables on Nb (C , N) precipitation in niobium microalloyed austenite,” *Materials Science and Technology*, vol. 3, pp. 197–206, 1987.

[42] S.-J. Lee and Y.-K. Lee, “Prediction of austenite grain growth during austenitization of low alloy steels,” *Materials & Design*, vol. 29, pp. 1840–1844, Oct. 2008.

[43] K. Lücke and K. Detert, “A quantitative theory of grain-boundary motion and recrystallization in metals in the presence of impurities,” *Acta Metallurgica*, vol. 5, pp. 328–637, 1957.

[44] D. R. Lide, “Molecular Structure and Spectroscopy,” in *Handbook of Chemistry and Physics*, 90th ed., 2009, pp. 1–117.

[45] L. J. Cuddy, “The effect of microalloy concentration on the recrystallization of austenite during hot deformation,” in *Thermomechanical Processing of Microalloyed Austenite1*, 1982, pp. 129–140.

[46] R. Lagneborg, T. Siwecki, S. Zajac, and B. Hutchinson, “The role of vanadium in microalloyed steels,” *The Scandanavian Journal of Metalurgy*, 1999.

[47] A. J. DeArdo, M. Hua, and C. I. Garcia, “Basic metallurgy of modern niobium steels,” in *International Symposium on Niobium Microalloyed Sheet Steel for Automotive Application*, 2006, pp. 499–549.

[48] H. Adrian and F. B. Pickering, “Effect of titanium aditions on austenite grain growth kinetics of medium carbon V-Nb steels containing 0.008-0.018 % N,” *Material Science and Technology*, vol. 7, pp. 176–182, 1991.

[49] L. Zheng and S. Gao, “Production and application of high strength and high toughness pipeline steel with acicular ferrite,” 2005.

[50] R. Barbosa, F. Boratto, S. Yue, and J. J. Jonas, “The influence of chemical composition on the recrystallisation behaviour of microalloyed steels,” in *Processing, Microstructure and Properties of HSLA Steels*, 1988, pp. 51–61.

[51] P. K. Ray, R. I. Ganguly, and A. K. Panda, “Determination of recrystallization stop temperature (TR) of an HSLA steel,” *Steel Grips: Journal of Steel and Related Materials*, 2004.

[52] T. M. Maccagno, J. J. Jonas, S. Yue, B. J. McCrady, R. Slobodian, and D. Deeks, “Determination of recyrstallization stop temperature from rolling mill logs and comparison with laboratory simulation results,” *ISIJ international*, vol. 34, pp. 917–922, 1994.

[53] A. B. Le Bon and L. N. de Saint-Martin, “Using laboratory simulations to improve rolling schedules and equipment,” in *Micro Alloying 75*, 1975, pp. 90–98.

[54] P. J. Wray, “Onset of recrystallization during the tensile deformation of austenitic iron at intermediate strain rates,” *Metallurgical Transactions A*, vol. 6, pp. 1197–1203, 1975.

[55] S. F. Medina, A. Quispe, P. Valles, and J. L. Banos, “Recrystallization-precipitation interaction study of two medium carbon niobium microalloyed steels,” *ISIJ international*, vol. 39, pp. 913–922, 1999.

[56] Y. B. Xu, Y. M. Yu, B. L. Xiao, Z. Y. Liu, and G. D. Wang, “Modelling of microstructure evolution during hot rolling of a high-Nb HSLA steel,” *Journal of Materials Science*, vol. 45, pp. 2580–2590, 2010.

[57] E. J. Palmiere, C. I. Garcia, and A. J. DeArdo, “The influence of niobium supersaturation in austenite on the static recrystallization behavior of low carbon microalloyed steels,” *Metallurgical and Materials Transactions A*, vol. 27A, pp. 951–960, 1996.

[58] A. I. Zaky, “Determinations of the non-recrystallization temperature for X52 steel produced by compact slab process combined with direct hot rolling,” *Journal of Materials Engineering and Performance*, vol. 15, pp. 651–655, 2006.

[59] F. Fletcher, “Meta-analysis of Tnr measurements: Determining new empirical models based on composition and strain,” in *Austenite Processing Symposium (Internal company presentation)*, 2008, pp. 1–14.

[60] O. Kwon and A. J. DeArdo, “Interactions between recrystallization and precipitation in hot-deformed microalloyed steels,” *Acta Metallurgica et Materialia*, vol. 39, pp. 529–538, 1991.

[61] G. A. Wilber, J. R. Bell, J. H. Bucher, and W. J. Childs, “The determination of rapid recrystallization rates of austenite and the temperatures of hot deformation,” *Transactions Of The Metallurgical Society Of AIME*, vol. 242, pp. 2305–2308, 1968.

[62] J. N. Cordea, “Effect of composition and processing on strength and toughness of Nb and V treated high strength low allow plate,” in *Symposium jointly organized by The METALLURG COMPANIES*, 1970, pp. 61–80.

[63] C. Devadas, I. V. Samarasekera, and E. B. Hawbolt, “The thermal and metallurgical state of steel strip during hot rolling : Part III. Microstructural evolution,” *Metallurgical Transactions*, vol. 22, pp. 335–349, 1991.

[64] S. Vervynckt, “Control of the non-recrystallization temperature in high strength low alloy (HSLA) steels,” Universiteit Gent, 2010.

[65] S. Vervynckt, “Control of the non-recrystallisation temperature in high strength low alloy (HSLA) steels: Recrystallisation-precipitation interaction in model Nb-steels,” in *Austenite Processing Symposium (Internal company presentation)*, 2008, p. 29.

[66] K. P. Rao, Y. K. D. V. Prasad, and E. B. Hawbolt, “Study of fractional softening in multi-stage hot deformation,” *Journal of Materials Processing Technology*, vol. 77, pp. 166–174, 1998.

[67] H. J. McQueen, “Review of simulations of multistage hot-forming of steels,” *Canadian Metallurgical Quarterly*, vol. 21, pp. 445–460, 1982.

[68] H. J. Mcqueen and J. J. Jonas, “Role of the dynamic and static softening mechanisms in multistage hot working,” *J. Applied Metalworking*, vol. 3, pp. 410–420, 1985.

[69] A. Laasraoui and J. J. Jonas, “Prediction of steel flow stresses at high temperatures and strain rates,” *Metallurgical Transactions A*, vol. 22, pp. 1545–1558, 1991.

[70] A. Najafi-Zadeh, S. Yue, and J. J. Jonas, “Influence of hot strip rolling parameters on austenite recrystallization in interstitial free steels,” *ISIJ International*, vol. 32, pp. 213–221, 1992.

[71] M. Olasolo, P. Uranga, J. M. Rodriguez-Ibabe, and B. López, “Effect of coiling temperature on microstructure and mechanical properties of a Nb-V microalloyed steel,” *Materials Science Forum*, vol. 638–642, pp. 3350–3355, 2010.

[72] M. Vega, S. F. Medina, A. Quispe, M. Gomez, and P. P. Gomez, “Recrystallisation driving forces against pinning forces in hot rolling of Ti-microalloyed steels,” *Materials Science and Engineering: A*, vol. 423, pp. 253–261, 2006.

[73] E. J. Pavlina, “Complex precipitate formation in austenite in low-carbon steels containing titanium, niobium, and molybdenum,” Colorado School of Mines, 2010.

[74] B. Roebuck, J. D. Lord, and M. Brooks, “Measuring flow stress in hot axisymmetric compression tests,” Teddington, Middlesex, United Kingdon, TW 11 0LW, 2002.

[75] Dynamic Systems Inc, “Gleeble® systems application note: Axisymmetric uniaxial compression testing using ISO-TTM anvils on Gleeble systems,” Poestenkill, New York, 2003.

[76] DuPont, “Teflon specification bulletin: High performance films DuPont PFA flurocarbon film types LP and CLP,” DuPont Company, 1996.

[77] Dynamic Systems Inc, “Gleeble® systems application note: Diffusion effects on type K (Cr-Al) thermocouple measurements,” DSI: Dynamic Systems Inc., Poestenkill, New York, 2001.

[78] L. M. Rothleutner, “Influence of reheat temperature and holding time on the interaction of V, Al, and N in air-cooled forging steels,” Advanced Steel Processing and Products Research Center, 2012.

[79] D. R. Barraclough, “Etching of prior austenite grain boundaries in martensite,” *Metallography*, vol. 6, pp. 465–472, Dec. 1973.

[80] R. L. Bodnar, V. E. McGraw, and A. V. Brandemarte, “Technique for revealing prior austenite grain boundaries in CrMoV turbine rotor steel,” *Metallography*, vol. 114, pp. 109–114, 1984.

[81] L. Zhang and D. C. Guo, “A general etchant for revealing prior-austenite grain boundaries in steels,” *Materials Characterization*, vol. 30, pp. 299–305, 1993.

[82] R. L. Bodnar, “private communication.” 2012.

[83] W. Roberts and B. Ahlblom, “A nucleation criterion for dynamic recrystallization during hot working,” *Acta Metallurgica*, vol. 26, pp. 801–913, 1978.

[84] J. G. Speer, S. Mehta, and S. S. Hansen, “Composition of vanadium carbonitride precipitates in microalloyed austenite,” *Scripta Metallurgica*, vol. 18, pp. 1241–1244, 1984.

[85] J. R. Michael, J. G. Speer, and S. S. Hansen, “Communications austenite recrystallization in Nb / V microalloyed steels,” *Metallurgical Transactions A*, vol. 18A, pp. 481–483, 1987.

APPENDIX A: SOLUBILITY CALCULATIONS

Solubility calculations were carried out using the equations by Turkdogan [30], presented in Section 2.3.2. Table A.1 shows the temperature for calculated precipitation formation of TiN, NbN, VN, AlN, TiC, NbC, and VC for the steels in this study. Figure A.1 – Figure A.3 show solubility plots for the precipitates of interest. The isothermal lines show the relative temperatures for precipitate formation.

Table A.1 – Solubility Temperatures for the Precipitates of Interest

	TiN (°C)	NbN (°C)	VN (°C)	AlN (°C)	TiC (°C)	NbC (°C)	VC (°C)
Lo-V	1300	1096	836	1093	804	1072	662
Hi-V	1291	1086	898	1073	817	1079	724
Lo-Nb	1305	1021	650	1071	815	985	513
Hi-Nb	1312	1072	644	1050	827	1074	514
Lo-Ti	1433	978	586	930	929	1067	512
Hi-Ti	1521	865	516	776	1126	1070	514
Lo-Ti-2	1444	962	577	907	958	1075	515
Hi-Ti-2	1543	860	512	762	1161	1091	969
Lo-Ti-Lo-V	1435	962	691	905	956	1072	630
Hi-Ti-Lo-V	1524	866	621	776	1136	1080	642

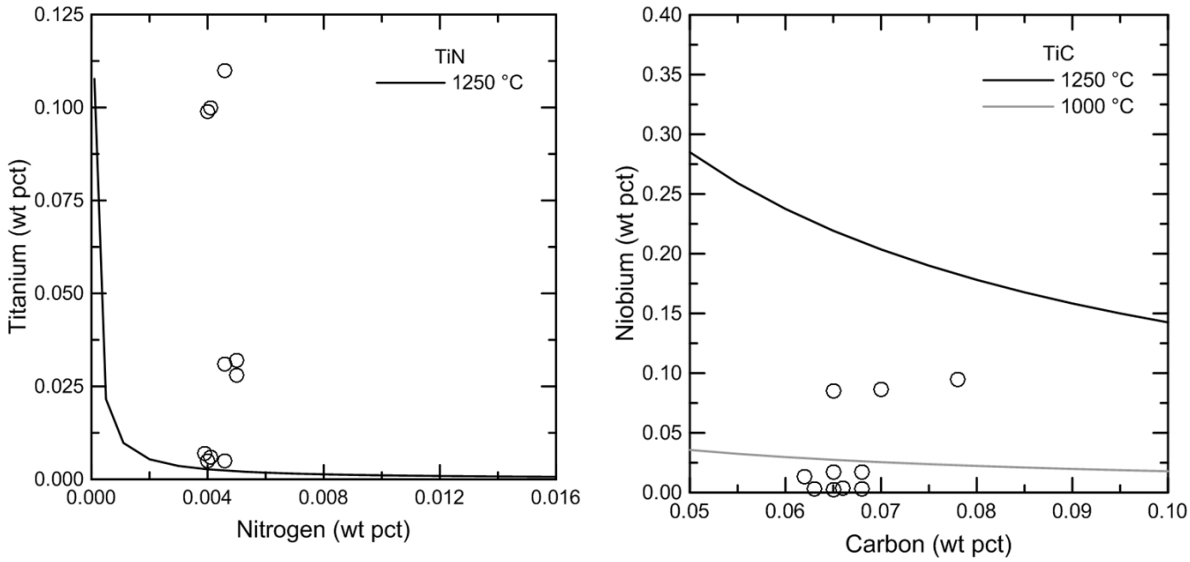

(a) (b)

Figure A.1 Solubility plots showing (a) TiN and (b) TiC for the ten alloys in this study. Isothermal lines show relative temperatures for precipitate formation.

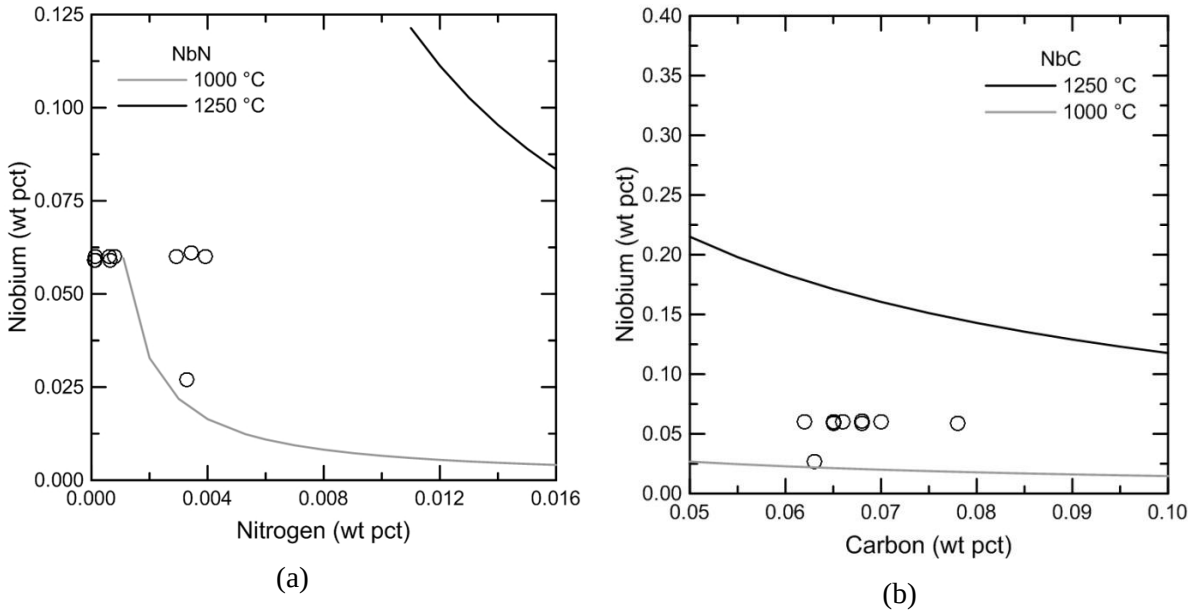

(a) (b)

Figure A.2 Solubility plots showing (a) NbN and (b) NC for the ten alloys in this study. Isothermal lines show relative temperatures for precipitate formation.

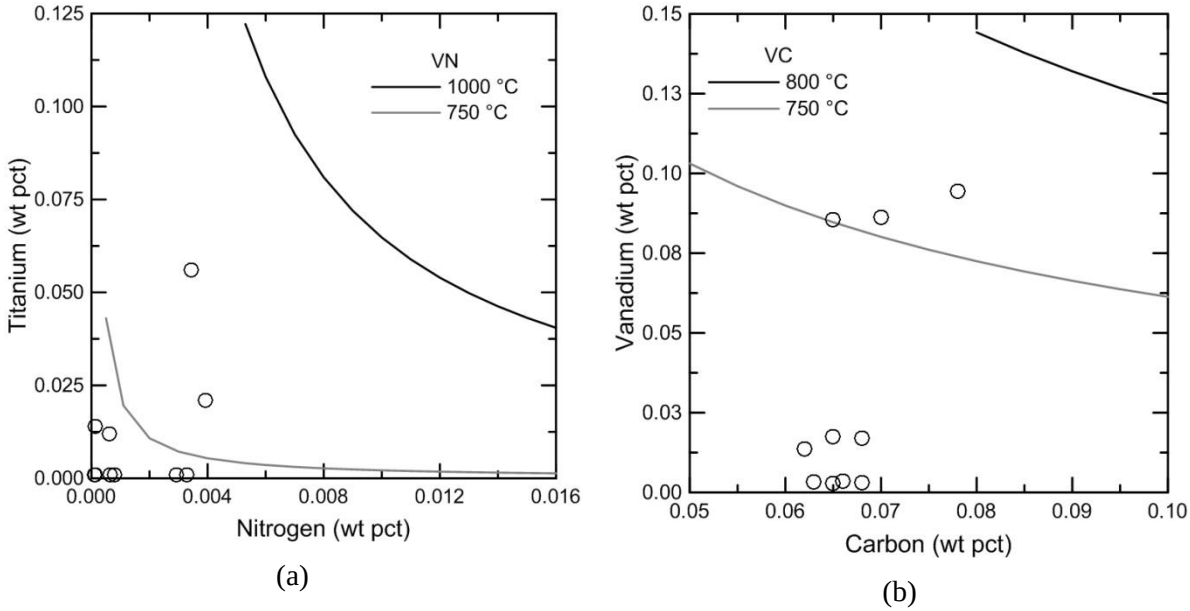

(a) (b)

Figure A.3 Solubility plots showing (a) NbN and (b) NC for the ten alloys in this study. Isothermal lines show relative temperatures for precipitate formation.

APPENDIX B: AS RECEIVED MATERIAL CHARACTERIZATION

This appendix provides additional data regarding the as received material used in this study. This includes photos of the as-received hot rolled plates, initial micrographs, and chemical analysis results.

B.1 As Received Hot Rolled Plate

Experimental alloys were produced and hot rolled byTata Steel Europe. Each 60 kg (132 lb) melt produced two 30 kg (66 lb) ingots with a high and low addition of a chosen alloying element. The ingots were then hot rolled with no particular parameters for load to a chosen thickness of approximately 30 mm (1.18 in). Ten alloys were produced with the following identification: Lo-V, Hi-V, Lo-Nb, Hi-Nb, Lo-Ti, Hi-Ti, Lo-T-2, Hi-Ti-2, Lo-Ti-Lo-V, and Hi-Ti-Lo-V. Figure B.1 through Figure B.10 show the (a) top view and length, (b) width, and (c) thickness of each plate. A single letter designation was used for easy machining identification A-J. The yellow code is the Tata Steel Europe identification. The grid markings designate the desired location of torsion specimens.

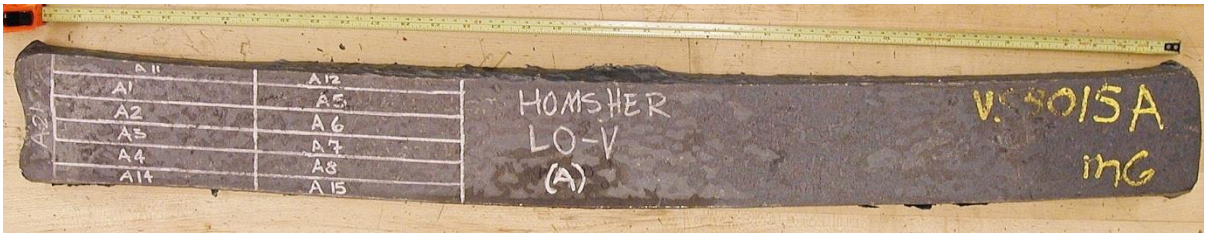

(a)

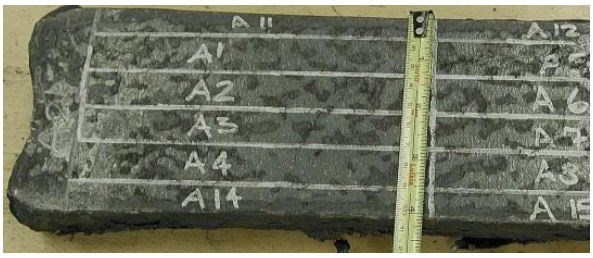

(b)

(c)

Figure B.1 Photos of the as received hot rolled Lo-V alloy showing the (a)top view and total length, (b) width, and (c) thickness of the plate

(a)

(b)

(c)

Figure B.2 Photos of the as received hot rolled Hi-V alloy showing the (a)top view and total length, (b) width, and (c) thickness of the plate

(a)

(b)

(c)

Figure B.3 Photos of the as received hot rolled Lo-Nb alloy showing the (a)top view and total length, (b) width, and (c) thickness of the plate

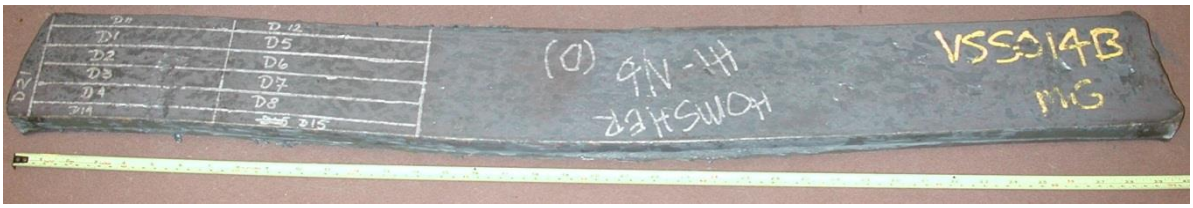

(a)

(b)

(c)

Figure B.4 Photos of the as received hot rolled Hi-Nb alloy showing the (a)top view and total length, (b) width, and (c) thickness of the plate

(a)

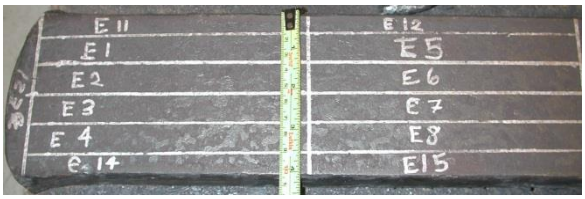

(b)

(c)

Figure B.5 Photos of the as received hot rolled Lo-Ti alloy showing the (a)top view and total length, (b) width, and (c) thickness of the plate

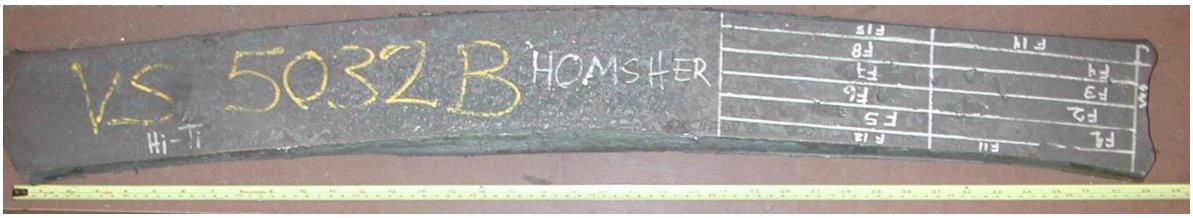

(a)

(b)

(c)

Figure B.6 Photos of the as received hot rolled Hi-Ti alloy showing the (a)top view and total length, (b) width, and (c) thickness of the plate

(a)

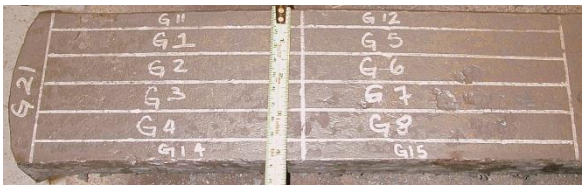

(b)

(c)

Figure B.7 Photos of the as received hot rolled Lo-Ti-2 alloy showing the (a)top view and total length, (b) width, and (c) thickness of the plate

(a)

(b)

(c)

Figure B.8 Photos of the as received hot rolled Hi-Ti-2 alloy showing the (a)top view and total length, (b) width, and (c) thickness of the plate

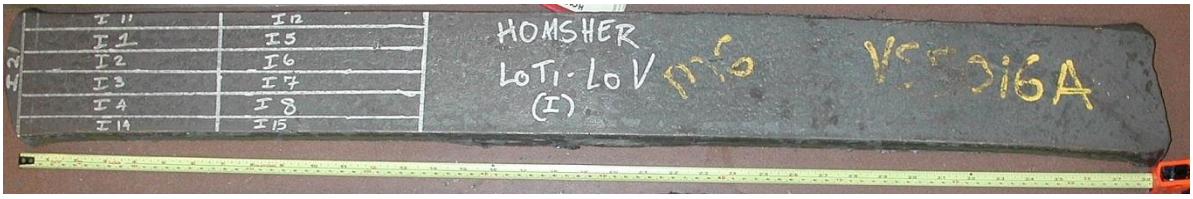

(a)

(b)

(c)

Figure B.9 Photos of the as received hot rolled Lo-Ti-Lo-V alloy showing the (a)top view and total length, (b) width, and (c) thickness of the plate

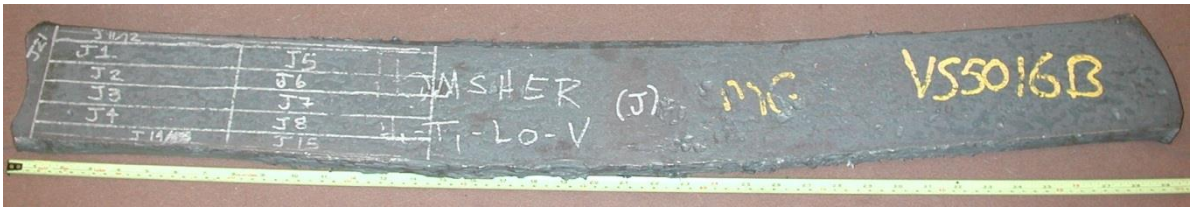

(a)

(b)

(c)

Figure B.10 Photos of the as received hot rolled Hi-T-Lo-V alloy showing the (a)top view and total length, (b) width, and (c) thickness of the plate

B.2 As Received Micrographs

Metallographic samples of the ten alloys in the as-received condition were used to obtain approximate grain sizes and general microstructural constituent identification. The expected microstructure for each alloy was primarily ferrite with possible pearlite or bainite colonies from the air-cooled hot-rolled condition. Figure B.11-Figure B.15 show representative light micrographs for the as-received alloys from the center of the plate width etched in a 2 % nital solution for 3-5 s. As expected, the microstructure is mostly ferrite with some pearlite or bainite colonies.

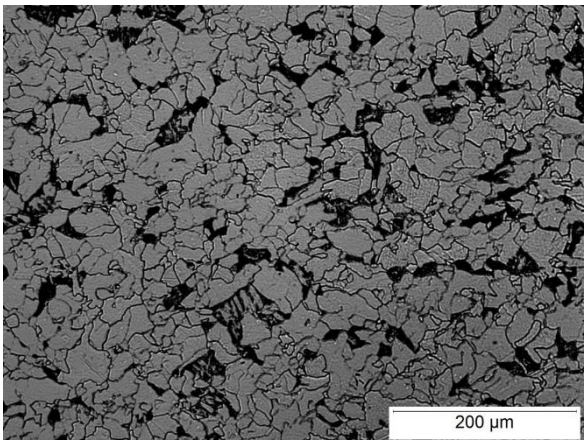

(a)

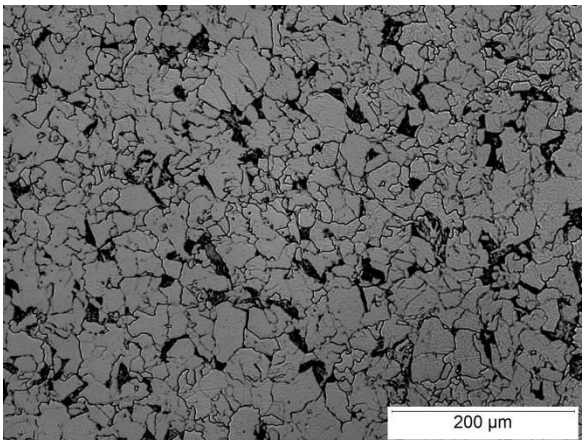

(b)

Figure B.11 Representative light micrographs for the as-received (a) Lo-V and (b) Hi-V alloys from the center of the plate width etched in a 2 % nital solution for 3-5 s.

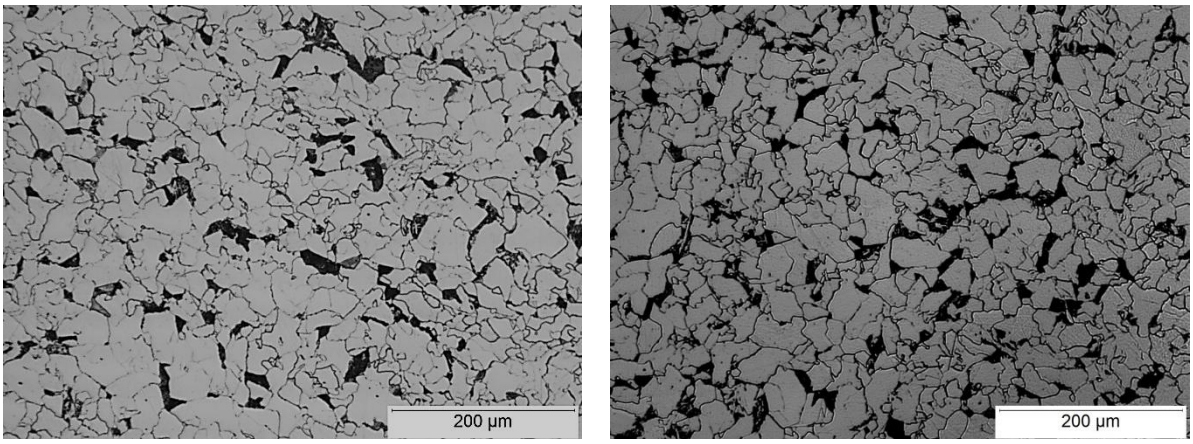

(a) (b)

Figure B.12 Representative light micrographs for the as-received (a) Lo-Nb and (b) Hi-Nb alloys from the center of the plate width etched in a 2 % nital solution for 3-5 s.

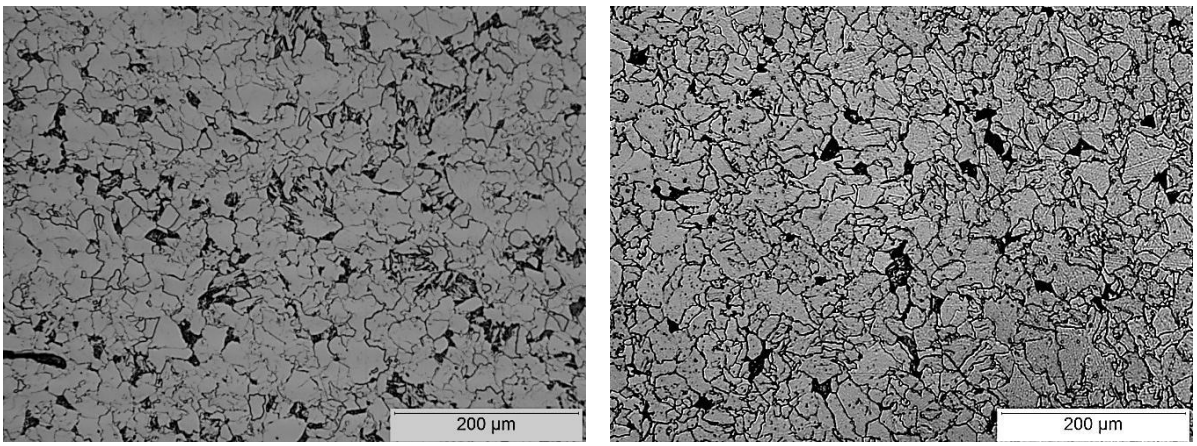

(a) (b)

Figure B.13 Representative light micrographs for the as-received (a) Lo-Ti and (b) Hi-Ti alloys from the center of the plate width etched in a 2 % nital solution for 3-5 s.

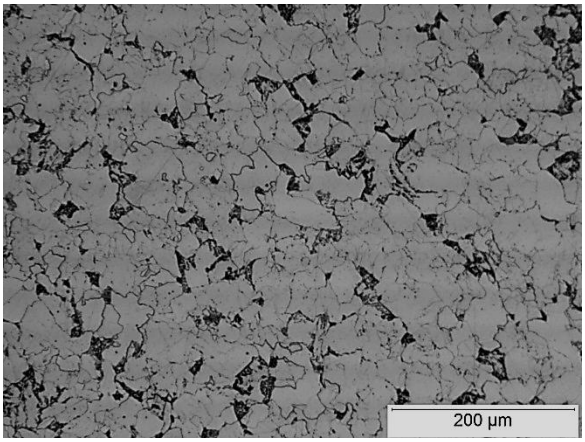

(g)

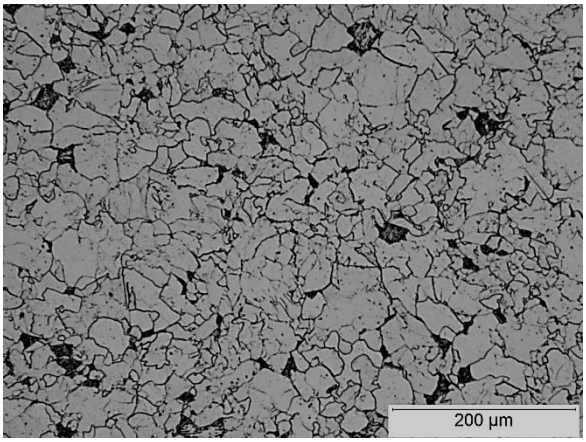

(h)

Figure B.14 Representative light micrographs for the as-received (a) Lo-Ti-2 and (b) Hi- Ti-2 alloys from the center of the plate width etched in a 2 % nital solution for 3-5 s.

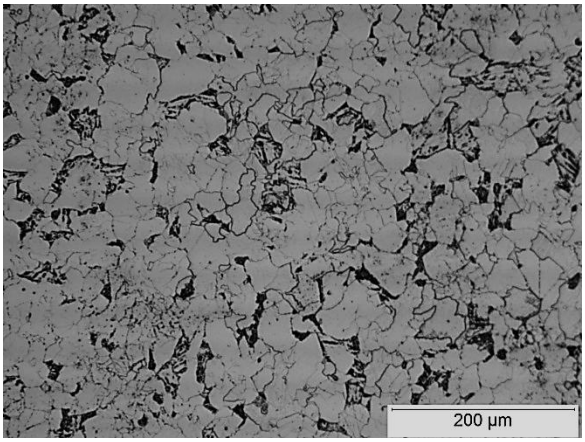

(i)

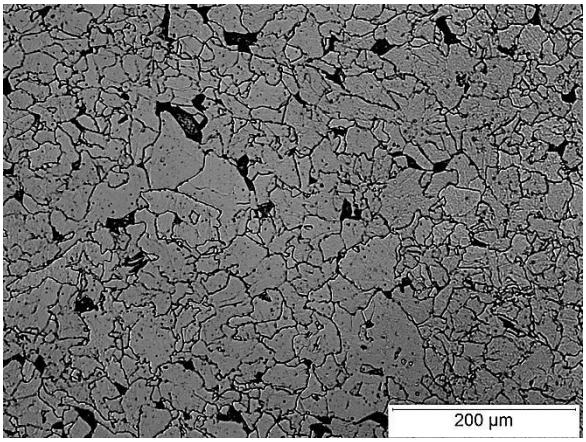

(j)

Figure B.15 Representative light micrographs for the as-received (a) Lo-Ti-Lo-V and (b) Hi-Ti-Lo-V alloys from the center of the plate width etched in a 2 % nital solution for 3-5 s.

B.3 As Received Chemical Analysis

Two sections from each plate were sent to SSAB Americas for chemical analysis. Standard Leco combustion analysis tested the amount of C, S, and N in the steel. Optical emission spectroscopy (OES) was used to confirm the remaining elements. Table B.1 shows the original chemical analysis provided by Tata Steel Europe. Table B.2 shows the results provided by SSAB Americas. The results from the Leco analysis confirmed the composition for C, S, and N provided by Tata Steel Europe. The remaining elements had good agreement for all alloys and all elements, with the exception of the V

content. The OES analysis from SSAB for V content was consistently higher by 20-30 ppm wt pct for each alloy. This result may be due to a calibration discrepancy or the location of specimen in the plate.

Table B.1 – Laboratory Nb-Bearing Microalloyed Steels in wt pct

Material ID	C	Mn	Si	Ti	Nb	V	Al	N	S	P
Lo-V	0.065	1.46	0.016	0.005	0.060	0.021	0.030	0.0046	0.0017	0.012
Hi-V	0.068	1.46	0.017	0.005	0.061	0.056	0.029	0.0040	0.0017	0.012
Lo-Nb	0.063	1.47	0.019	0.006	0.027	<0.001	0.030	0.0041	0.0017	0.012
Hi-Nb	0.066	1.46	0.020	0.007	0.060	<0.001	0.028	0.0039	0.0017	0.011
Lo-Ti	0.062	1.48	0.018	0.028	0.060	<0.001	0.032	0.0050	0.0018	0.011
Hi-Ti	0.065	1.48	0.019	0.099	0.059	<0.001	0.030	0.0040	0.0019	0.011
Lo-Ti-2	0.068	1.47	0.018	0.032	0.059	<0.001	0.031	0.0050	0.0021	0.011
Hi-Ti-2	0.078	1.46	0.022	0.110	0.059	<0.001	0.027	0.0046	0.0020	0.011
Lo-Ti-Lo-V	0.065	1.47	0.019	0.031	0.060	0.012	0.031	0.0046	0.0018	0.012
Hi-Ti-Lo-V	0.070	1.47	0.021	0.100	0.060	0.014	0.030	0.0041	0.002	0.012

Table B.2 – Laboratory Nb-Bearing Microalloyed Steels in wt pct

Material ID	C (Leco)	Mn	Si	Ti	Nb	V	Al	N (Leco)	S (Leco)	P
Lo-V	0.066	1.47	0.010	0.006	0.062	0.023	0.029	0.0053	0.0010	0.013
Hi-V	0.066	1.47	0.011	0.006	0.062	0.054	0.029	0.0049	0.0016	0.013
Lo-Nb	0.064	1.48	0.014	0.007	0.029	0.003	0.029	0.0051	0.0016	0.013
Hi-Nb	0.064	1.47	0.015	0.008	0.061	0.003	0.028	0.0045	0.0014	0.013
Lo-Ti	0.058	1.47	0.013	0.027	0.062	0.003	0.030	0.0058	0.0018	0.013
Hi-Ti	0.060	1.46	0.014	0.101	0.062	0.004	0.032	0.0050	0.0013	0.013
Lo-Ti-2	0.061	1.47	0.012	0.031	0.061	0.003	0.029	0.0055	0.0016	0.012
Hi-Ti-2	0.075	1.46	0.016	0.103	0.061	0.004	0.026	0.0051	0.0016	0.012
Lo-Ti-Lo-V	0.066	1.49	0.014	0.030	0.062	0.015	0.030	0.0051	0.0004	0.013
Hi-Ti-Lo-V	0.067	1.48	0.015	0.103	0.063	0.017	0.030	0.0052	0.0008	0.013

APPENDIX C: TEST SPECIMEN GEOMETRY

This appendix provides a schematic for the specimen geometries used for double-hit deformation testing. All test specimens were machined away from the edge of the plate, at least 25.4 mm (1.0 in) away from either side along the width and 5 mm (0.20 in) away from the top or bottom. Figure C.1 shows a schematic of the specimens used for double-hit deformation testing.

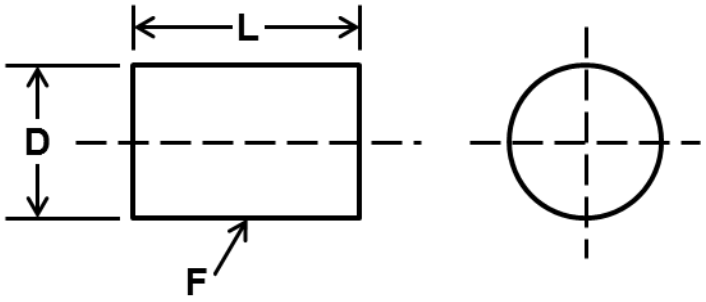

Dimensions	mm	in
D- Diameter	10.0 ± 0.025	0.394 ± 0.001
L- Length	15.0 ± 0.025	0.591 ± 0.001
F- Surface Finish (R_a)	0.4 µm	16 µin
Perpendicularity	±0.5°	±0.5°

Figure C.1 Schematic of hot compression specimen used in double-hit deformation testing for all ten alloys.

APPENDIX D: DOUBLE-HIT DEFORMATION TESTING DATA

This appendix provides more detail and insight into the results of the double-hit deformation tests. Specifically looking at the prior austenite grains (PAGs), Gleeble® 3500 program, and various quench media, heat treatments, and etchants used to reveal the PAGs.

D.1 Micrographs

The six main alloys were tested around the predicted T_{NR} and quenched to reveal the prior austenite grains. Figure D.1 through Figure D.6 show the PAGs for the Lo-V, Hi-V, Lo-Nb, Hi-Nb, Lo-Ti, and the Hi-Ti alloys, respectively just below, near, and just above the predicted T_{NR}.

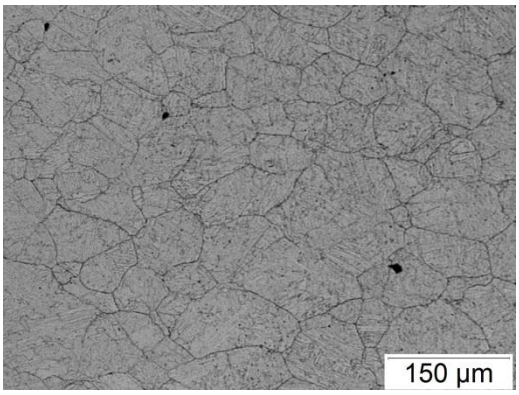

(a)

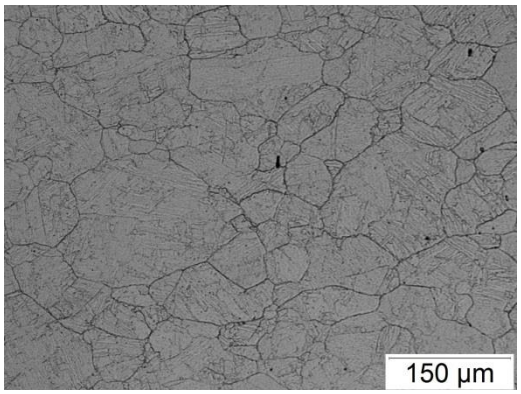

(b)

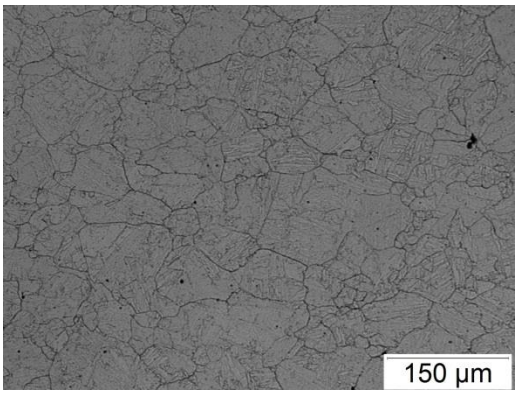

(c)

Figure D.1 Representative light micrographs showing the prior austenite grains (PAGs) of the deformed and quenched Lo-V (a) just below T_{NR} (b) near T_{NR} and (c) above T_{NR}. Each sample was etched with a modified Béchet–Beaujard reagent discussed in Section 3.7.2.

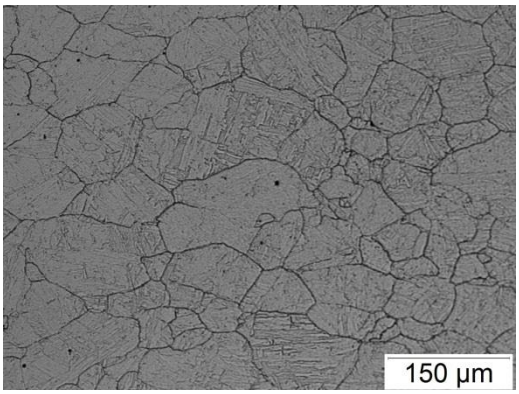

(a)

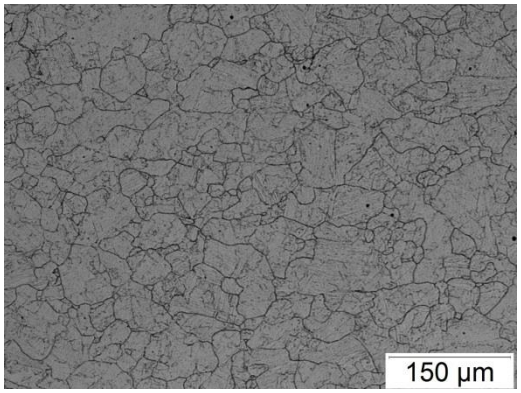

(b)

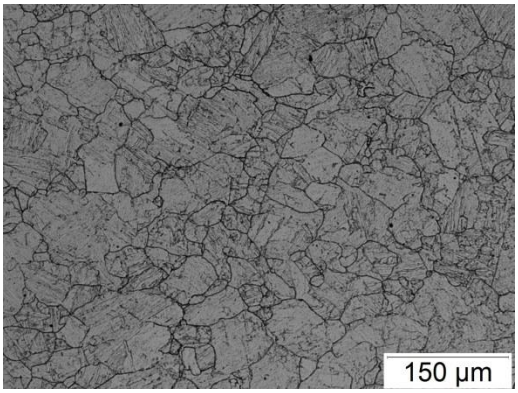

(c)

Figure D.2 Representative light micrographs showing the prior austenite grains (PAGs) of the deformed and quenched Hi-V (a) just below T_{NR} (b) near T_{NR} and (c) above T_{NR}. Each sample was etched with a modified Béchet–Beaujard reagent discussed in Section 3.7.2.

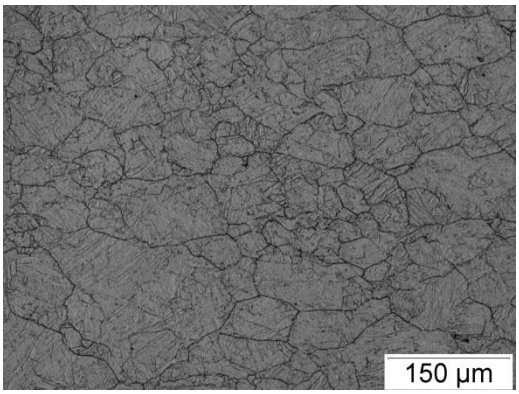

(a)

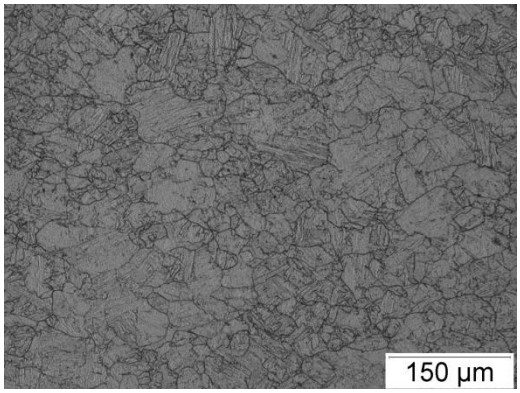

(b)

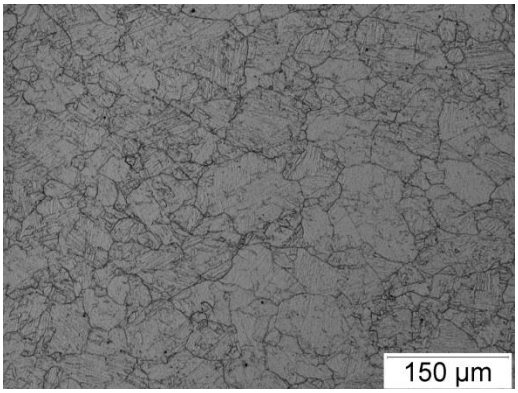

(c)

Figure D.3 Representative light micrographs showing the prior austenite grains (PAGs) of the deformed and quenched Lo-Nb (a) just below T_{NR} (b) near T_{NR} and (c) above T_{NR}. Each sample was etched with a modified Béchet–Beaujard reagent discussed in Section 3.7.2.

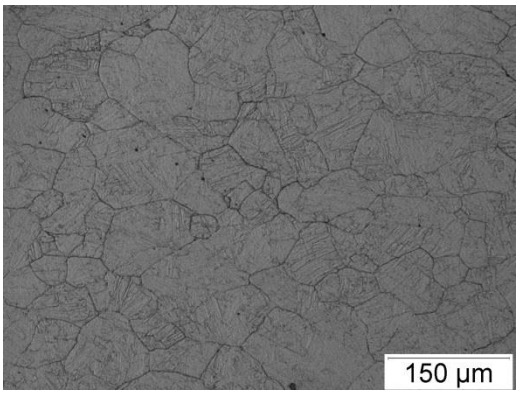

(a)

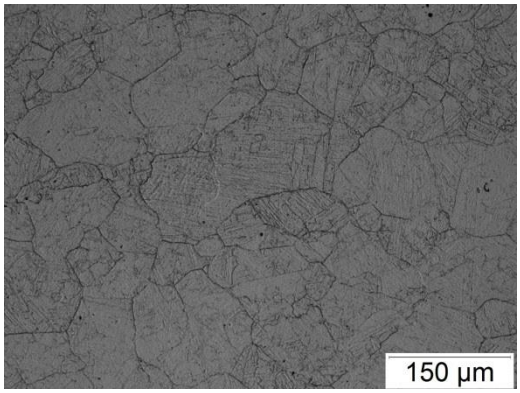

(b)

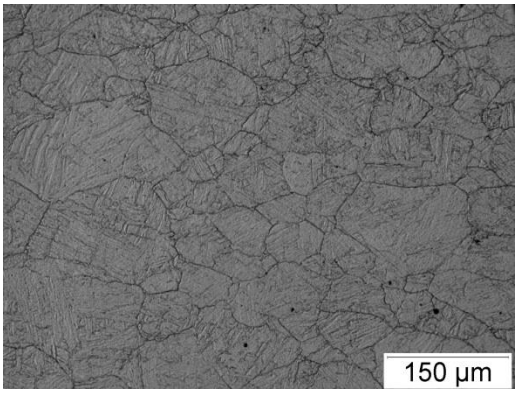

(c)

Figure D.4 Representative light micrographs showing the prior austenite grains (PAGs) of the deformed and quenched Hi-Nb (a) just below T_{NR} (b) near T_{NR} and (c) above T_{NR}. Each sample was etched with a modified Béchet–Beaujard reagent discussed in Section 3.7.2.

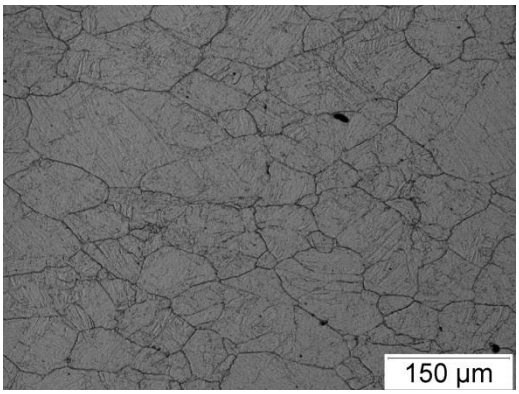

(a)

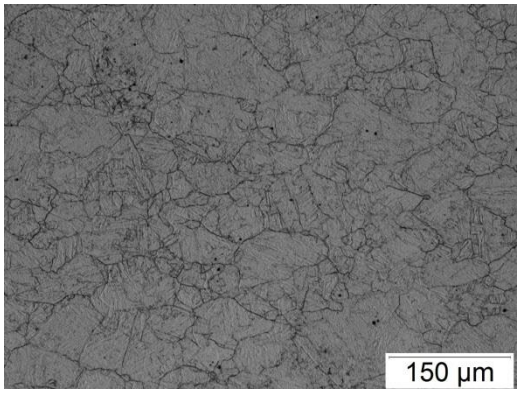

(b)

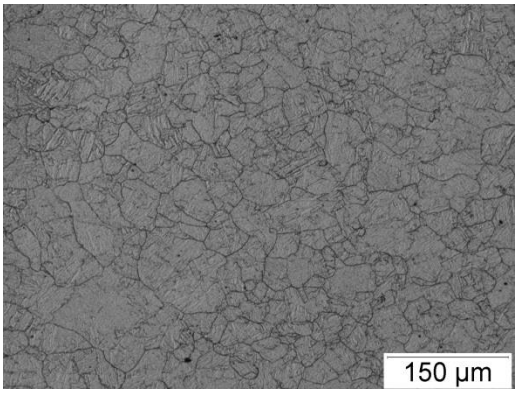

(c)

Figure D.5 Representative light micrographs showing the prior austenite grains (PAGs) of the deformed and quenched Lo-Ti (a) just below T_{NR} (b) near T_{NR} and (c) above T_{NR}. Each sample was etched with a modified Béchet–Beaujard reagent discussed in Section 3.7.2.

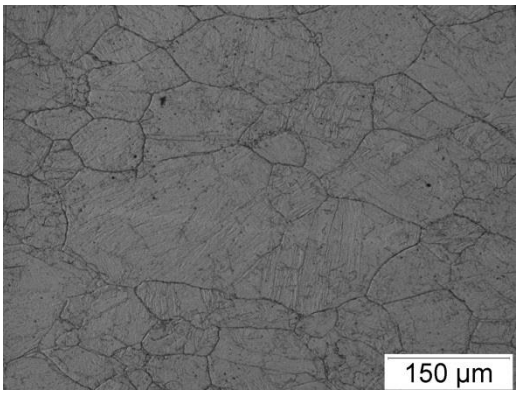

(a)

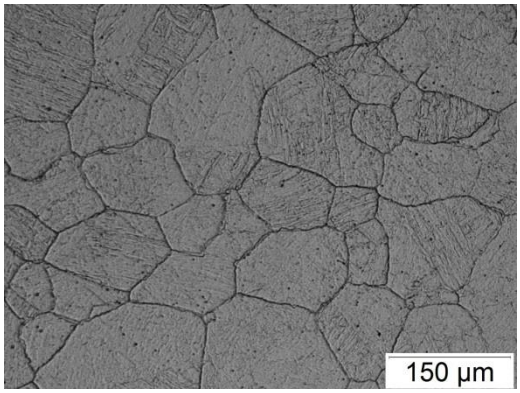

(b)

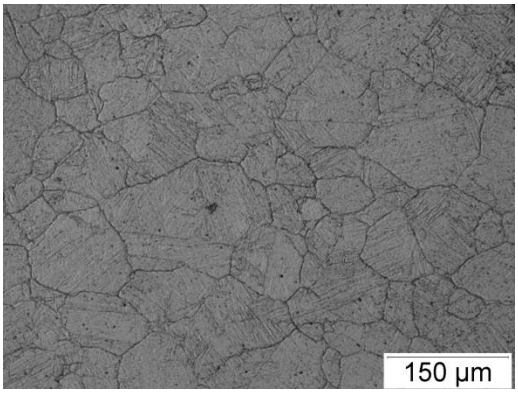

(c)

Figure D.6 Representative light micrographs showing the prior austenite grains (PAGs) of the deformed and quenched Hi-Ti (a) just below T_{NR} (b) near T_{NR} and (c) above T_{NR}. Each sample was etched with a modified Béchet–Beaujard reagent discussed in Section 3.7.2.

D.2 Prior Austenite Grain Etching

Many iterations of various quench media, etchants, and heat treatments were used to reveal austenite grains. Table D.1 shows the various techniques utilized and the results. Ultimately, the laboratory steel grades were found to be "too clean" and a He quench was not adequate to cool the center of the sample to fully martensitic. Water quenched was required. A 24 hour heat treatment at 500 °C (932 °F) and a modified Béchet–Beaujard reagent adequately revealed the PAGs for analysis.

Table D.1 – Tempering and Etching Procedure to Reveal Prior Austenite Grains

Quench Media	Condition	Etchant	Time	Back Polish (1µm diamond)	Notes
90 psi He	As Quenched	200 mL DI water 2.6 grams of Picric Acid 6 mL Teepol (3% of total solution) 2 mL HCl (1% of total solution) 60-70 °C	4-10 min	every 15-20 sec	martensite/bainite structure, no PAG
90 psi He	As Quenched	200 mL DI Water 2.6 g aq. Picric Acid 2 mL Teepol (1% of total solution) 2 mL HCl (1% total solution) 60-70 °C	4 min	every 15 sec	martensite/bainite structure, no PAG
90 psi He	As Quenched	200 mL DI Water 2.6 g aq. Picric Acid 2 mL Teepol (1% of total solution) 2 mL HCl (1% total solution) 60-70 °C	30 min	every 5 min	extreme pitting-possibly along PAG
90 psi He	Temper: 500 °C 3 hours (C. Nowill PhD)	200 mL DI Water 2.6 g aq. Picric Acid 2 mL Teepol (1% of total solution) 2 mL HCl (1% total solution) 60-70 °C	10 min	every 2 min	martensite/bainite structure, no PAG
90 psi He	Temper: 500 °C 24 hrs Barraclough	200 mL DI Water 2.6 g aq. Picric Acid 2 mL Teepol (1% of total solution) 2 mL HCl (1% total solution) 60-70 °C	10-45 min	every 5 min	PAG along sample edge, extreme pitting, back polish did very little
90 psi He	As Quenched	200 mL DI water 2.6 grams of Picric Acid 6 mL Teepol (3% of total solution) 2 mL HCl (1% of total solution) 60-70 °C	4-10 min	every 15-20 sec	martensite/bainite structure, no PAG
90 psi He	As Quenched	200 mL DI Water 2.6 g aq. Picric Acid 2 mL Teepol (1% of total solution) 2 mL HCl (1% total solution) 60-70 °C	4 min	every 15 sec	martensite/bainite structure, no PAG

Table D.2 Continued

Quench Media	Condition	Etchant	Time	Back Polish (1µm diamond)	Notes
90 psi He	As Quenched	200 mL DI Water 2.6 g aq. Picric Acid 2 mL Teepol (1% of total solution) 2 mL HCl (1% total solution) 60-70 °C	30 min	every 5 min	extreme pitting-possibly along PAG
90 psi He	Temper: 500 °C 3 hours (C. Nowill PhD)	200 mL DI Water 2.6 g aq. Picric Acid 2 mL Teepol (1% of total solution) 2 mL HCl (1% total solution) 60-70 °C	10 min	every 2 min	martensite/bainite structure, no PAG
90 psi He	Temper: 500 °C 24 hrs Barraclough	200 mL DI Water 2.6 g aq. Picric Acid 2 mL Teepol (1% of total solution) 2 mL HCl (1% total solution) 60-70 °C	10-45 min	every 5 min	PAG along sample edge, extreme pitting, back polish did very little

D.3 Double-Hit Deformation Program

Table D.3 shows a sample program used in the Gleeble® 3500 for double-hit deformation tests. To achieve true strain, multiple deformation steps were used to ensure a near-true strain simulation. The target strain rate was $5s^{-1}$, the actual strain rate was calculated to be $4.95 \pm 0.03s^{-1}$, which was considered on target.

Table D.3 – Double-Hit Deformation Program Used in the Gleeble® 3500

Action	Temp (°C)	Time	Force (lb)	Stroke (mm)	Diam	Notes
Force Control			125			
Heat to Soak	1250	02:05.0	125	-		10°C/sec
Hold at temp	1250	10:00.0	125	-		
Cool to T_{def}	*1200*	*00:40.0*	125	-		1.25°C/s- variable time to get to proper temp
Stroke Control	1200	00:00.001		15.00	10.00	
Def 1	1200	00:00.004		14.70	10.10	strain: 0.002
Def 2	1200	00:00.004		14.41	10.20	strain: 0.002
Def 3	1200	00:00.004		14.13	10.30	strain: 0.002
Def 4	1200	00:00.004		13.85	10.41	strain: 0.002
Def 5	1200	00:00.004		13.57	10.51	strain: 0.002
Def 6	1200	00:00.004		13.30	10.62	strain: 0.002
Def 7	1200	00:00.004		13.04	10.73	strain: 0.002
Def 8	1200	00:00.004		12.78	10.83	strain: 0.002
Def 9	1200	00:00.004		12.53	10.94	strain: 0.002
Def 10	1200	00:00.004		12.28	11.05	strain: 0.002
Force Control	1200	00:00.001	125	-		
Hold at temp	1200	00:04.998	125	-		Simulate Interpass time
Stroke Control	1200	00:00.001	-	12.28	11.05	
Def 1	1200	00:00.004		12.04	11.16	strain: 0.002
Def 2	1200	00:00.004		11.80	11.28	strain: 0.002
Def 3	1200	00:00.004		11.56	11.39	strain: 0.002
Def 4	1200	00:00.004		11.34	11.50	strain: 0.002
Def 5	1200	00:00.004		11.11	11.62	strain: 0.002
Def 6	1200	00:00.004		10.89	11.74	strain: 0.002
Def 7	1200	00:00.004		10.68	11.85	strain: 0.002
Def 8	1200	00:00.004		10.46	11.97	strain: 0.002
Def 9	1200	00:00.004		10.26	12.09	strain: 0.002
Def 10	1200	00:00.004		10.05	12.21	strain: 0.002
Cool	0	00:30.0		10.05	12.21	

D.4 Compression Test Evaluation

Table D.3 shows the range of values for the shape coefficients barreling, B, height, H, and ovality, O_v for all specimens. Table D.4-Table D.13 show the shape coefficients for each alloy divided by temperature. The ideal values for the coefficients are also listed. For the most part, the experimental

values fit within the limits of the barreling. All test showed higher than expected O_v, however the diameter measurements were not conducted per the standard. Instead, three locations along the height were measured at approximately 60° increments. This altered method is believed to cause the higher O_V values since some barreling occurred. All tests were within the H range of less than 0.04. The B was also on the higher side.

Table D.4 – Shape Coefficients to Validate Compression Tests

Value	B	H	O_V
Min	1.009	0.001	1.003
Max	1.123	0.032	1.095
Ideal	≤ 1.10	≤ 0.04	1.00

Table D.5 – Shape Coefficients to Validate Compression Tests for Lo-V Alloy

Temperature (°C)	B	StdDev of B	H	StdDev of H	Ov	StdDev of Ov
750	1.065	0.010	0.008	0.005	1.060	0.006
800	1.054	0.003	0.005	0.002	1.058	0.020
850	1.069	0.034	0.014	0.016	1.068	0.018
900	1.037	0.027	0.008	0.005	1.054	0.027
950	1.105	0.005	0.007	0.001	1.013	0.006
1000	1.096	0.004	0.004	0.001	1.019	0.005
1050	1.115	0.003	0.004	0.005	1.047	0.045
1100	1.100	0.011	0.005	0.002	1.012	0.002
1150	1.096	0.008	0.007	0.004	1.006	0.003
1200	1.110	0.012	0.003	0.002	1.014	0.010
Average	1.084	0.029	0.006	0.006	1.035	0.028

Table D.6 – Shape Coefficients to Validate Compression Tests for Hi-V Alloy

Temperature (°C)	B	StdDev of B	H	StdDev of H	Ov	StdDev of Ov
750	1.076	0.005	0.005	0.002	1.069	0.018
800	1.068	0.001	0.004	0.004	1.059	0.016
850	1.066	0.018	0.006	0.005	1.068	0.005
900	1.071	0.013	0.008	0.000	1.093	0.004
950	1.115	0.082	0.014	0.008	1.068	0.011
1000	1.056	0.052	0.014	0.004	1.051	0.031
1050	1.092	0.025	0.011	0.008	1.036	0.023
1100	1.115	0.012	0.021	0.013	1.077	0.032
1150	1.059	0.032	0.005	0.003	1.070	0.034
1200	1.112	0.009	0.039	0.028	1.075	0.042
Average	1.083	0.037	0.013	0.014	1.067	0.025

Table D.7 – Shape Coefficients to Validate Compression Tests for Lo-Nb Alloy

Temperature (°C)	B	StdDev of B	H	StdDev of H	Ov	StdDev of Ov
750	1.046	0.061	0.005	0.003	1.065	0.018
800	1.066	0.020	0.007	0.004	1.051	0.006
850	1.055	0.021	0.006	0.006	1.057	0.007
900	1.077	0.009	0.004	0.002	1.077	0.003
950	1.770	0.624	0.002	0.003	1.066	0.019
1000	1.094	0.008	0.007	0.005	1.083	0.016
1050	1.084	0.028	0.005	0.002	1.080	0.033
1100	1.098	0.007	0.008	0.007	1.092	0.014
1150	1.087	0.009	0.002	0.001	1.099	0.013
1200	1.088	0.007	0.009	0.001	1.106	0.014
Average	1.145	0.264	0.006	0.004	1.078	0.022

Table D.8 – Shape Coefficients to Validate Compression Tests for Hi-Nb Alloy

Temperature (°C)	B	StdDev of B	H	StdDev of H	Ov	StdDev of Ov
750	1.071	0.007	0.003	0.002	1.073	0.004
800	1.040	0.055	0.005	0.005	1.056	0.016
850	1.046	0.017	0.005	0.003	1.063	0.012
900	1.068	0.005	0.006	0.001	1.070	0.017
950	1.084	0.015	0.005	0.003	1.093	0.040
1000	1.082	0.019	0.005	0.002	1.078	0.007
1050	1.095	0.016	0.009	0.005	1.098	0.021
1100	1.087	0.012	0.012	0.004	1.088	0.021
1150	1.088	0.012	0.009	0.005	1.081	0.003
1200	1.087	0.014	0.006	0.007	1.094	0.036
Average	1.074	0.026	0.006	0.004	1.079	0.021

Table D.9 – Shape Coefficients to Validate Compression Tests for Lo-Ti Alloy

Temperature (°C)	B	StdDev of B	H	StdDev of H	Ov	StdDev of Ov
750	1.091	0.003	0.007	0.003	1.074	0.007
800	1.081	0.015	0.004	0.001	1.073	0.021
850	1.071	0.004	0.007	0.006	1.075	0.007
900	1.035	0.051	0.014	0.004	1.046	0.029
950	1.074	0.013	0.010	0.004	1.067	0.012
1000	1.274	0.319	0.006	0.002	1.074	0.004
1050	1.097	0.008	0.003	0.003	1.097	0.006
1100	1.093	0.010	0.007	0.001	1.091	0.013
1150	1.088	0.013	0.012	0.002	1.095	0.023
1200	1.080	0.020	0.007	0.004	1.110	0.033
Average	1.098	0.105	0.008	0.004	1.080	0.023

Table D.10 – Shape Coefficients to Validate Compression Tests for Hi-Ti Alloy

Temperature (°C)	B	StdDev of B	H	StdDev of H	Ov	StdDev of Ov
750	1.096	0.026	0.005	0.004	1.068	0.023
800	1.044	0.011	0.013	0.010	1.060	0.012
900	1.084	0.007	0.004	0.004	1.085	0.014
950	1.071	0.026	0.003	0.001	1.083	0.053
1000	1.089	0.104	0.013	0.003	1.103	0.075
1050	1.099	0.016	0.006	0.005	1.158	0.124
1100	1.438	0.386	0.005	0.002	1.092	0.059
1150	1.053	0.043	0.006	0.005	1.063	0.026
1200	1.094	0.013	0.005	0.001	1.094	0.004
Average	1.123	0.167	0.006	0.005	1.091	0.057

Table D.11 – Shape Coefficients to Validate Compression Tests for Lo-Ti-2 Alloy

Temperature (°C)	B	StdDev of B	H	StdDev of H	Ov	StdDev of Ov
750	1.075	0.022	0.006	0.001	1.066	0.016
800	1.073	0.011	0.006	0.002	1.060	0.017
850	1.066	0.013	0.011	0.004	1.070	0.006
900	1.067	0.006	0.005	0.003	1.054	0.023
950	1.075	0.009	0.006	0.002	1.078	0.007
1000	1.080	0.010	0.006	0.004	1.081	0.014
1050	1.079	0.027	0.008	0.005	1.085	0.022
1100	1.120	0.018	0.008	0.002	1.105	0.006
1150	1.134	0.022	0.010	0.001	1.088	0.025
1200	1.133	0.013	0.021	0.020	1.104	0.022
Average	1.090	0.030	0.009	0.007	1.079	0.022

Table D.12 – Shape Coefficients to Validate Compression Tests for Hi-Ti-2 Alloy

Temperature (°C)	B	StdDev of B	H	StdDev of H	Ov	StdDev of Ov
750	1.065	0.020	0.005	0.005	1.082	0.025
800	1.093	0.034	0.014	0.005	1.074	0.012
850	1.119	0.006	0.003	0.002	1.192	0.175
900	1.101	0.019	0.007	0.005	1.108	0.014
950	1.079	0.008	0.004	0.002	1.083	0.005
1000	1.096	0.024	0.007	0.002	1.074	0.023
1050	1.092	0.042	0.009	0.005	1.119	0.022
1100	1.104	0.022	0.005	0.005	1.108	0.035
1150	1.117	0.034	0.014	0.001	1.091	0.011
1200	1.138	0.015	0.008	0.002	1.090	0.020
Average	1.100	0.029	0.008	0.005	1.102	0.059

Table D.13 – Shape Coefficients to Validate Compression Tests for LoTi-LoV Alloy

Temperature (°C)	B	StdDev of B	H	StdDev of H	Ov	StdDev of Ov
750	1.084	0.005	0.005	0.001	1.071	0.011
800	1.042	0.028	0.003	0.001	1.055	0.027
850	1.063	0.029	0.009	0.007	1.091	0.008
900	1.057	0.012	0.002	0.001	1.065	0.011
950	1.081	0.008	0.003	0.003	1.098	0.023
1000	1.075	0.019	0.003	0.001	1.093	0.004
1050	1.112	0.008	0.003	0.000	1.109	0.023
1100	1.095	0.020	0.007	0.002	1.114	0.006
1150	1.100	0.020	0.004	0.000	1.120	0.023
1200	1.104	0.002	0.005	0.002	1.145	0.017
Average	1.082	0.026	0.004	0.003	1.096	0.031

Table D.14 – Shape Coefficients to Validate Compression Tests for HiTi-LoV Alloy

Temperature (°C)	B	StdDev of B	H	StdDev of H	Ov	StdDev of Ov
750	1.071	0.019	0.003	0.002	1.079	0.003
800	1.092	0.015	0.003	0.001	1.073	0.015
850	1.075	0.037	0.007	0.004	1.074	0.009
900	1.081	0.024	0.007	0.004	1.082	0.027
950	1.095	0.018	0.007	0.002	1.076	0.004
1000	1.082	0.025	0.004	0.002	1.082	0.010
1050	1.097	0.007	0.007	0.005	1.100	0.005
1100	1.110	0.008	0.004	0.003	1.119	0.006
1150	1.099	0.009	0.004	0.003	1.108	0.014
1200	1.104	0.010	0.004	0.003	1.118	0.017
Average	1.091	0.020	0.005	0.003	1.091	0.021